



UNIVERSIDAD NACIONAL AUTÓNOMA DE MÉXICO

PROGRAMA DE POSGRADO EN ASTROFÍSICA
Instituto de Astronomía

Observaciones de He II estelar en NGC 346 y NGC 3125-A1

TESIS
QUE PARA OPTAR POR EL GRADO DE:
DOCTOR EN CIENCIAS (ASTROFÍSICA)

PRESENTA:

José Andrés Sixtos González

ASESORA:

Aida Hortensia Nava Bencheikh, Instituto de Astronomía - UNAM

Ensenada, Baja California - 4 de octubre de 2023



UNAM – Dirección General de Bibliotecas

Tesis Digitales
Restricciones de uso

DERECHOS RESERVADOS ©
PROHIBIDA SU REPRODUCCIÓN TOTAL O PARCIAL

Todo el material contenido en esta tesis está protegido por la Ley Federal del Derecho de Autor (LFDA) de los Estados Unidos Mexicanos (Méjico).

El uso de imágenes, fragmentos de videos, y demás material que sea objeto de protección de los derechos de autor, será exclusivamente para fines educativos e informativos y deberá citar la fuente donde la obtuvo mencionando el autor o autores. Cualquier uso distinto como el lucro, reproducción, edición o modificación, será perseguido y sancionado por el respectivo titular de los Derechos de Autor.

Agradecimientos

Agradezco al Consejo Nacional de Humanidades, Ciencia y Tecnología por la beca otorgada durante los cuatro años de mi doctorado. Asimismo, agradezco al Instituto de Astronomía de la Universidad Nacional Autónoma de México, y a la misma Universidad, por brindarme todos los recursos necesarios para mi estadía en esta institución.

Agradezco a los miembros del comité evaluador de este trabajo, la Dra. Gloria Koenigsberger, Dra. Miriam García, Dr. Gustavo Bruzual, Dr. Divakara Mayya y Dr. Christophe Morisset. Las recomendaciones a la ciencia y escritura de este trabajo, enriquecieron sustancialmente la investigación y presentación de la misma. Agradezco también al Dr. Sebastián Sánchez, por la guía a lo largo de estos 6 años de posgrado formando parte de mi comité tutor.

A la Dra. Gloria Koenigsberger, por recibirme en los primeros pasos de mi camino en astrofísica. Sus recomendaciones, trato y apoyo de inicio a fin fueron importantes en mi desarrollo académico.

Al Dr. Christophe Morisset, que ha sido un pilar importante en mi desarrollo académico. Su guía y recomendaciones han sido fundamentales en mis seis años de posgrado. Su apoyo al llegar a una nueva tierra jugó un papel importante para el inicio de mi doctorado. Los vinos, quesos, postres y pláticas compartidas con él y Marie, hicieron ameno mi paso por el doctorado.

Agradezco a la Dra. Aida Nava, porque sin su guía, su paciencia, su trato, su manera impresionante de ver la ciencia y a las personas que la forjan, mi investigación doctoral no habría sido posible. Es, sin lugar a duda, una de las personas más impresionantes que he conocido, y una de las científicas más grandes que jamás conoceré.

Agradezco a todos los compañeros del posgrado que amenizaron mi paso por el doctorado. A Rogelio, por las pláticas científicas en la oficina que aportaron mucho a mi entendimiento del tema, pero sobre todo, por la amistad reflejada en decenas de tazas de café, platos de birria, reuniones para juegos y charlas, consejos y risas para seguir adelante. A Sergio, por ser mi dosis de cultura internacional, por las pláticas en la terraza y por la compañía en las desoladas tardes de oficina. A David, por las pláticas con café y comida que se transformaron en las reuniones oficiales de doctorado.

Te agradezco Morgan, has sido un sostén en mi paso por el doctorado y en la vida. Sin tu compañía habría sido complicado sobrellevar los años de pandemia. Agradezco absolutamente todo lo que has compartido conmigo, tu tiempo, tus partidas de Apex, tu comida, tus problemas, tu cariño, tus risas, tus locuras, tus ideas, pero sobre todo, tu amistad.

Te agradezco, Valeria, de ti he recibido un apoyo fundamental para mi desarrollo académico y personal. Has sido un ancla en este yermo puerto. Los desayunos, cigarros, pláticas, cafés, peleas, risas, confidencias, vinos, han sido el origen de una de las amistades más importantes de mi vida.

Te agradezco madre, padre, hermana, que a la lejanía jamás me han dejado sentir solo. Han sido un apoyo incondicional y una de mis razones de vida.

Te agradezco a ti, Elizabeth, la persona más importante para mí durante estos años en tierras extrañas. Has sido la razón principal de mi crecimiento estos últimos cuatro años. Agradezco tu tiempo, paciencia, consejo, compañía y amor. Admiro tu inalcanzable estado sublime al existir. No hay nadie más grande que tú. Te amo.

Contenido

Introducción General	5
1.1 Objetivos	5
1.2 Importancia de las estrellas masivas	5
1.3 Evolución de las estrellas masivas	6
1.4 Estrellas Wolf-Rayet	7
1.5 Very Massive Stars	8
1.6 Mecanismos de formación y fuentes de las líneas de He II.	8
1.7 Modelos de síntesis de población estelar	10
Looking for nebular He II emission south of the multiple-massive star system, HD 5980	13
1.1 Resumen	13
1.2 Contribución	14
Extreme broad He II emission at high and low redshifts: the dominant role of VMS in NGC 3125-A1 and CDF-S131717.	33
2.1 Resumen	33
2.2 Contribución	33
Conclusiones generales	53

Resumen General

En algunas galaxias, cuya emisión está dominada por la formación estelar, se puede observar emisión de He II ancha, para la cual comúnmente se dice que se forma en el viento de estrellas masivas (principalmente a metalicidad solar o similar a la de las Nubes de Magallanes). Adicionalmente, se puede observar emisión angosta nebulosa de He II, que domina conforme disminuye la metalicidad. En esta tesis, se estudió la emisión de He II al sur de HD 5980, un sistema múltiple formado por dos estrellas WR (WN6h + WN6-7) y una estrella tipo O. Dicho sistema se encuentra en la Nube Menor de Magallanes (SMC, por sus siglas en inglés). Asimismo, se estudió la emisión de He II del supercúmulo de estrellas, A1, en la galaxia tipo starburst, NGC 3125. Como objetivo principal, el primer estudio buscó verificar si la presencia de estrellas tipo WN genera He II nebuloso en el objeto estudiado, debido a que en la literatura se suele presentar a estas estrellas como principales fuentes de fotones ionizantes de He II necesarios para formar líneas nebulosas de He II angostas. Para ello, se empleó tanto espectroscopía óptica que cubre la emisión de He II 4686Å al sur de HD 5980, así como modelos de atmósferas para WNs que predicen la tasa de fotones ionizantes de He II que escapan del viento de estas estrellas. Como conclusión principal se sugiere que *las estrellas WN no son fuentes claras de fotones ionizantes de HeII a la metalicidad de la SMC, con lo que se recomienda actualizar algunos de los modelos de síntesis de poblaciones estelares más usados que asumen lo contrario.* El segundo estudio tuvo como principal enfoque demostrar la importancia de las estrellas muy masivas (Very Massive Stars - VMS - en inglés) para poder reproducir algunas líneas de He II estelar anchas extremadamente fuertes que se han observado en algunas galaxias con brotes estelares, tanto a bajo como a alto ($z=2-3$) corrimiento al rojo. Como resultado, se encontró que *las VMS sí son necesarias para explicar la línea de HeII 1640Å ancha del supercúmulo NGC 3125-A1. Adicionalmente, se encontró que la línea de absorción de Ov 1371Å ancha producida íntegramente en el viento de las estrellas, es un buen marcador de la extrema juventud de las poblaciones de estrellas masivas no resueltas.* Ambos estudios se presentan en esta tesis como artículos publicados.

1. Introducción General

1.1. Objetivos

Observaciones espacialmente no resueltas de galaxias con formación estelar pueden presentar emisiones angostas y/o anchas de líneas de alta ionización de He II λ 4686 (óptico) o su equivalente en el ultravioleta (He II λ 1640). Esto es cierto para galaxias cercanas (Mingozzi et al., 2022) y hasta la era de mayor formación estelar del Universo (Shapley et al., 2003; Saxena et al., 2020), conocida como el medio día cósmico (cosmic noon, en inglés), a corrimientos al rojo entre 2 y 3 (Madau & Dickinson, 2014). Por otro lado, el proyecto JWST Jades detectó una línea de He II λ 1640 en la galaxia GN-z11, localizada a $z=10.6$, la cual ha sido interpretada como evidencia de la presencia de estrellas libres de metales de Población III (Maiolino et al., 2023).

En términos generales, esta tesis explora el papel que juegan algunas estrellas masivas en la generación de líneas anchas (estelares) y angostas (nebulares) de He II. Si se puede establecer este rol de manera clara, entonces se puede invertir el problema y aprender sobre las poblaciones de estrellas masivas utilizando observaciones integradas. La tesis contiene dos artículos publicados. El objetivo del primer artículo es establecer si estrellas masivas evolucionadas conocidas como WNs son buenas fuentes de fotones ionizantes que puedan generar He II nebuloso. Para esto se estudió un región cercana al sistema múltiple de estrellas HD 5980 en la Nube Menor de Magallanes (SMC). Por otro lado, el objetivo del segundo artículo es establecer qué tipo de estrellas masivas se requieren para reproducir la emisión ancha y extrema de He II estelar que se observa en algunas poblaciones estelares. Para esto se estudiaron dos objetos, el supercúmulo de estrellas masivas A1 de la galaxia cercana NGC 3125, y una galaxia del cosmic noon.

En esta introducción, antes de abordar los temas de los artículos describimos la importancia de las estrellas masivas de manera general, resumimos lo que se conoce sobre su evolución, introducimos lo que son las estrellas Wolf-Rayet clásicas y las estrellas muy masivas (Very Massive Stars, VMS, por sus siglas en inglés), explicamos cuáles son los mecanismos de formación y fuentes de las líneas de He II en el Universo, y resumimos lo que son los modelos de síntesis de poblaciones estelares.

1.2. Importancia de las estrellas masivas

Las estrellas masivas son aquellas con masas por encima del límite para la formación de un núcleo degenerado de C-O, lo que significa que pueden quemar carbono en su núcleo de forma no degenerada. Se definen con un límite inferior de masa de aproximadamente $8 M_{\odot}$, siendo estrellas tipo espectral O y B por ser muy calientes y luminosas.

Las estrellas masivas representan un tema de estudio central en la astrofísica, ya que impulsan la evolución química de las galaxias, inyectan energía y momento a través de los vientos estelares y las explosiones de supernovas, modifican de este modo el estado físico del gas interestelar y repercuten en la formación estelar (Meynet et al., 2009) y son responsables de la mayor producción de los elementos alfa (Woosley & Weaver, 1995).

A bajas metalicidades, estas estrellas aportan importantes cantidades de carbono y nitrógeno al medio interestelar (Pettini et al., 2008; Chiappini et al., 2006). A lo largo de su evolución,

enriquecen el entorno circundante y generan vientos supersónicos debido a la intensa radiación ultravioleta emitida por sus altas temperaturas efectivas, que oscilan entre 20,000 K y 200,000 K (Wofford et al., 2012). Como resultado de estas características, las estrellas masivas contribuyen a la formación de estructuras complejas como burbujas ionizadas o regiones H II, y su muerte da lugar a eventos astronómicos significativos, como supernovas de tipo Ib, Ic, II o estallidos de rayos gamma largos (Dessart et al., 2012). Adicionalmente, el destino de aquellas con masas por encima de las $100 M_{\odot}$ terminarán su vida como supernovas de creación de pares o agujeros negros. También se consideran cruciales en el contexto de la reionización en el Universo temprano (Robertson et al., 2010) y el alto de la formación estelar en galaxias de muy baja masa del Universo temprano (Brown et al., 2014). En tiempos más recientes, el estudio de la evolución de las estrellas masivas que tienen como destino un objeto compacto, tales como agujeros negros o estrellas de neutrones, representa un indicio de la formación de ondas gravitacionales. El número de eventos de ondas gravitacionales detectados cuyo origen esta impulsado por agujeros negros binarios, sistemas de agujero negro y estrella de neutrones o estrellas de neutrones binarias, ha aumentado (Abbott et al., 2019, 2020, 2021; The LIGO Scientific Collaboration et al., 2021). Estas detecciones proveen de información importante sobre las propiedades, como masa y rotación, de estos objetos compactos y a su vez, de la formación, vida y muerte de estrellas masivas a través de la historia cósmica (Broekgaarden et al., 2022).

1.3. Evolución de las estrellas masivas

Las estrellas masivas se forman típicamente en nubes moleculares con masas cercanas a $10^5 M_{\odot}$ (Völschow et al., 2017). Su evolución y pérdida de masa depende de las propiedades iniciales de la estrella, como la masa y la composición química. Como se comentó en la sección anterior, además de no desarrollar un núcleo degenerado de C-O y quemar carbono de forma no degenerada, una estrella se considera masiva cuando atraviesa por todas las fases de combustión hasta el silicio incluido y terminando su vida con una explosión de supernova o colapsar directamente a un agujero negro (Hirschi et al., 2010).

Después de dejar la secuencia principal, las estrellas que se encuentran en el rango de 8 a $13 M_{\odot}$, se convertirán en supergigantes rojas (RSG, por sus siglas en inglés), por otra parte las estrellas con masas entre 13 y $25 M_{\odot}$ permanecerán como RSG después de salir de la secuencia principal, hasta que finalmente mueran como supernovas tipo II. En estrellas RSG, aunque las temperaturas de la superficie se están enfriando, en el núcleo las temperaturas y densidades centrales aumentan inexorablemente. En un momento dado, una zona de material que rodea el núcleo, se calienta lo suficiente como para comenzar la fusión de hidrógeno, comenzando así la combustión de hidrógeno en la envolvente. Finalmente, la temperatura y la densidad del núcleo son lo suficientemente altas como para que el helio pueda empezar a fusionarse en carbono.

Si la masa de la estrella se encuentra en el rango de 25 - $40 M_{\odot}$, esta se convertirá en supergigante roja y debido a la pérdida de masa perderá su envolvente de hidrógeno, convirtiéndose en estrella Wolf-Rayet. La mayoría de las estrellas en este rango de masas terminarán sus vidas como supernovas tipo Ib. Para masas por encima de $40 M_{\odot}$, las estrellas pierden su envolvente de hidrógeno antes de llegar a la fase de supergigante roja debido a las grandes tasas de pérdida de masa. Aquellas que cuentan con masas entre 40 - $90 M_{\odot}$, pasan por una fase de variable azul luminosa (LBV, por sus siglas en inglés), las cuales sufren pérdidas de masa episódicas y representan una fase de transición entre las estrellas O y las estrellas Wolf-Rayet (Hirschi et al., 2010). Algunas observaciones han mostrado que las estrellas masivas podrían morir en la etapa LBV (Kotak & Vink, 2006), y que son las progenitoras para algunas supernovas tipo IIn (Trundle et al., 2008; Gal-Yam & Leonard, 2009).

Una vez que el núcleo de la estrella masiva está dominado por los elementos del pico de hierro, la contracción del núcleo y su aumento de temperatura ya no libera energía de las reacciones nucleares que dejan de ser exotérmicas, por lo que no es posible mantener la presión

interna que contrareste la gravedad. Si la masa del núcleo esta por debajo de $\sim 2.5 M_{\odot}$ (masa de Oppenheimer-Volkoff) el destino final de la estrella masiva es una estrella de neutrones. De otra forma el colapso continuará, pues la presión ejercida por los neutrones degenerados no será suficiente, y un agujero negro será formado.

La evolución de estrellas con masas superiores a $40 M_{\odot}$ presenta complicaciones particulares. Estas estrellas exhiben luminosidades cercanas a la luminosidad crítica de Eddington, que establece el límite para mantener el equilibrio entre la presión debida a la fuerza gravitacional y la presión de radiación. La ineficiencia de la convección debajo de la superficie provoca protuberancias en su opacidad, lo que resulta en un aumento en la luminosidad radiativa, superando el límite de Eddington. Para mantener el equilibrio hidrostático, la densidad y presión del gas, que normalmente disminuyen con el radio, experimentan aumentos locales en las capas por debajo de la superficie, dando lugar a inversiones de densidad y presión del gas. Estas inversiones de densidad plantean desafíos al modelizar la evolución de estrellas masivas, ya que los pasos temporales de la simulación se vuelven excesivamente pequeños y la modelización posterior de la estrella se convierte en un reto computacional (Paxton et al., 2013). Por tanto, se requiere emplear ciertas técnicas, como aumentar las tasas de pérdida de masa para eliminar las capas exteriores problemáticas o incrementar la eficiencia convectiva mediante la aplicación de una mezcla del material proporcional a la altura de la escala de densidad, con el fin de avanzar en la evolución de las estrellas masivas más allá de estas inestabilidades numéricas. Estas estrategias permiten superar los desafíos asociados con la simulación de estrellas masivas y facilitan un estudio más preciso y confiable de su evolución astrofísica (Agrawal, 2021).

Otro factor importante que considerar en la evolución de las estrellas masivas, es la binariedad. Se piensa que el porcentaje de estrellas masivas OB de secuencia principal en sistemas binarios puede ser del 70% o mayor. Sin embargo las observaciones no han sido concluyentes. Estudios han encontrado que estrellas súpergigantes rojas, descendientes directas de estrellas evolucionadas OB, se encuentren en sistemas binarios acompañadas de estrellas de tipo B no evolucionadas en una fracción del 15-30% (Neugent et al., 2021). Algunos de las implicaciones de la binariedad esta sobre el proceso de vientos. Una estrella individual puede perder masa vía vientos estelares. En un sistema binario, una de las compañeras puede acretar este viento expulsado, transportando así momento angular. La evolución de un sistema binario depende de muchas variables, tales como el periodo binario inicial, la excentricidad y el cociente de las masas. Para periodos orbitales suficientemente grandes, las componentes del sistema pueden evolucionar independientemente, como si fueran estrellas individuales.

Aunque se ha avanzado en el conocimiento de la formación y evolución de las estrellas masivas tanto individualmente como en relación con la función inicial de masa, aún existe la necesidad de mejorar nuestra comprensión al respecto (Garcia et al., 2019).

1.4. Estrellas Wolf-Rayet

En el primer artículo nos enfocamos en las estrellas masivas que pasan por la fase de Wolf-Rayet, descrita en esta sección.

Las estrellas WR clásicas son las descendientes de las estrellas tipo O que han perdido sus capas externas, debido a vientos intensos y procesos eruptivos durante la etapa LBV o a transferencia de masa en sistemas binarios. Tienen masas de más de $20 M_{\odot}$ (dependiendo de la metalicidad de la progenitora, (Massey, 2003)). Tienen tasas de pérdida de masa de hasta $\sim 10^{-4} M_{\odot} \text{ yr}^{-1}$ y se caracterizan por tener vientos densos y veloces donde se producen líneas de emisión de He II anchas, es decir, con anchuras a media altura (FWHM, por sus siglas en inglés) $\geq 1000 \text{ km s}^{-1}$ (Crowther, 2007). Se encuentran quemando helio en su núcleo y sus espectros son deficientes en líneas de hidrógeno debido a que lo han perdido en su atmósfera vía erupciones y vientos en etapas evolutivas anteriores.

Se clasifican según los perfiles presentes en sus espectros, aquellas con fuertes líneas de He y N

son denominadas WN, mientras que aquellas que presentan, además de líneas de helio, emisiones fuertes de carbono y oxígeno, se clasifican como WC y WO. Aunque los modelos de evolución de estrellas masivas aisladas con muy baja metalicidad, es decir, con $O/H < (O/H)_{\odot}/20$, no evolucionan hasta la fase de WC por sí solas, es posible formar estrellas WC por el canal binario, por el que una de las estrellas masivas transfiere su atmósfera de hidrógeno a su compañera. (e.g., (Götberg et al., 2017); (Stanway et al., 2020)). Esto podría explicar porqué se han reportado detecciones de estrellas WR en I Zw 18 ((Legrand et al., 1997); (Brown et al., 2002)) y SBS 0335-052E ((Papaderos et al., 2006); (Izotov et al., 2006)). De hecho, las estrellas WR a menudo se encuentran en sistemas binarios que intercambian masa (por ejemplo, (Hainich et al., 2015)). En binarias, las WR pueden ser progenitores de agujeros negros binarios que al fundirse generan ondas gravitacionales. Por otro lado, las estrellas WN son divididas según el cociente del flujo de sus líneas de He y N. Usando las relaciones de N IV-V se clasifican las WN2-5 (o WNE, siendo la E por *early*), mientras que observando los cocientes de N III-V se catalogan las WN7-9 (o WNL, siendo la L por *late*), pudiendo las WN6 formar parte de las WNE o WNL, ambas clasificaciones usan adicionalmente los cocientes de He I-II (Smith et al., 1996).

1.5. Very Massive Stars

Recientemente, se han descubierto estrellas con masas de más de $150 M_{\odot}$ (Crowther et al., 2010), conocidas como Very Massive Stars (VMS, por sus siglas en inglés) que son relevantes en el segundo artículo de esta tesis. Las VMS fueron descubiertas en el cúmulo estelar R136, el cual se encuentra en el centro de la región H II NGC 2070 en la Nube Mayor de Magallanes (LMC, por sus siglas en inglés). El espectro integrado de todo el cúmulo R136 muestra emisión He II, y dicha emisión está dominada por siete estrellas tipo VMS (Crowther et al., 2016). Aunque las altas pérdidas de masa generan líneas anchas de He II en VMS, se ha encontrado que la proximidad de su luminosidad al límite de Eddington contribuye también a este efecto (Vink et al., 2011).

Varias de las VMS encontradas en R136 están clasificadas como WNH (que son estrellas WR no clásicas) o estrellas en transición Of/WN (Crowther et al., 2016). La clasificación, WNH, fue propuesta en (Smith & Conti, 2008) para estrellas que además de los perfiles característicos de nitrógeno, cuentan con líneas de hidrógeno en su espectro. Se encuentran quemando hidrógeno en su núcleo y tienen tasas de pérdida de masa altas. Algunos autores (Schaller et al., 1992; Meynet et al., 1994; Maeder & Meynet, 1994) proponen que dichas estrellas se encuentran después o en lugar de la fase variable azul luminosa (LBV, por sus siglas en inglés), marcando el inicio de la quema de helio en el núcleo, sin embargo (Smith & Conti, 2008) concluye que la estrellas WNH se presentan como un estado que precede a las fase LBV, a partir de la alta luminosidad que presentan algunas de estas estrellas (con luminosidades por encima de $\log(L/L_{\odot}) = 5.8-6.0$), así como su pertenencia a cúmulos estelares masivos muy jóvenes, tales como R136 en 30 doradus y NGC 3603 (Drisken et al., 1995; Crowther et al., 2016). Otras galaxias que podrían albergar VMS son NGC 3125 (Wofford et al., 2014), NGC 5253 (Smith et al., 2016), II Zw 40 (Leitherer et al., 2018) y algunas regiones locales de formación estelar, tales como: Tol89-A, seis regiones H II en M101, NGC 4214, NGC 4670 y Mrk 33 (Martins et al., 2023).

1.6. Mecanismos de formación y fuentes de las líneas de He II.

Las principales observables de esta tesis son las líneas de He II en 4686 y 1640 Å, las cuales son las más luminosas de He II en el óptico y ultravioleta (UV) respectivamente. Para ionizar

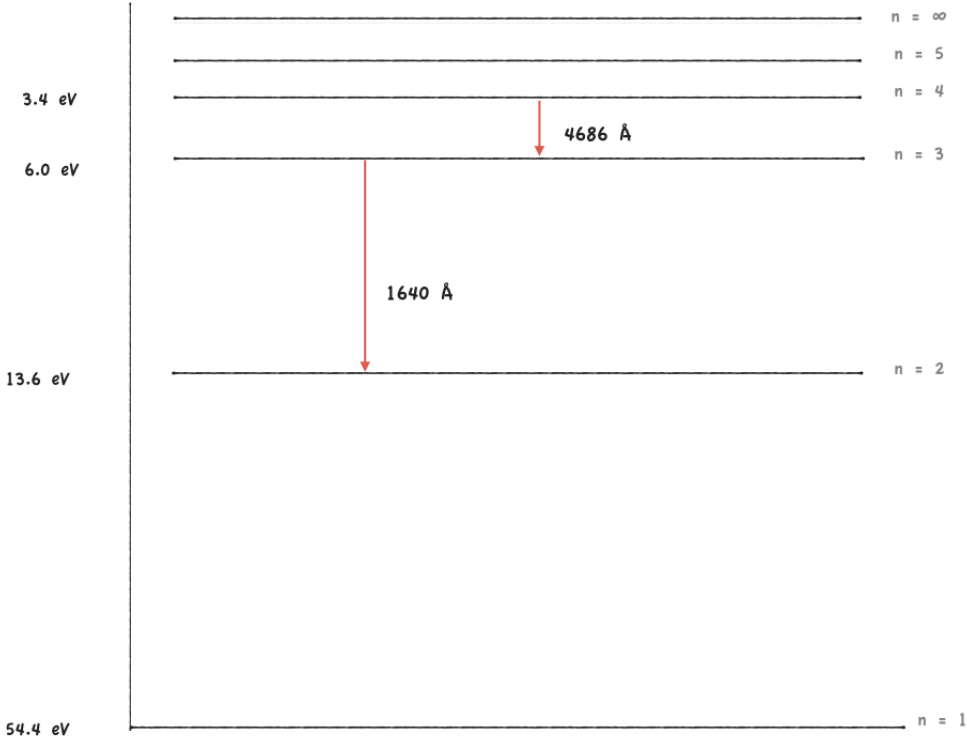


Figura 1.1: Diagrama de niveles de energía de He II para las línea UV ($\lambda 1640 \text{ \AA}$) y óptica ($\lambda 4686 \text{ \AA}$)

He^+ se requiere de fotones con altas energías ($E \geq 54.4 \text{ eV}$), i.e., con longitudes de onda $\lambda \leq 228 \text{ \AA}$. El principal mecanismo de formación de las líneas de He II es la recombinación de electrones libres con He^{++} para formar He^+ . Sin embargo, las líneas también pueden ser producidas por colisión de un electrón libre con un átomo de He^+ que es excitado al nivel relevante ($n=4$ en el caso óptico y $n=3$ en el caso UV) y luego produce las líneas en 4686 \AA (pasando el electrón excitado de $n=4$ a $n=3$) o 1640 \AA (si pasa de $n=3$ a $n=2$), como se muestra en la Figura 1.1; o por fluorescencia, en la que la excitación del electrón ligado al He^+ se debe a un fotón de la energía adecuada.

Las líneas de emisión de He II permiten estudiar el contenido en estrellas masivas ($> 8 M_\odot$) de galaxias cuyas estrellas individuales no están espacialmente resueltas (e.g. Hadfield & Crowther, 2006) y la retroalimentación de dichas estrellas al medio interestelar (e.g. Wofford et al., 2021). Por ejemplo, al disminuir la metalicidad de las estrellas, la tasa de fotones ionizantes de He^+ aumenta, esto sugiere que en galaxias dominadas por estrellas de Población III (libres de metales), se espera una fuerte emisión de He II (Schaerer, 2003). La detección de líneas de He II $\lambda 1640 \text{ \AA}$ con telescopios como el James Webb Space Telescope o futuros grandes telescopios terrestres, tales como el Extremely Large Telescope (ELT) y el Thirty Meter Telescope (TMT), impulsaría los estudios sobre estas poblaciones estelares. Una de las líneas de emisión de He II $\lambda 1640$ más lejana de un sistema dominado por formación estelar que se haya detectado proviene de la fuente CR7 OB3 que está localizada a $z \sim 6.6$ (Sobral et al., 2019; Matthee et al., 2020). En su tiempo, esta observación fue alentadora debido a que indicaba que la línea de He II podría ser detectada a mayores distancias, es decir, a edades más tempranas del Universo. De hecho, muy recientemente, el proyecto JWST Jades detectó una línea de He II en la galaxia GN-z11, localizada a $z=10.6$, la cual ha sido interpretada como evidencia de la presencia de estrellas de Población III (Maiolino et al., 2023).

En galaxias con formación estelar, una fuente de fotones con $E \geq 54.4$ eV son las capas calientes internas de las estrellas WR clásicas. Estas estrellas se caracterizan por poderosos vientos de alta velocidad que tienen grandes pérdidas de masa (Lamers et al., 1991). Los vientos son impulsados por la radiación. La aceleración de estos es proporcionada por la absorción de fotones en miles de líneas espectrales de los metales, que arrastra el resto del material a través de interacciones Coulombianas. Cuanto mayor sea la metalicidad, más eficiente es la transferencia de momento y energía al viento estelar, lo que resulta en mayores luminosidades de las líneas de He II ((Crowther & Hadfield, 2006); (Hainich et al., 2015)). De ahora en adelante, llamaremos a las líneas de emisión de He II anchas (~ 1000 km/S) formadas por recombinación en los vientos de las estrellas masivas, líneas de He II estelares. El análisis de estas líneas es importante debido a los estudios que se pueden realizar, por ejemplo, sobre el contenido de estrellas masivas (Hadfield & Crowther, 2006) y la atenuación del polvo en galaxias de formación estelar (Leitherer et al., 2019). En espectros ópticos de baja resolución espectral de galaxias con WR, el abultamiento azul cerca de He II 4686 Å es conocida en inglés como 'blue blump', y puede ser una combinación de líneas de N III 4640, C III/C IV 4650 y He II 4686 Å, dependiendo del tipo de WR que las están generando (e.g., (López-Sánchez & Esteban, 2010); (Gómez-González et al., 2021)). Por lo tanto, para estimar el número de WR de cada tipo usando espectros integrados de galaxias es importante tener buena resolución espectral.

Si suficientes fotones capaces de ionizar al He⁺ se escapan de los vientos estelares, se pueden producir zonas de emisión de He II cerca de la fuente. Esta emisión se muestra en los espectros de las galaxias como líneas de emisión de He II angosta (~ 100 km/s) denominado como He II nebular (e.g. López-Sánchez & Esteban, 2010; Mayya et al., 2020). El estudio de estas líneas puede ser usado, por ejemplo, para clasificar objetos según los cocientes de C IV $\lambda 1550$ y O III] $\lambda 1663$ con He II $\lambda 1640$ (Wofford et al., 2021). Sin embargo, en los artículos de esta tesis mostramos que el que las estrellas VMS y WN sean una fuente de fotones ionizantes de He II es un resultado controvertido. Por otro lado, en galaxias con formación estelar de extremadamente baja metalicidad no se detecta He II ancho, lo cual es debido a la menor presión radiativa de los metales en las estrellas masivas. Sin embargo, sí se observa emisión He II nebular extendida espacialmente (e.g. Wofford et al., 2021; Kehrig et al., 2021) que hasta la fecha no ha podido ser explicada.

Además de las estrellas masivas evolucionadas ya mencionadas, otras fuentes de fotones ionizantes de He⁺ son los discos de acreción de agujeros negros estelares en sistemas tipo High Mass X-ray Binary (por su nombre en inglés, e.g. Senchyna et al., 2020) o galácticos (e.g. Feltre et al., 2016); los choques donde la ionización de He⁺ se debe a la alta temperatura del gas (e.g. Alarie & Morisset, 2019; Plat et al., 2019); y las llamadas "stripped stars", que son estrellas despojadas de sus envolventes por la interacción con una compañera binaria (e.g. Götberg et al., 2018).

1.7. Modelos de síntesis de población estelar

En el segundo artículo de esta tesis se utilizaron modelos de síntesis de poblaciones estelares en el análisis. Durante las últimas cinco décadas, se han llevado a cabo estudios de poblaciones estelares en galaxias mediante el análisis de la luz integrada que emiten. Esto ha dado lugar al desarrollo de modelos de síntesis de poblaciones estelares, que incorporan diferentes funciones iniciales de masa (IMF, por sus siglas en inglés), trazas evolutivas para estrellas de diferentes masas, librerías de espectros estelares individuales, una historia de formación estelar y la metalicidad (Spinrad & Taylor, 1971; Faber, 1972; Bruzual-A., 1983; Schulz et al., 2002; Plat et al., 2019).

La historia de formación estelar (SFH, por sus siglas en inglés) nos habla de la formación

de estrellas como función del tiempo. La SFH puede considerar dos casos límites: el primero como poblaciones estelares simples (SSP, por sus siglas en inglés) que asume un brote de formación estelar, mientras que el segundo asume una producción continua de estrellas. La elaboración de modelos para poblaciones estelares enfrenta diversas limitaciones: la falta de isócronas, bibliotecas estelares empíricas y un mayor entendimiento de la física subyacente a la formación y evolución estelar. A pesar de estas dificultades, las poblaciones estelares son fundamentales para comprender observaciones de la distribución de energía de las estrellas (SED) en función de su edad y desarrollar modelos de poblaciones complejas.

Adicionalmente, para generar los modelos de síntesis de población estelar, es necesario tener otras consideraciones, por ejemplo la evolución en sistemas binarios, la rotación y la convección. Asimismo, es esencial comprender la distribución y evolución de la metalicidad, utilizar una ley de extinción adecuada y considerar la geometría del polvo cuando se compara con observaciones. Aunque combinar todos estos factores en los modelos resulta una tarea computacionalmente costosa, se han realizado esfuerzos para crear redes de modelos útiles (Leitherer et al., 1999; Bruzual & Charlot, 2003; Maraston, 2005; Vazdekis et al., 2010) que permiten el estudio de las poblaciones estelares utilizando los espectros integrados de galaxias con formación estelar.

Cada componente de los modelos de síntesis de población estelar enfrenta diversos desafíos que limitan el nivel de detalle con el que pueden ser desarrollados. Un ejemplo de esto es el cálculo de isocronas, que representan la ubicación de una estrella en el diagrama Hertzsprung-Russell (H-R) con una edad y metalicidad específicas. Estas isócronas se generan a partir de cálculos de evolución estelar que abarcan desde estrellas con la mínima masa para poder iniciar la combustión de hidrógeno hasta aquellas con una masa estelar máxima de al menos $100 M_{\odot}$.

Algunas de las isócronas más ampliamente utilizadas provienen de los modelos Padova (Bressan et al., 2012; Chen et al., 2015) y BaSTI (Pietrinferni et al., 2004; Cordier et al., 2007), los cuales cubren una amplia gama de fases evolutivas para diferentes edades y composiciones químicas. Asimismo, los modelos de Ginebra (Ekström et al., 2012; Georgy et al., 2012, 2013; Murphy et al., 2021; Eggenberger et al., 2021; Yusof et al., 2022), los cuales también incluyen la fase Wolf-Rayet, y los modelos de MESA (Dotter, 2016) y Bonn (Szécsi et al., 2022) también son muy usados.

Considerar todas las trazas evolutivas desarrolladas por diferentes modelos representa una tarea compleja debido a que cada uno de ellos adopta distintas consideraciones respecto a la tasa de pérdida de masa, la binariedad de las estrellas, la convección, la rotación y otros factores, que influyen en la edad en la que las estrellas evolucionan fuera de la secuencia principal. Estas suposiciones, que describen procesos físicos tridimensionales, se basan en códigos unidimensionales, lo que introduce incertidumbres en las isócronas y afecta las predicciones de los modelos de síntesis de población estelar.

Otros factores, como la rotación, ejercen un impacto directo sobre el tiempo que una estrella permanecerá en la secuencia principal, ya que la rotación induce una mezcla adicional de hidrógeno en la zona convectiva, lo que proporciona más material al núcleo convectivo. Asimismo, la rotación provoca una disminución en la gravedad superficial efectiva, lo que reduce la opacidad de la envolvente radiativa y aumenta la luminosidad. Estos efectos resultan en cambios en la predicción del número de estrellas supergigantes rojas y azules, así como en la cantidad y clase de estrellas Wolf-Rayet. Comparados con modelos sin rotación, las estrellas de los modelos que la incorporan generan un campo de radiación más duro y una mayor luminosidad bolométrica. Adicionalmente, producen modificaciones en los perfiles característicos de las estrellas Wolf-Rayet en espectros integrados (Levesque et al., 2012).

Otro aspecto crucial que afecta los observables y la evolución de las estrellas masivas es el intercambio de masa y la evolución de la envolvente común en la interacción entre estrellas binarias. Se ha destacado que los modelos que incorporan la evolución de estrellas binarias ajustan mejor algunas observaciones en el ultravioleta (Eldridge & Stanway, 2012) pero no a otras (Wofford et al., 2021).

La tasa de pérdida de masa es otro ingrediente importante en el desarrollo de los modelos de evolución estelar. Para estrellas masivas, se cree que el mecanismo de pérdida de masa ocurre mediante vientos impulsados por la absorción de fotones dada las muchas transiciones de líneas en metales, mientras que para masas menores los vientos son impulsados por polvo originado en pulsaciones (Willson, 2000). Para masas $M \leq 8 M_{\odot}$, la tasa de pérdida de masa determina el tiempo de vida de las estrellas antes de convertirse en enanas blancas, así como la masa que alcanzarán. Por otro lado, para masas superiores, esta tasa de pérdida de masa afecta directamente las predicciones de las fases evolutivas más avanzadas.

Un ingrediente esencial en los modelos de síntesis de población estelar son las bibliotecas de espectros estelares. Por un lado, existen bibliotecas teóricas que abarcan un amplio espacio de parámetros, como la resolución espectral, la gravedad y la temperatura efectiva. Estos espectros no requieren calibración en flujo ni considerar la absorción atmosférica. Sin embargo, dependen fuertemente de la calidad de los parámetros atómicos y moleculares, así como de las suposiciones sobre convección y microturbulencia utilizadas. Por otro lado, las bibliotecas empíricas no enfrentan estos problemas, pero están limitadas por restricciones observacionales, como la resolución espectral, los rangos limitados de longitud de onda, la calibración de flujo y la absorción atmosférica. Además, algunas de ellas no pueden cubrir un amplio rango de parámetros estelares, pues aunque algunas librerías como XSHOOTU y VLT-FLAMES Tarantula Survey (VFTS) exploren estrellas de baja metalicidad en las nubes de Magallanes, muchas otras se basan en estrellas cercanas a nuestra Galaxia, que tienen un número reducido de estrellas de baja metalicidad en la secuencia principal y pocas estrellas evolucionadas.

Como se dijo anteriormente, otro componente de gran importancia para el desarrollo de los modelos de síntesis de población estelar es la Distribución Inicial de Masas (IMF, por sus siglas en inglés), que ha sido objeto de numerosos estudios (Salpeter, 1955; Scalo, 1986; Kroupa, 2001; Chabrier, 2003). La IMF determina, en el contexto de los modelos de SSP, la tasa de evolución de la luminosidad para una población que evoluciona pasivamente, así como la normalización de la relación entre masa y luminosidad estelar. Además, la IMF afecta la distribución de energía espectral de poblaciones estelares compuestas y contribuye a la forma de la Distribución Espectral de Energía.

Dado el número de factores que requieren ser implementados en los modelos de síntesis de poblaciones, la labor de integrar todos en una sola red de modelos es complicada, sin embargo, en los últimos años se han realizado esfuerzos para implementar más ingredientes a los ya desarrollados. En esta tesis se hizo uso de los modelos de Charlot y Bruzual (Plat et al., 2019), que cubren en detalle la evolución de estrellas O y B, además de incluir la fase Wolf-Rayet y han extendido la masa límite de las estrellas hasta $300 M_{\odot}$. Para más información, ver sección 3 del segundo artículo.

1. Looking for nebular He II emission south of the multiple-massive star system, HD 5980

1.1. Resumen

Las observaciones de la línea de emisión nebulosa He II λ 4686 (óptico) o su equivalente en el ultravioleta (He II λ 1640) en galaxias con formación estelar a grandes distancias pueden utilizarse para determinar las propiedades de las fuentes de fotones ionizantes de He⁺. En algunas galaxias cercanas con estallidos de formación estelar, la línea de emisión nebulosa de He II λ 4686 presenta una componente ancha, cuyo origen generalmente se atribuye a formación en los vientos de estrellas Wolf-Rayet de subtipo WN. Dada la naturaleza de formación de las líneas de He II, resulta importante conocer si las estrellas masivas son buenas candidatas a fuentes de fotones ionizantes de He⁺.

Para esto se pueden realizar estudios sobre las líneas observadas de He II, haciendo uso de modelos de síntesis de poblaciones estelares que predicen la contribución de las estrellas al flujo emergente, y modelos de fotoionización que predicen la contribución del gas. Fuentes alternativas de fotones con energía mayor que 54.4 eV, necesarios para ionizar dos veces el helio, pueden ser los discos de acreción alrededor de agujeros negros, los choques radiativos rápidos y estrellas masivas que han perdido su envolvente de hidrógeno debido al intercambio de masa con su compañera binaria, convirtiéndose en estrellas calientes y compactas, llamadas binarias despojadas (stripped stars).

En este trabajo, examinamos observaciones de rendija larga obtenidas con el *Focal Reducer and low dispersion Spectrograph* (FORS1) en el Very Large Telescope (VLT) para buscar emisión nebulosa de He II λ 4686 al sur del sistema múltiple HD 5980 en la Nube Menor de Magallanes, formado por dos estrellas WN: WN6h + WN6-7 y una estrella tipo O. Nuestros resultados muestran sólo una emisión ancha de He II λ 4686 hasta aproximadamente 7.6 pc del sistema. Una comparación con observaciones obtenidas con el Space Telescope Imaging Spectrograph (STIS) del telescopio espacial Hubble, en una fase orbital similar, indica que la emisión ancha de He II medida con FORS1 es probablemente contaminación procedente del sistema estelar múltiple HD 5980.

Utilizando modelos de atmósferas estelares, mostramos que no se espera ningún flujo ionizante de He⁺ significativo proveniente de las estrellas WN en HD 5980. Además, cuando estrellas similares están presentes en una población estelar coetánea, las estrellas O pueden ser los principales contribuidores a la radiación de He⁺ ionizante. Ahora bien, utilizando modelos de síntesis de población estelar (SSP, por sus siglas en inglés) de dos diferentes códigos, Starbursts99 (Leitherer et al., 2010) y, Charlot y Bruzual (Plat et al., 2019), observamos un aumento de la tasa de fotones ionizantes de He⁺ cuando las estrellas WN y WC aparecen, planteando un escenario diferente al encontrado en los modelos de evolución estelar. Por otro lado, diferentes autores han encontrado que los modelos de SSP presentan problemas al determinar el número de estrellas WR comparado con las predichas con las observaciones. Un ejemplo de esto se presenta en Doran et al. (2013) donde se encontraron solo 7 estrellas WR clásicas en NGC 2070, en la Nube Mayor de Magallanes, un número menor al predicho por modelos de

síntesis de población estelar BPASS (Bestenlehner et al. (2020)). De la misma manera, Mayya et al. (2020) realizó un estudio en el súper cúmulo estelar A en la galaxia enana NGC 1569, donde utilizó el cociente de la línea de He II λ 4686 observada y la luminosidad típica de una estrella WNL para estimar el número de estrellas WR, encontrando valores consistentes con los predichos por Starburst99, pero mucho mayores a los encontrados en el cúmulo NGC 2070, que tiene una masa similar. Finalmente, conociendo la existencia del remanente de supernova SNR B0057-724 al sur de HD 5980, utilizamos cocientes típicos de líneas en el diagrama BPT para comparar nuestras observaciones con la malla de modelos de choque 3MdB (Alarie & Morisset (2019)), descartando así la posibilidad de que la emisión de He II observada tenga una contribución del remanente de supernova.

1.2. Contribución

Los datos utilizados para este primer trabajo fueron observaciones de rendija larga ($0.51'' \times 410''$) del FORS1 en el VLT de la región H II, NGC 346. La rendija fue ubicada en tres diferentes posiciones dentro de la nebulosa (Tabla 1 del artículo). Busqué en la literatura, y catálogos disponibles, estrellas masivas identificadas en NGC 346 para ubicar aquellas que se encuentran dentro de las posiciones de la rendija utilizadas, encontrando las compilaciones de Massey & Duffy (2001) y Dufton et al. (2019) para estrellas tipo O y WR, así como la base de datos de HST ULLYSES (Roman-Duval et al., 2020) en el UV. Solo encontré estrellas de las dos últimas referencias dentro de las posiciones de la rendija, siendo una de ellas el sistema estudiado HD 5980. Así mismo, como se sugiere en (Reid et al., 2006), localicé la posición del remanente de supernova SNR B0057-724.

Para corroborar que la determinación de la posición de la rendija fue adecuada, comparamos nuestras observaciones con espectros de VLT Flames-Medusa (proporcionados por Philip Dufton y Chris Evans), el cual tiene fibras con un diámetro de $1.2''$. Es así que utilizando las imágenes 2-dimensionales (ver artículo asociado: Figura 2) de la posición C de la rendija (ver artículo asociado: Figura 1), seleccioné rectángulos de 6 píxeles, correspondientes a los $1.2''$ de diámetro en VLT Flames-Medusa, sobre las trazas espectrales más brillantes, realizando finalmente la extracción de los espectros. Identifiqué los espectros correspondientes a fuentes dentro de los catálogos de estrellas masivas antes mencionados, desenrojecí y apliqué una corrección por desplazamiento al rojo derivado de la línea de emisión nebulosa de [Ar IV] λ 4740, la cual previamente medí ajustando una gaussiana.

Una vez asegurada la posición de la rendija, utilicé los espectros bidimensionales azul, rojo y baja dispersión de la posición C (ver detalles en sección 2 del artículo) para extraer 34 espectros de cada grisma, tomando rectángulos de 6 píxeles a lo largo de la rendija ($0.15 \text{ pc} \times 1.48 \text{ pc}$) y haciendo uso de una rutina desarrollada en python. Comparé espectros derivados de la rutina apall de IRAF en (Valerdi et al., 2019) con espectros obtenidos con la rutina de python tomando las mismas condiciones de extracción, esto con el objetivo de darle fidelidad al algoritmo desarrollado en python (ver Figura A1 en los apéndices del artículo asociado). Adicionalmente, utilicé estos espectros prueba para realizar una calibración del flujo mediante la determinación de un factor de conversión de cuentas de píxel a unidades de flujo, dicho factor es de $2.36 \times 10^{-15} \text{ erg s}^{-1} \text{ cm}^{-2} \text{ \AA}^{-1}$. Este procedimiento fue necesario debido a que los archivos fits no contienen la información para realizar la calibración del flujo. Una vez finalizado lo anterior, uní los espectros proporcionados por el grisma azul y rojo como se describe en el apéndice B del artículo. Corregí por enrojecimiento y desplazamiento al rojo cada uno de los espectros de las 34 extracciones mencionadas previamente.

Tomando en cuenta cada uno de los espectros extraídos, ajusté funciones gaussianas a diferentes líneas de emisión, principalmente He II λ 4686 y las necesarias para el diagrama BPT. Para la línea de He II, obtuve los parámetros de amplitud, FWHM y EW, lo que me permitió

determinar que no se detecta He II nebular. Utilizando los espectros con una SNR ≥ 5 , observé que la emisión estelar de He II se extiende ~ 15 pc a lo largo de la rendija (ver Figura 7 en artículo asociado).

El ajuste de la máxima emisión de He II (es decir, la más cercana al sistema múltiple HD 5980) necesitó dos funciones gaussianas. Para descartar la posibilidad de estar observando las dos componentes WN del sistema, calculé la fase orbital tomando en cuenta la fecha de nuestras observaciones (sección 4.2 del artículo) y la comparé con la presentada en (Hillier et al., 2019). Por otro lado, utilicé observaciones HST/STIS Hillier et al. (2019) centradas en HD 5980, dónde caractericé el perfil de He II $\lambda 4686$ y comparé la morfología con la máxima emisión de He II de nuestras observaciones (ver sección 4.3 del artículo para más detalles) mostrando que son muy similares.

Puesto que la remanente de supernova SNR B0057-724 se encuentra al sur del sistema, utilicé modelos de choques de la base de datos 3MdB Alarie & Morisset (2019), para descartar la posibilidad de que las observaciones estuvieran afectadas por la emisión de la remanente. Para esto medí y comparé, mediante diagramas de diagnóstico, las líneas de [O III], [N II] y [S II] de nuestras observaciones, con las obtenidas en los modelos, descartando así que la emisión de la SNR contamine nuestras observaciones (ver sección 5.3 del artículo para más detalles).

Finalmente, para verificar que contábamos con la posibilidad de detectar He II nebular, sumé la línea de [Ar IV] $\lambda 4740$ a la máxima emisión de He II $\lambda 4686$ de nuestras observaciones, elegimos la línea de [Ar IV] basados en la figura 1 de (López-Sánchez & Esteban, 2010), donde la línea nebular de He II tienen flujos similares a [Ar IV]. Ajusté la emisión combinada, observando que son necesarias tres componentes gaussianas para reproducir la nueva emisión, concluyendo que tenemos la posibilidad de detectar emisión nebular de He II del orden de la línea de [Ar IV] (ver último párrafo de la sección 5.3 del artículo).

Para cada uno de los resultados y trabajo realizado, escribí las secciones correspondientes en el artículo, y realicé las gráficas asociadas. Me encargué del envío del mismo y de los comentarios del árbitro.

Looking for nebular He II emission south of the multiple-massive star system, HD 5980

A. Sixtos¹,¹★ A. Wofford¹,¹★ A. A. C. Sander²,² and A. Peimbert³,³★

¹Instituto de Astronomía, Universidad Nacional Autónoma de México, Unidad Académica en Ensenada, Km 103 Carr. Tijuana–Ensenada, Ensenada, B.C., C.P. 22860, México

²Zentrum für Astronomie der Universität Heidelberg, Astronomisches Rechen-Institut, Mönchhofstr 12-14, D-69120 Heidelberg, Germany

³Instituto de Astronomía, Universidad Nacional Autónoma de México, Apdo. Postal 70-264, Ciudad de México 04510, México

Accepted 2022 December 11. Received 2022 December 8; in original form 2022 February 17

ABSTRACT

The nebular He II $\lambda 1640$ emission line is observed in star-forming galaxies out to large distances and can be used to constrain the properties of sources of He⁺-ionizing photons. For this purpose, it is crucial to understand which are the main stellar sources of these photons. In some nearby metal-poor starburst galaxies, nebular He II $\lambda 4686$ (optical equivalent) is accompanied by a broad underlying component, which is generally attributed to formation in the winds of classical (He-burning) Wolf–Rayet stars, primarily of the WN subtype. In such cases, the origin of the nebular component has been proposed to be the escape of He⁺-ionizing photons from the winds of the WN stars, at least partially. We use archival long-slit observations obtained with Focal Reducer Low Dispersion Spectrograph (FORS1) on the Very Large Telescope to look for nebular He II $\lambda 4686$ emission south of the WN6h + WN6-7 close binary in HD 5980. We only find broad He II $\lambda 4686$ emission, as far as ~ 7.6 pc from the binary. A comparison with observations obtained with Space Telescope Imaging Spectrograph (STIS) on the *Hubble Space Telescope*, at a similar orbital phase, shows that the FORS1 broad He II emission is likely contamination from the multiple-star system HD 5980. We use models to show that no significant He⁺-ionizing flux is expected from the WN stars in HD 5980 and that when similar stars are present in a coeval stellar population, the O stars can be far greater emitters of He⁺-ionizing radiation.

Key words: binaries: eclipsing – stars: individual: HD 5980 – stars: Wolf–Rayet – H II regions – Magellanic Clouds.

1 INTRODUCTION

1.1 Nebular He II from star-forming objects

The presence of narrow (full width at half-maximum, FWHM < 1000 km s⁻¹) nebular He II emission lines at 4686 Å (optical) and/or 1640 Å (ultraviolet, UV) in the integrated spectrum of a galaxy indicates the existence of a hard ionizing source, as photons of ≥ 54.4 eV ($\lambda \leq 228$ Å) are required to ionize He⁺. It is the recombination of free electrons with He²⁺ that produces the He II emission lines. Active galactic nuclei (AGNs) are sources of hard radiation and produce luminous He II emission in galaxies (e.g. Shirazi & Brinchmann 2012; Saxena et al. 2020). However, nebular He II emission is also observed in star-forming (SF) galaxies without AGN signatures, particularly at subsolar metallicities (e.g. Shirazi & Brinchmann 2012; Senchyna et al. 2017; James et al. 2022), and as far as redshifts of $z \sim 2$ –3, e.g. in galaxies of the VANDELS survey, which used VIsible MultiObject Spectrograph (VIMOS) on the Very Large Telescope (VLT; Saxena et al. 2020). At even higher distances, in the epoch of reionization (EoR), tentative detections of He II emission from SF objects include (i) A1703-zd6 at $z \sim 7$, observed with Multi-Object Spectrometer for Infra-Red Exploration First Light Obtained (MOSFIRE) on Keck (Stark et al. 2015);

(ii) CR7 OB3 at $z \sim 6.6$, observed with XShooter on the VLT (Sobral et al. 2019); and (iii) a galaxy at $z = 6.112$, observed with NIRCam on the JWST, as part of the commissioning of the wide-field slitless spectroscopy mode. These tentative He II detections are promising for the ongoing JWST NIRSpec GTO programme, JWST Advanced Deep Extragalactic Survey (JADES), which will observe the He II $\lambda 1640$ line of galaxies in the EoR (leads, M. Rieke and P. Ferruit), and future observations with extremely large (≥ 20 m in diameter) ground-based telescopes. Thus, in principle, the nebular He II lines can be used to identify and constrain the properties of sources of hard ionizing radiation in SF galaxies over a large range of distances. For this purpose, it is crucial to understand which are main sources of these photons in these galaxies. In Section 1.2, we summarize some of the work attempting to constrain the properties of sources of He⁺-ionizing radiation in nearby galaxies.

1.2 Sources of He⁺-ionizing photons in nearby SF galaxies

Two of the nearest, most metal-poor starburst galaxies known, I Zw 18 and SBS 0335–052E, show strong extended nebular He II emission (e.g. Izotov et al. 2006; Kehrig et al. 2015; Kehrig et al. 2018). In these two galaxies, AGNs, high-mass X-ray binaries (HMXBs), and fast radiative shocks have been excluded as dominant sources responsible for the nebular He II emission (Kehrig et al. 2021; Wofford et al. 2021). Of the two galaxies, SBS 0335–052E is the most luminous in integrated nebular He II emission. Wofford et al. (2021) use observations of this galaxy with the Cosmic Origins

* E-mail: jasixtos@astro.unam.mx (AS); awoffor@astro.unam.mx (AW); antonio@astro.unam.mx (AP)

Spectrograph (COS; PI: Wofford, PID: 13788) on the *Hubble Space Telescope (HST)*, and the models of Gutkin, Charlot & Bruzual (2016), which account for single non-rotating stars of up to $300 M_{\odot}$ and the ionized gas, to show that simultaneously reproducing the fluxes of all high-ionization UV lines observed with COS, including the He II $\lambda 1640$ emission line, requires an unphysically low metallicity. Wofford et al. (2021) also present observations of the galaxy with the Multi-Unit Spectroscopic Explorer (MUSE) on the VLT and show that the observed He II $\lambda 4686/H\beta$ ratio cannot be reproduced with simple stellar population (SSP) Binary Population and Spectral Synthesis (BPASS) v2.1 models that account for massive star evolution in close binaries (Eldridge et al. 2017) and the ionized gas (Xiao, Stanway & Eldridge 2018).

Senchyna et al. (2020) argue that HMXB populations may not be sufficient to account for the observed He II line strengths in nearby metal-poor galaxies, and that revised stellar wind models or inclusion of softer X-ray sources may be needed. Stars that have been stripped of their envelopes via an interaction with a binary companion and which emit a significant portion of their radiation as ionizing photons (Götberg et al. 2019) have been proposed as alternative sources of He⁺-ionizing photons in SF galaxies (Senchyna et al. 2017). Evidence for the existence of these stars is hard to obtain but some has been collected (Wang et al. 2021). However, comparisons of observations with predictions from population synthesis models that account for stripped-binary products have yet to demonstrate that such products generate sufficient He⁺-ionizing flux to explain the observations of SBS 0335–052E, for instance. As an alternative mechanism, Garnett et al. (1991) suggest that fast radiative shocks due to supernova explosions can produce relatively strong He II emission in giant H II regions under certain conditions. Plat et al. (2019) successfully reproduce high-ionization UV nebular emission lines of metal-poor galaxies, including He II lines, with a combination of fast radiative shocks and photoionization by single non-rotating massive stars. In the latter work, massive stars are needed, at least partially, but which is the stellar type that contributes the most to the He⁺-ionizing flux?

1.3 Nebular He II due to Wolf–Rayet stars

Wolf–Rayet (WR) galaxies (Schaerer, Contini & Pindao 1999) are SF galaxies that show signatures of the presence of WR stars. WR stars are descended from O-type stars with initial masses of $\gtrsim 25 M_{\odot}$ (depending on metallicity) and are divided into those with strong optical lines of helium and nitrogen (WN subtype) and those with strong helium, carbon, and oxygen (WC and WO subtypes). The WN subtype is further divided based on the value of N III–N V and He I–He II optical-line ratios, into ranges from WN2 to WN5 for ‘early WN’ (WNE) stars and WN7 to WN9 for ‘late WN’ (WNL) stars, with WN6 stars being either early or late type (Crowther 2007).

In order to produce detectable stellar (broad) He II emission, at least one of the following conditions must be met: the stars must be hot to doubly ionize He and the mass-loss rates must be high to produce dense winds. Since classical (He-burning) WR stars (cWR) meet these two conditions, the presence of broad He II is generally thought to indicate the presence of these stars. In addition, H-rich very massive stars (VMSs), which have masses of $M > 150 M_{\odot}$, have WR features as well. Wind signatures from VMSs have been detected in 30 Dor (Crowther et al. 2016; Brands et al. 2022) and two starburst galaxies (Wofford et al. 2014; Smith et al. 2016). For reference, seven VMSs dominate the stellar He II $\lambda 1640$ and C IV 1550λ emission of 70 far-UV-bright stars in the core of star cluster

NGC 2070, located in the Large Magellanic Cloud (LMC; Crowther et al. 2016).

Some nearby SF galaxies with nebular He II $\lambda 4686$ detections are accompanied by an underlying blue bump (e.g. Guseva, Izotov & Thuan 2000; López-Sánchez & Esteban 2010; Kehrig et al. 2016; Mayya et al. 2020) that is generally associated with He II $\lambda 4686$ blended with additional contributions from N III $\lambda 4640$ in WN stars and/or C III/C IV 4650 in WC stars. These WR galaxies may also show a red WR bump, composed by the broad C IV $\lambda 5808$ line that is mainly observed in WC stars (López-Sánchez & Esteban 2010).

When both stellar and nebular He II $\lambda 4686$ emission are observed in SF galaxies, the nebular component is sometimes attributed, at least partially, to the escape of He⁺-ionizing photons from the WR star winds (e.g. Guseva et al. 2000; Kehrig et al. 2016; Mayya et al. 2020). Schaerer & Vacca (1998) synthesized the nebular and WR He II $\lambda 4686$ emission from low-metallicity young starbursts ($Z \vee Z_{\odot}/5$) and found that the nebular He II emission is associated with the presence of WC/WO stars and/or hot WN stars evolving to become WC/WO stars. For WR stars, the production of He⁺-ionizing flux is a matter of wind strength. As a rule of thumb, stellar evolution models predict He⁺-ionizing flux for WN2 (i.e. early, nitrogen-rich, classical WRs), WN3ha (i.e. early, nitrogen-rich WRs showing H lines in emission and absorption), and WO (i.e. hot evolved stars showing strong oxygen emission lines) stars, but not for other WRs or VMSs. In some works, however, the nebular He II emission is associated with the presence of WNL stars (e.g. Mayya et al. 2020). Do observations of the Small Magellanic Cloud (SMC) show the same result?

1.4 NGC 346

Due to its proximity, massive star content, and low metallicity, the young massive cluster (YMC; Portegies Zwart, McMillan & Gieles 2010) NGC 346 is a unique target to address this question.

NGC 346 is located in the SMC, at only 61 ± 1 kpc (Hilditch, Howarth & Harries 2005), specifically in SF complex LHA 115-N66, whose radius is 3.5 arcmin (Relaño, Peimbert & Beckman 2002) and is the brightest H II region of the SMC (Henize 1956). The cluster has an age of $\sim 3 \pm 1$ Myr (Sabbati et al. 2007) and a present-day mass function in the range from 0.6 to $60 M_{\odot}$ that is in agreement with the Salpeter stellar initial mass function (Sabbati et al. 2008). Its total mass, $3.9 \times 10^5 M_{\odot}$ (Sabbati et al. 2008, table 1), makes it the most massive YMC of the SMC (Gouliermis & Hony 2015) and comparable in mass to spatially unresolved YMCs in some nearby SF and starburst galaxies (e.g. Adamo et al. 2017). The ionized-gas oxygen abundance of NGC 346 is about one-third that of the sun’s photosphere¹ (Valerdi et al. 2019, hereafter V19). The latter value is in agreement with the oxygen abundance of massive stars in the SMC (Bouret et al. 2013) and specifically NGC 346 (Rickard et al. 2022).

1.5 HD 5980

NGC 346 hosts a multiple-massive star system, HD 5980, which is of great interest for understanding massive star evolution and binary black hole formation. HD 5980 is composed of three massive stars. Its first component, star A, is a massive ($60 \pm 10 M_{\odot}$) star that went through the eruptive luminous blue variable (LBV) phase during 1993–1994, and that now has a spectrum corresponding to that of a

¹We adopt the photospheric solar oxygen abundance of Asplund et al. (2009), which is $12 + \log(O/H) = 8.69$.

WN6h. Its second component, star B, is a close, eclipsing companion of similar spectral type (WN6-7) and mass ($66 \pm 10 M_{\odot}$). The spectral types are those from Shenar et al. (2016). The masses of stars A and B are determined in Koenigsberger et al. (2014). Stars A and B orbit around each other with a period and eccentricity of $P_{AB} = 19.3$ d and $e = 0.3$, respectively. The spectrum of HD 5980 has a third component, star C, believed to be itself a binary system containing a late O-type supergiant. This is shown in Hillier et al. (2019), who used CMFGEN (Hillier & Lanz 2001) models to fit *HST*/STIS UV observations of HD 5980 (PI: Koenigsberger, PID: 13373, date of observation: 2014 March 24), in particular, its broad He II $\lambda 1640$ emission and C IV $\lambda\lambda 1548, 1551$ and N IV $\lambda\lambda 3479–3485$ P Cygni-like profiles. Using the 2014 data, Hillier et al. (2019) found that when Star A (the LBV) eclipses Star B, the fitted mass-loss rate and luminosity have the lowest values ever determined for such spectra. They also found that as the mass-loss rate decreases, the difference between the observed and model P Cygni profiles increases. They suggest that the discrepancy between the model and the observation could be due to an asymmetry of the wind that is not included in the model and that is due to the perturbation of the winds of the LBV and WR star by the radiation of an O supergiant plus the wind–wind interaction.

1.6 Nebular He II observations in NGC 346

NGC 346 is the target of two large massive star spectroscopic surveys, one that is ongoing ('Ultraviolet Legacy Library of Young Stars as Essential Standards, ULLYSES'; Roman-Duval et al. 2020) and the other that recently completed ('X-Shooting ULLYSES, XShootU'; Vink et al., in preparation). ULLYSES is a Director's Discretionary programme that is collecting data for about 250 OB stars in low-metallicity regions of Local Group galaxies, using either COS or STIS on *HST*, and far- and near-UV gratings: COS G130M, COS G160M, STIS E140M, COS G185M, and STIS E230M. XShootU obtained medium-spectral resolution spectroscopy with the X-Shooter instrument on the VLT. This slit-fed (11 arcsec slit length) spectrograph provides simultaneous coverage of the wavelength region between 300 and 2500 nm, divided into three arms: UVB ($300 \text{ nm} \lesssim \lambda \lesssim 500 \text{ nm}$), VIS ($500 \text{ nm} \lesssim \lambda \lesssim 1000 \text{ nm}$), and NIR ($1000 \text{ nm} \lesssim \lambda \lesssim 2500 \text{ nm}$). Unfortunately, the apertures of the UV and optical observations from the above surveys are not optimized to study nebular He II in the vicinity of HD 5980. In addition, there are archival *HST*/STIS UV (PI: Oskinova, PID: 15112) and VLT/MUSE optical (PI: Hamann, PID: 098.D-0211) observations of NGC 346. However, these observations targeted the O-star population (Rickard et al. 2022) and thus avoided the area near HD 5980.

On the other hand, V19 determined the ionized-gas oxygen abundance and primordial helium abundance of the ionized nebula surrounding NGC 346 using long-slit optical observations at three different positions, obtained with the Focal Reducer Low Dispersion Spectrograph (FORS1) of the VLT. In order to measure the nebular He, they required accurate measurements of the nebular He⁺⁺ lines. Since the presence of stellar lines would impact the accuracy of these measurements, V19 discarded regions along the slits containing stars or broad He II emission, in particular, a region with broad He II emission that is located at a projected distance of ~ 1.2 pc south of HD 5980. In this paper, we use the FORS1 observations to look for nebular He II emission south of HD 5980.

1.7 This paper

The paper is organized as follows: In Section 2, we present the FORS1 observations, determine the distance between HD 5980

and the nearest slit, and compare the seeing of the corresponding observation to this distance. Although the FORS1 observations are not optimized for massive stars, in Section 3, we present massive star spectra extracted from the FORS1 slits, compare a subsample of the spectra to archival VLT FLAMES (Fibre Large Array Multi-Element Spectrograph) observations, and use this comparison as a second check of our slit position determinations. Although our main interest is in the blue-grism FORS1 data, we also provide a brief discussion of the available red-grism spectra in the context of massive stars. In Section 4, we characterize and analyse the He II emission observed with FORS1 and south of HD 5980. In Section 5.2, we discuss whether nebular He II emission is expected south of HD 5980 based on predictions from individual star models. We also discuss these predictions in the context of SF galaxies. In addition, we analyse the effect of the SNR located south of HD 5980. Finally, in Section 6, we provide a summary and conclusions.

2 OBSERVATIONS AND STANDARD DATA REDUCTION

2.1 Observations

We use VLT FORS1 observations obtained on 2002 September 9, as part of programme 440 (PI: Peimbert). The observations include a direct *V*-band image with a plate scale of 0.2 arcsec/pixel, and long-slit ($0.51 \text{ arcsec} \times 410 \text{ arcsec}$) optical spectra covering three different locations in NGC 346. Spectra were obtained at each location with three grism/filter combinations: 300V/GG375 (3440–7600 Å, $R \sim 700$); 600B + 12 (3560–5974 Å, $R \sim 1300$); and 600R + 14/GG435 (5330–7485 Å, $R \sim 1700$). Hereafter, we will refer to the corresponding observations as the low-dispersion, blue-, and red-grism spectra, respectively. The resolution of the blue grism is 230.5 km s^{-1} and is enough to distinguish between narrow and broad He II emission. The data were reduced using IRAF and a standard procedure (bias, dark and plane correction, wavelength calibration, and flux calibration).

The left-hand panel of Fig. 1 shows the *V*-band image of NGC 346 with the slit footprints overlaid. Following V19, we use A, B, and C to identify the different slit positions. In the figure, we also indicate the locations of HD 5980 and SNR B0057–724. For slit C, we show windows that are 5 arcsec in length and whose height has been enlarged for clarity. In Section 4, we extract spectra from these windows in order to characterize the He II emission south of HD 5980. The right-hand panel of Fig. 1 shows a zoomed-in version of the area around HD 5980 covering windows 17 to 26 on slit C, and the position of star 1070 that is mentioned in Section 3.

2.2 Determination of FORS1 slit positions relative to stars

The positions of the slit centres that are reported in V19 are only approximate. We need to know the positions of the slits more accurately in order to determine whether known massive stars are located within the slits. This is particularly important for better interpreting the properties of the He II emission south of HD 5980. In order to find the slit positions, we use a similar procedure to that of Wofford, Leitherer & Chandar (2011). The method relies on the fact that at the correct slit position, the stars in the direct image that are located within the slit should align with spectral traces of the 2D-spectral image. Thus, we compare the positions of the stars in the *V*-band image and the blue spectra. For each of slits A, B, and C (from top to bottom), the left-hand panel of Fig. 2 shows a portion of the *V*-band image that includes the relevant slit, while the right-hand

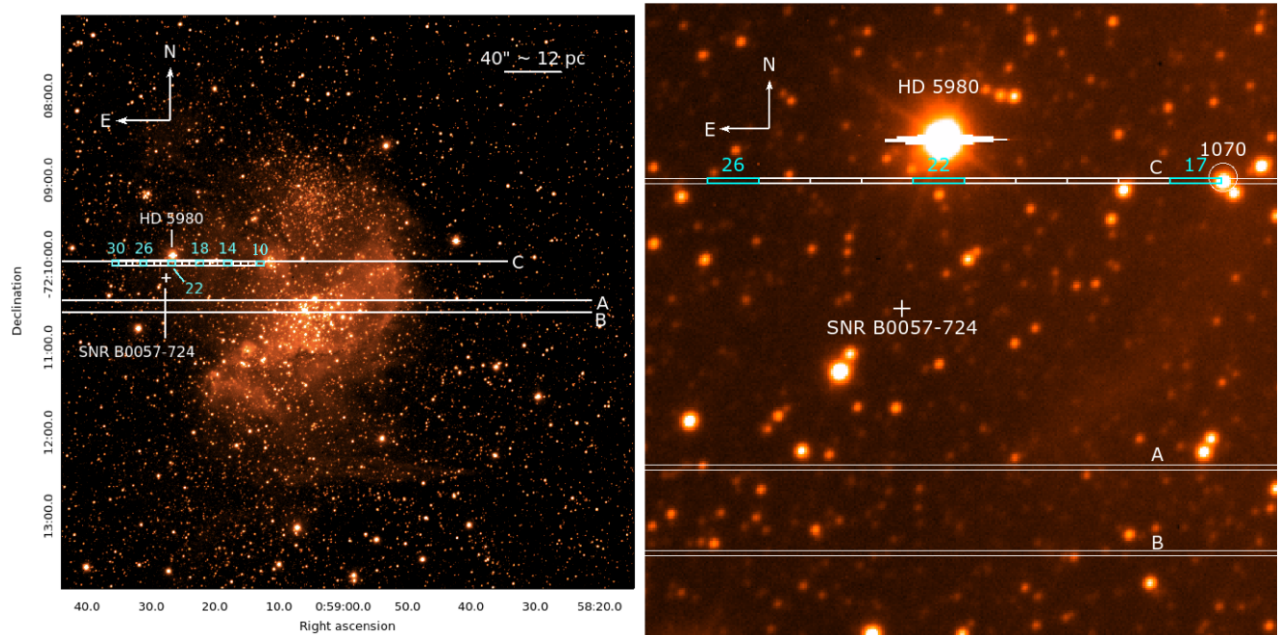


Figure 1. Left: VLT FORS1 V-band image of NGC 346 in logarithmic scale. We overlay the footprints of the 0.51 arcsec \times 410 arcsec slits at the positions that were determined in this work. We indicate the positions of HD 5980 (Hillier et al. 2019) and SNR B0057–724 (Reid et al. 2006). For slit C, we show 20 spectral extraction windows of 5 arcsec in length and height enlarged for clarity, which we use to study the He II emission south of HD 5980. The cyan numbers are the window IDs. At the adopted distance of NGC 346 (61 kpc), 40 arcsec represents 11.83 pc and slit C is 1.2 pc from HD 5980. Right-hand panel: Zoomed-in version of the area around HD 5980 covering windows 17 to 26 on slit C and the position of star 1070, which is mentioned in Section 3.

panel shows a portion of the 2D spectrum corresponding to that slit. The slit positions that are reported in V19 are shown with vertical-dashed lines, while the positions found in this work (hereafter, S22) are shown with vertical-solid lines. Table 1 gives the V19 and S22 slit centre positions. For the three slits, the differences in declinations between V19 and S22 are about 3.2 arcsec. We estimate that our slit declinations are accurate within ± 0.6 arcsec (3 pixels), which is about the width of the slit. No significant adjustment in RA was necessary.

In Fig. 2, we use the star IDs of Dufton et al. (2019, hereafter, D19) to mark the positions of their stars within our slits. If the star is part of the ULLYSES survey, then we add an asterisk to the star ID. This is the case for HD 5980 and NGC346 435 (1001, according to D19). The figure shows that spectral traces are brighter when the star is located within the slit, and fainter when the star is either located just outside the slit (e.g. star 1064 in the top panels) or there is nebular plus stellar emission, as is the case for HD 5980 (bottom panels of Fig. 2). The type of star also affects the brightness of the spectral trace. Note that the spectral trace of HD 5980 in the bottom-right panel shows strong He II $\lambda 4686$ emission.

Fig. 3 shows that the S22 slit positions yield a good match between intensity peaks due to the presence of stars in the direct image (middle panels) and due to the presence of spectral traces (bottom panels). The figure also shows that the V19 slit positions do not yield good matches. The plots of Fig. 3 are obtained by fixing the row number and summing the counts in the relevant columns of the image. For the top and middle panels, the columns are those within each slit. For the bottom plots, we sum the counts of columns 800 to 850, which span a wavelength interval that is free of bright emission lines (see right-hand panels of Fig. 2). Note that in Fig. 3, the count sums are divided by the maximum amplitude of the peaks in each panel.

2.3 Seeing

The blue-grism FORS1 observation corresponds to a Julian Date (JD) of 245 2529.65. The values of the seeing during this observation were 1.14 arcsec at the beginning and 1.25 arcsec at the end of the run, i.e. smaller than 4 arcsec, which is the distance from slit C to HD 5980. Thus, in principle, there should be no significant contamination from the stars in HD 5980 at the position of slit C.

3 MASSIVE STAR SPECTRA

D19 obtained stellar parameters and rotational velocities from a large sample of massive star optical spectra obtained with the FLAMES and the Giraffe spectrograph on the VLT. Some of the stars in D19 are near or within the slits used in V19. P. Dufton kindly shared these spectra with us. By comparing the latter spectra with the blue-grism FORS1 observations, we can double check the accuracy of our VLT FORS1 slit-position determinations.

Table 2 provides the list of stars within FORS1 slits A, B and C for which we extract spectra. The table gives the stellar ID, spectral classification, coordinates, bottom-row pixel used in our spectral extraction, and reference for the spectral classification. The meanings of the O-star designations are given in table 1 of van der Hucht (1996). The table includes a region near multiple-star system HD 5980 and an O4 V [(f)] star, which are not included in D19. We show their spectra in this section for completeness.

3.1 Spectral extraction

We use a custom PYTHON routine to extract one-dimensional spectra from the two-dimensional FORS1 spectral images using boxes of 6 pixels in height. This height, which corresponds to the diameter of the VLT FLAMES-Medusa fibres, i.e. to 1.2 arcsec, projects to

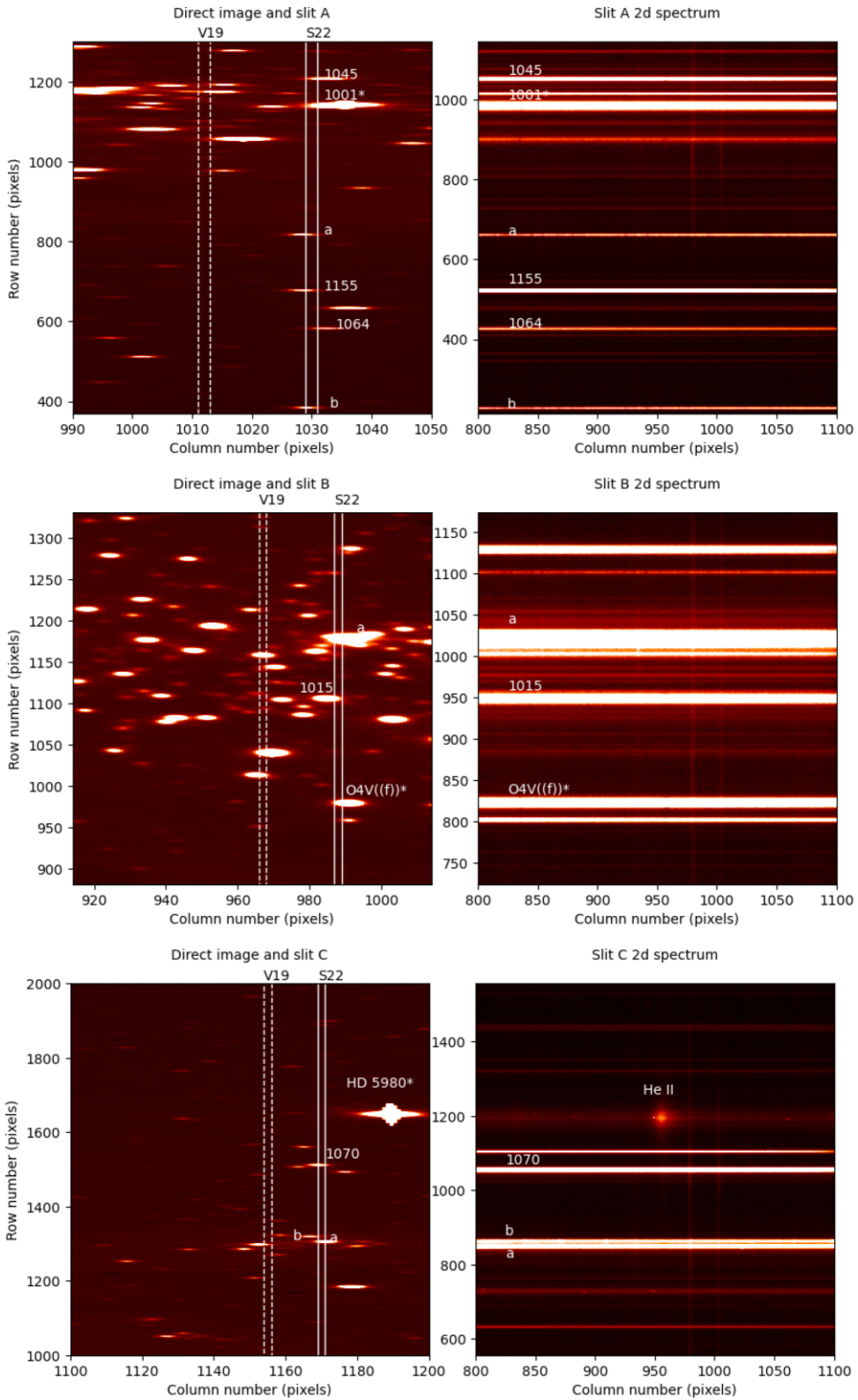


Figure 2. Left-hand panels: Portions of the direct images near slits A, B, and C from top to bottom. East is up and north is to the right. We overlay the footprints of the slits at positions V19 (dashed vertical lines) and S22 (solid vertical lines). The slit is ~ 0.51 arcsec, i.e. 2 pixel wide. Except for HD 5980 and O4 V[(f)], we use the D19 IDs of known massive stars to indicate their positions. For unclassified stars with spectral traces we use lower case letters. We add an asterisk if the known star is part of ULLYSES. Stars marked with lower case letters are unclassified and used for reference in Fig. 3. Right: Portions of the blue-grism 2D spectra showing that the S22 positions are more accurate than the V19 ones. Note the bright He II emission that is located south of HD 5980 (bottom-right panel). The direct and 2D images are stretched because the aspect ratio of the panels is one but the pixel ranges are different for the x and y axes. However, the number of rows is the same for the direct and 2D images. The number of rows shown for each slit varies in order to show relevant features.

Table 1. Coordinates of slit centres.

Slit	RA ^a V19	Dec. ^a V19	RA ^b S22	Dec. ^b S22	ΔDec. ^c (V19–S22)
A	00:59:06	−72:10:29.3	0:59:06	−72:10:25.75	3.5 arcsec
B	00:59:06	−72:10:37.3	0:59:06	−72:10:34.1	3.2 arcsec
C	00:59:19	−72:10:00.7	0:59:19	−72:09:57.8	2.9 arcsec

Notes. ^aJ2000 values from V19.

^bJ2000 values derived in this work.

^cDifference in declination of slit centre between V19 and S22.

0.35 pc at the distance of the SMC. In Appendix A, we show that our PYTHON extraction code yields spectra that are undistinguishable from those obtained with IRAF’s apall routine.

For the O4 V [(f)] star and the stars in D19, we subtract the background. This does not include HD 5980, in which case we are interested in the nebular contribution. The box for the background spectrum is 6 pixels in height and is located in the vicinity of the spectral trace, avoiding nearby stellar sources. We use python numpy.polyfit to fit a 10th-order polynomial to line-free portions of the sky-subtracted FORS1 spectra. We then normalize each extracted FORS1 spectrum by dividing the observed flux by the polynomial. We correct the spectra for the redshift, which we derive from the nebular [Ar IV] λ 4740 emission line of NGC 346 obtained for window #14 in Fig. 1. The redshift is $z = 0.000\,68$, corresponds to 204 ± 4 km s^{−1}, and is within values measured from interstellar medium components along the line of sight to the brightest stars, which go from ~ 130 to 210 km s^{−1} (see Koenigsberger, Peimbert, et al. 2001).

Fig. 4 shows the comparison between the normalized FLAMES and blue-grism FORS1 spectra. We show the FLAMES spectra at the original resolution (top blue curve) and with the same sampling as the FORS1 spectra (middle blue curve). The title of each panel gives the ID of the FORS1 slit, the star ID from D19, and the spectral and

luminosity class of the star from Table 2. In the figure, we mark the rest-frame wavelengths of the strongest lines that are listed in Table 3.

In Martins & Palacios (2017), the spectral type is determined from the ratio of the equivalent width of He I λ 4471 to He II λ 4542 for O4 to O9.7 stars. For O8.5 to B0 stars, the criteria from Sota et al. (2011), which include the ratio of the S III λ 4552 to He II λ 4542 line, are added. Fig. 4 shows that for stars of these types, the FORS1 spectra have sufficient spectral resolution and signal-to-noise ratio (SNR) to estimate the ratio of the equivalent width of He I λ 4471 to He II λ 4542. In particular, for the main-sequence stars (top three panels), note that the high-ionization optical He II absorption lines are absent in the B3 star and get stronger from O9 to O7 as the corresponding stars get hotter. On the other hand, the weak S III λ 4552 of the O9 V star is barely detected. In addition, in Martins & Palacios (2017), the luminosity class of O stars with spectral type earlier than O8.5 is obtained from the morphology of the He II λ 4686. In the case of the O4 If + O5-6 system, the quality of the FORS1 data is insufficient to appreciate the morphology of the weak line He II λ 4686. In Evans et al. (2004) and D19, a combination of the equivalent width of H γ , which is clearly detected, and the B-band magnitude is used for determining the luminosity class of early B stars. Finally, the O III 5592 line has been used to determine rotational velocities of Galactic O-type stars (e.g. Simón-Díaz & Herrero 2014). This line that is not covered by the FLAMES observations is covered by the FORS1 blue grism. However, at the low metallicity of the SMC, the line is too weak in the FORS1 data to be clearly detected. Note that the wavelength range that is shown in Fig. 4 does not include the latter line. The similarities between the FLAMES and FORS1 spectra give us confidence that our FORS1 slit position determinations are sufficiently accurate for our purposes.

For completeness, we extract blue-grism FORS1 spectra of two additional sources that appear in Figs 2 and 3, and are listed in Table 2, but are not in D19, i.e. an O4 V [(f)] star and a region in

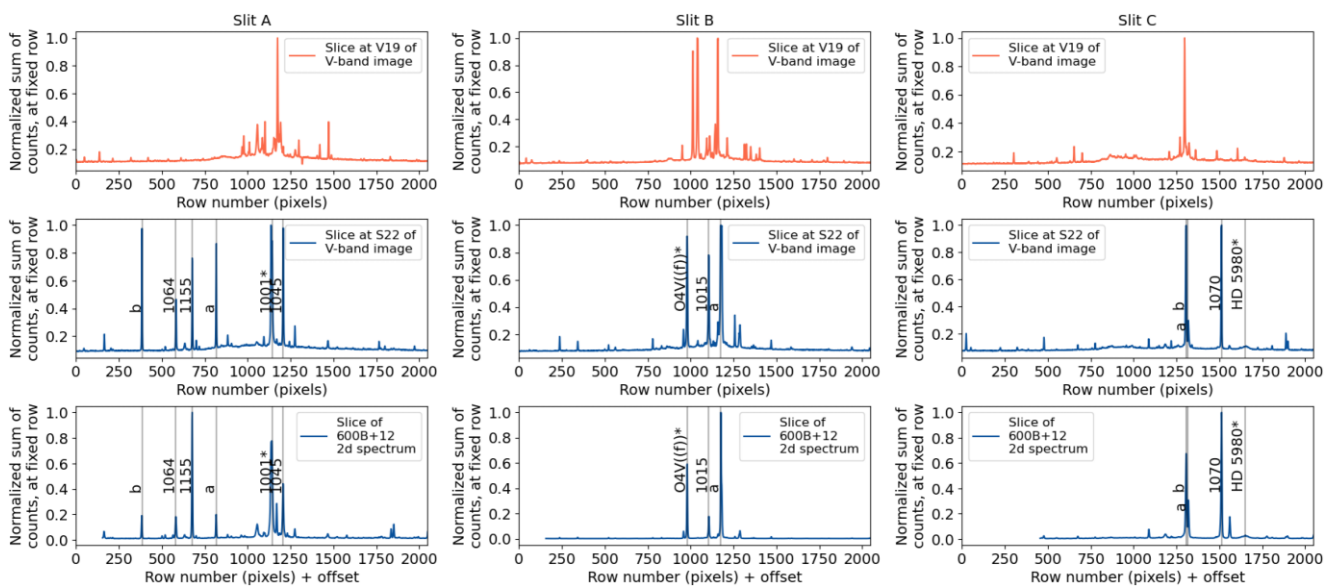


Figure 3. Top panels: For every row of the V-band image, sum of the counts in the columns that span the width of the slit, when the slit is located at the V19 position. The sums are divided by the largest sum. From left to right, we show results for slits A, B, and C. Middle panels: Similar to the top panel but now the slit is located at the S22 position. We label the peaks corresponding to stars that are labelled in Fig. 2. Bottom panels: For every row of the 600B + 12 2D spectrum, sum of the counts in columns 800 to 850. As can be seen in Fig. 2, these columns are free of emission lines. The sums are divided by the largest sum. We label the peaks corresponding to stars that are labelled in Fig. 2. Note that the peaks of the top and bottom panels are not aligned, contrary to the peaks of the middle and bottom panels. This is because the S22 positions are more accurate. Also note that the 2D spectrum covers bluer wavelengths than the V-band image. This affects the relative heights of the peaks in the middle and bottom panels.

Table 2. Massive stars and regions near them for which we extract VLT FORS1 spectra, grouped by luminosity class.

Slit ^a (1)	ID ^b (2)	Classification ^c (3)	RA ^d (4)	Dec. ^d (5)	y-pixel ^e (6)	Ref ^f (7)
A	1164	B3 V	0:58:40.140	-72:10:25.000	426	D19
A	1045	O9 V	0:59:07.330	-72:10:25.300	1051	D19
B	1015	O7 V	0:59:02.904	-72:10:34.569	935	D19
B	O4 VI(f)*	O4 VI(f)	0:58:57.419	-72:10:33.268	822	W00
A	1001*	O4 If + O5-6	0:59:04.499	-72:10:24.766	984	D19
A	1155	B1.5 III	0:58:44.280	-72:10:25.800	521	D19
C	1070	B2 III	0:59:20.600	-72:09:58.000	1056	D19
C	HD 5980*	WN5-6 + WN4 + OI	0:59:26.587	-72:09:53.948	1194	H19

Notes. ^aSlit where the star is located.

^bID of the star. The asterisk indicates that the star is a ULLYSES target. The names of the stars in ULLYSES are: NGC346-7 {O4V[(f)]} and NGC346 435 (1001). Note that 1001 is classified as an O4III(n)f in ULLYSES, <https://ullyses.stsci.edu/ullyses-targets-smc.html>.

^cClassification from the reference given in column (7).

^dStar coordinates from the reference given in column (7).

^eBottom row (pixel) of spectral extraction box.

^fReference for the stellar classification. D19: Dufton *et al.* (2019). W00: Walborn *et al.* (2000). H19: Hillier *et al.* (2019).

close proximity to HD 5980. Fig. 5 shows the result. For the spectrum corresponding to the vicinity of HD 5980, we do not subtract the background, as we are interested in any nebular emission near this source. The bottom panel of Fig. 5 and more detailed analysis of Section 4 show that no nebular He II emission is detected in the FORS1 observations. Note that in the bottom panel of Fig. 5, the narrow peaks marked with dotted-vertical lines are contaminating cosmic rays. In the latter panel, also note the detection of broad He II 4686 and NIV 4058 emission, which are characteristic of WN5-6 SMC stars (see fig. 3 of Crowther & Hadfield 2006). The N III 4634–41 emission feature is very weak.

3.2 Red-grism spectra

Given that our main goal is the study of nebular He II emission in SF galaxies, our main interest is in the blue-grism FORS1 spectra. However, we also have red-grism FORS1 data. One of the most useful applications of the FORS1 red-grism spectra would be the study of variability in the broad stellar H α emission line of systems 1001 and HD 5980. Unfortunately, in the case of 1001, the stellar component is in absorption and in the case of HD 5980, the strong nebular component makes it difficult to extract an accurate stellar component. Fig. 6 shows the spectra around H α of these two stars.

4 HE II EMISSION SOUTH OF HD 5980

The FORS1 slit C is located at a projected distance of ~ 1.2 pc south of HD 5980. As previously mentioned, the seeing during the observation with the blue grism is smaller than this distance. In order to study the He II $\lambda 4686$ emission south of HD 5980 (hereafter, He II emission), we extract slit-C spectra within windows of 0.51 arcsec \times 5 arcsec in size, which at the distance of the SMC corresponds to boxes of 0.15 pc \times 1.48 pc in size. The windows are shown in Fig. 1. We extract a spectrum from each window using a custom PYTHON routine. We do not subtract the nebular emission in order to check whether any contaminates the He II emission. For each window, we perform the following steps. (1) We match the fluxes of the FORS1 blue and red grisms by following the method that is described in Appendix B. Note that this step is mostly required for step 2 below and for plotting FORS1 observations that use both grisms in the diagnostic diagram of Section 5.3. (2) We transform from counts per pixel to flux units by multiplying the counts per

pixel by 2.36×10^{-15} erg s $^{-1}$ cm $^{-2}$ Å $^{-1}$. We obtained the latter factor by comparing flux-calibrated spectra from V19 with spectra that we extracted from the same regions. This is because the headers of the files containing the archival FORS1 2D spectra do not contain the information that is required to perform the flux calibration. (3) We correct for foreground extinction due to the Milky Way (MW) using $E(B - V) = 0.033$ mag (Schlafly & Finkbeiner 2011) and the MW extinction law of Fitzpatrick (1999). (4) We use the redshift measured from the nebular [Ar IV] $\lambda 4740$ emission line in window #14, i.e. $z = 0.000\,68$, to correct each extracted spectrum for the redshift. (5) We correct for reddening due to dust in NGC 346 by using $E(B - V) = 0.08$ mag (Hennekemper *et al.* 2008) and the SMC bar extinction law of Gordon *et al.* (2003).

4.1 Properties of the broad He II emission lines

For the extraction windows with an SNR ≥ 5 in the He II $\lambda 4686$ line and a clear broad ($\gtrsim 1000$ km s $^{-1}$) He II component, Fig. 7 shows the continuum-subtracted He II $\lambda 4686$ line profiles. The fit to the continuum is a first-order polynomial that uses the wavelength range 4686 ± 100 Å and avoids the strongest emission lines. The total distance covered by the 10 windows along the slit corresponds to ~ 15 pc. In Fig. 7, the FWHM and velocity shift of the He II line components are given in the legend of each panel. As expected, the strongest He II emission corresponds to window 22, which is the closest to HD 5980. Two broad He II components are required to reproduce the He II profiles of windows 20 to 26, while only one broad component is necessary for the rest of the windows. In particular, the He II profile corresponding to window 22 is composed of a redshifted component with FWHM ~ 1439 km s $^{-1}$ and a blueshifted component with FWHM ~ 603 km s $^{-1}$.

4.2 Orbital phase during the FORS1 blue-grism observation

In order to interpret the shape of the He II profile corresponding to window 22, we start by comparing the orbital phases corresponding to (i) the eclipse between the two WN stars and (ii) the date of the FORS1 blue-grism observation. The orbital period of the WR stars is 19.265 d and the date of the eclipse is JD2443158.77 (Koenigsberger *et al.* 2010). The latter eclipse corresponds to an orbital phase of $\phi = 0.36$ and to Star B in front of Star A, by definition of Star B. On the other hand, the date of the FORS1 observation is JD2452528, which

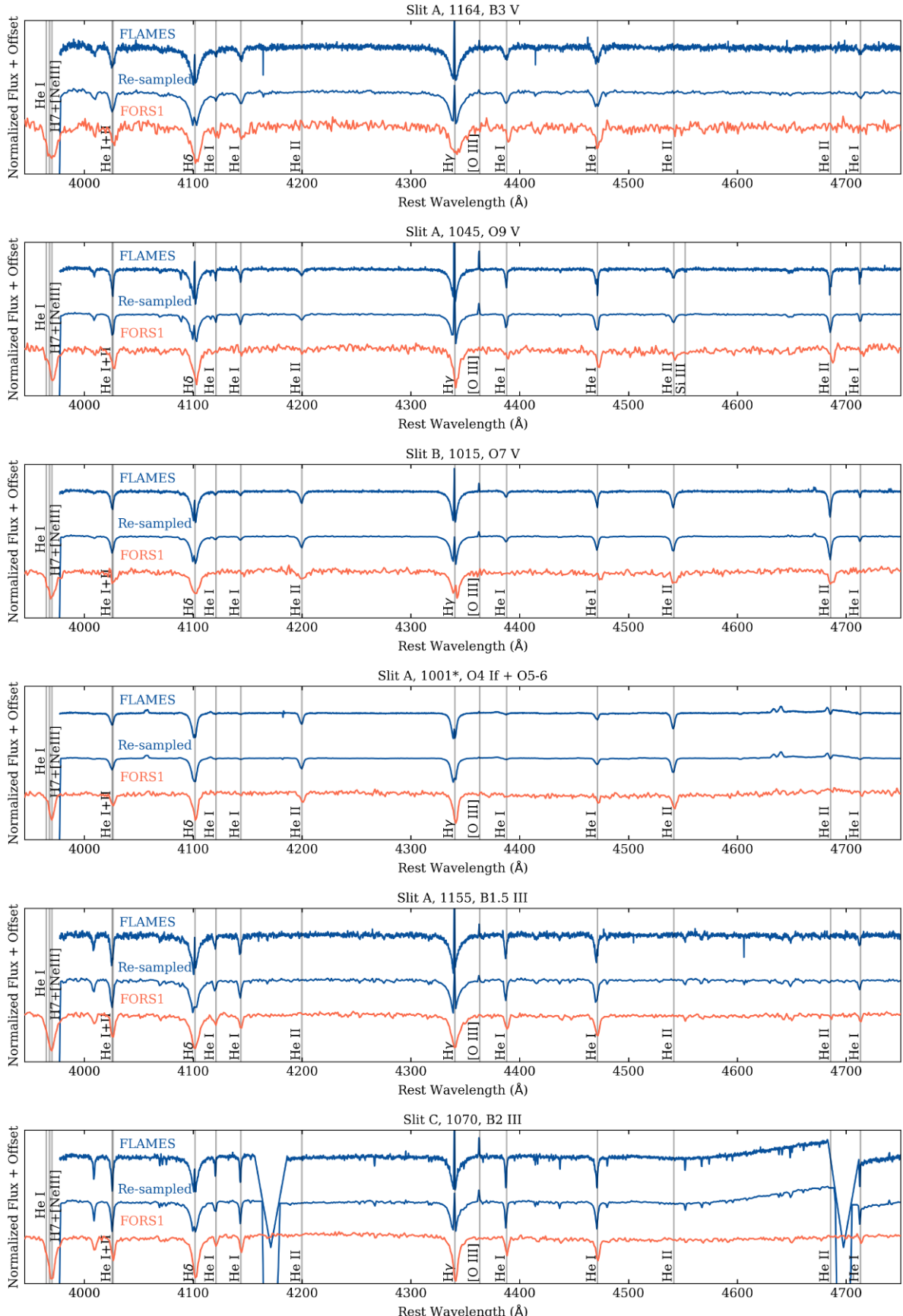


Figure 4. Normalized spectra from FLAMES's 1.2 arcsec fibres (top blue curves) and FORS1's 0.5 arcsec \times 1.2 arcsec windows (bottom red curves). We also show the FLAMES spectra re-sampled to match the FORS1 spectra (middle blue curves). We mark the rest-frame wavelengths of spectral lines listed in Table 3. In the bottom panel, the two gaps in the FLAMES spectra are due to hot pixels in the array that were removed to enable normalization.

Table 3. Line list corresponding to Fig. 4. The rest-frame wavelengths are in air.

Ion	λ_{air}
He I	3964.73
[Ne III]	3967.79
H γ	3970.07
He II	4025.60
He I	4026.18
H δ	4101.73
He I	4120.81
He I	4143.76
He I	4168.97
He II	4199.83
He I	4387.93
H γ	4340.46
[O III]	4363.21
He I	4471.47
He II	4541.59
Si III	4552.62
He II	4685.71
He I	4713.16

corresponds to $\phi = 0.32$, i.e. very close to the phase of the eclipse. Hillier *et al.* (2019) showed that at $\phi = 0.36$, a significant amount of line emission originating in Star A is observed. This is because the wind line-emitting region has a significantly larger radius than the eclipsing disc of Star B. Therefore, even if Star B had no wind, we would still see a WR emission-line spectrum at $\phi = 0.36$ due to Star A. Not only is the date of the FORS1 observation close to the eclipse but the shape of the He II profile observed with FORS1 is qualitatively very similar to an independent STIS optical observation at $\phi = 0.36$. In the next section, we describe the *HST*/STIS observation and compare the two profiles quantitatively.

4.3 Comparison with STIS observation of HD 5980

The He II $\lambda 4686$ emission of the multiple-star system HD 5980 was observed with *HST*/STIS and the $52 \text{ arcsec} \times 0.2 \text{ arcsec}$ slit, as part of programme 14476 (PI: Nazé, ID: 14476; Hillier *et al.* 2019). The

observation, which was centred on HD 5980 (unlike the FORS1 observation, which observed further south), was obtained on 2016 September 21 (JD = 245 7653.06), and corresponds to the orbital phase of the eclipse ($\phi = 0.36$; Koenigsberger *et al.* 2010). Fig. 8 shows the He II $\lambda 4686$ emission-line profiles corresponding to the FORS1/slit C/window 22 and STIS observations. The figure shows that both profiles have a very similar morphology. By fitting two Gaussians to the STIS He II observation, we find a similar result than for FORS1; i.e. the best fit has a broad component with FWHM $\sim 1700 \text{ km s}^{-1}$ that is redshifted by 527 km s^{-1} and a narrower component with FWHM $\sim 900 \text{ km s}^{-1}$ that is blueshifted by -84 km s^{-1} .

The above result can be interpreted in two ways: (i) either the seeing of the FORS1 observation is larger than the value quoted previously and with FORS1 we are looking at light coming directly from HD 5980; or (ii) with FORS1 we are catching light that is being reflected by material inside or outside of slit C. We note that we are confident in the position that we determined for slit C. This is based on results shown in the bottom panels of Figs 2 and 4, as well as in the last column of Fig. 3, where we show that the FORS1 and FLAMES spectra of star 1070 are very similar.

According to Shenar *et al.* (2016), the spectral types of the WN stars in HD 5980 are: WN6h (A) and WN6-7 (B). In Fig. 9, we show spectra extracted from windows 19 to 24 (see Fig. 1) that span from 4000 to 5000 Å. The curves corresponding to windows 21 and 22 show broad N IV $\lambda 4058$ and He II emission, which are characteristic of the WR stars in HD 5980. This further reinforces our conclusion that we are looking at direct or reflected light from HD 5980. Also notable are the He II Pickering bumps and the broad components underlying the H I nebular lines.

5 IS NEBULAR HE II EMISSION EXPECTED SOUTH OF HD 5980?

Given the massive star content of HD 5980, we discuss here whether nebular He II is expected around this multiple-star system.

5.1 Predictions from stellar evolution models

Fig. 10 shows synthetic flux distributions at a distance of 10 pc from the two WN stars (top two panels) and the O I star (bottom

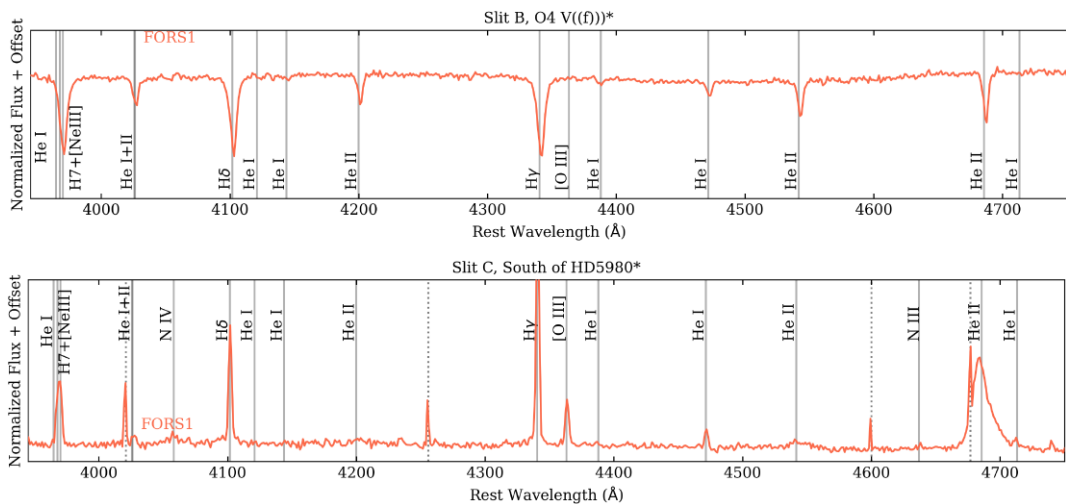


Figure 5. FORS1 spectra of two stars that are not in D19 but that are in ULLYSES. In the case of HD 5980, the narrow peaks marked with dotted-vertical lines are contaminating cosmic rays. Note that for HD 5980, no background subtraction was performed.

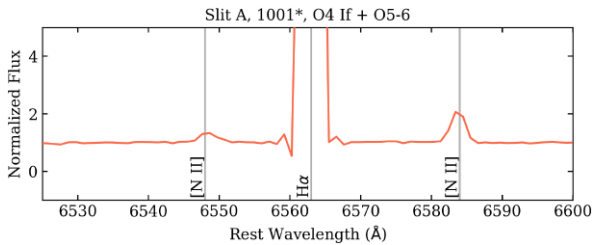


Figure 6. FORS1 red-grism spectra around $H\alpha$.

panel) in HD 5980. The distributions are based on Potsdam Wolf-Rayet Models (PoWR) atmosphere model calculations (Gräfener, Koesterke & Hamann 2002; Hamann & Gräfener 2003; Sander et al. 2015) implementing the obtained parameters from the spectral analysis by Shenar et al. (2016). In each panel, we give the effective temperature (T_{eff}) and luminosity (L/L_{\odot}) of the star, and its H I and He II ionizing rates. The figure shows that the O supergiant, despite quite some error margin due to the uncertainty in the mass-loss rate, is a far greater contributor to the He^+ ionizing budget of HD 5980 than the WN stars, by above three orders of magnitude. The origin of this striking difference is the much higher density in the WR winds, making them opaque to He^+ -ionizing photons for sufficiently high mass-loss rates (e.g. Schmutz, Leitherer & Gruenwald 1992).

Fig. 11 shows estimates for the He^+ ionizing rate ($Q_{\text{He II}}$) on the zero age main sequence (ZAMS) for the SMC. To estimate the values, we calculated models from the SMC PoWR model grid (Hainich et al. 2019), but assuming the Vink, de Koter & Lamers (2001) mass-loss rates instead of the fixed \dot{M} available in the online grid. The stellar parameters are based on the SMC tracks from Brott et al. (2011). To extend the resulting relations to higher masses, an additional model for a $100 M_{\odot}$ SMC ZAMS star was calculated adopting the values from corresponding BoOST SMC track (Szécsi et al. 2022). The blue lines in the figure are connecting models with the same effective temperature but different values of the surface gravity ($\log g$) and the luminosity ($\log L$), indicating that when going from dwarfs to supergiants, the luminosity increases, which usually increases the ionizing flux, although this trend can be reverted due to stronger mass-loss consuming these photons. The orange curve is generated by using the luminosity from the SMC ZAMS inferred from Brott et al. (2011) and then interpolating the blue data set. By adding the additional data point based on Szécsi et al. (2022), we extend the curve up to initial masses of $100 M_{\odot}$.

This essentially gives the estimates for $\log Q_{\text{He II}}$ as a function of L (and the initial mass). For a better reading, we indicate the values for particular initial masses with small black dots and orange labels. The absolute values of the orange curve are subject to \dot{M} . Here, we employed the rates of Vink et al. (2001), which are also applied in most population synthesis codes. Individual OB star analyses in the SMC often yield lower mass-loss rates (e.g. Bouret et al. 2003; Ramachandran et al. 2019; Rickard et al. 2022), while recent theoretical calculations yielded partially conflicting results (e.g. Björklund et al. 2021; Vink & Sander 2021). In case of a downward revision in mass-loss rates for the ZAMS stage, the resulting $Q_{\text{He II}}$ values could even be higher than those indicated by our orange curve in Fig. 11.

Finally, the figure shows the He^+ ionizing rates of the three components of HD 5980. Note that the diagnostics for the O-star mass-loss rate are limited, so this star will have a higher uncertainty.

Despite all uncertainties, we can safely conclude from Fig. 11 that any individual ZAMS star above $50 M_{\odot}$ or any individual O

supergiant hotter than ~ 45 kK would outshine the whole HD 5980 system. Rickard et al. (2022) recently provided $Q_{\text{He II}}$ values for O stars of the nearby NGC 346 cluster. Among them, only three provide a He II-ionizing flux of more than 10^{43} s^{-1} and only one target – the O2 giant SSN 9 – has the capability to outshine Star C of HD 5980 with a flux of $10^{46.5} \text{ s}^{-1}$. However, this star is in the middle of the cluster and far away from our studied region.

5.2 Predictions from population synthesis models

For SSPs composed of single, non-rotating stars, and without VMSs (maximum stellar mass is $100 M_{\odot}$), Fig. 12 shows the predicted evolution of $Q_{\text{He II}}$ and the numbers of O, WN, and WC stars. The latter numbers are scaled down by the factors given in the legends so that all curves can be shown near to each other. The predictions are from two independent codes: STARBURST99 (top panel) and Charlot & Bruzual 2019 (CB19, Plat et al. 2019; bottom panel).

The predictions for $Q_{\text{He II}}$ significantly depend on the implemented evolutionary tracks, their incorporated mass-loss descriptions, and the model atmospheres mapping the derived population. STARBURST99 employs GENEC (Ekström et al. 2012) evolutionary tracks with $Z_{\odot} = 0.014$ as those for $Z = 0.008$ tracks are not yet implemented. The assigned model atmospheres, however, take the subsolar metallicity of the LMC into account and use $0.4 Z_{\odot}$. The resulting output is generated as follows: (i) the mass-loss rates are those inherent to the GENEC tracks for solar metallicity; (ii) the star numbers are for solar-metallicity models (for O stars, these include both main-sequence and post-main-sequence stars); and (iii) the number of ionizing photons is calculated from solar-metallicity tracks and atmospheres with $0.4 Z_{\odot}$.

The visualizing in the top panel of Fig. 12 shows that during the first 3 Myr, the value of $Q_{\text{He II}}$ is completely determined by O-type stars (which is expected). Then, there is an increase in $Q_{\text{He II}}$ when the number of WCs is a maximum. This is in conflict with empirical studies of WC stars, which are not contributing significant amounts of $Q_{\text{He II}}$ due to their dense winds. However, it is a known problem in STARBURST99 that the photon output for the WC does not match the observations (C. Leitherer, private communication).

The CB19 synthesis models employ PARSEC stellar evolution tracks (Bressan et al. 2012) using $Z = 0.008$ and atmospheres of roughly matching metallicity (see Plat et al. 2019, for more details). The CB19 predictions (bottom panel of Fig. 12) show an increase in $Q_{\text{He II}}$ with the appearance of the WNLs. The WCs also contribute to this increase and at a later time the WNEs. Assuming a causality between the rising WR numbers and $Q_{\text{He II}}$, these results are confusing as well as one would not expect the usually strong-winded WNL and WC stars to be transparent to He II-ionizing photons. Both SB99 and CB99 use the PoWR atmosphere model grids (Todt et al. 2015). The mass-loss rate is one (indirect) parameter entering these

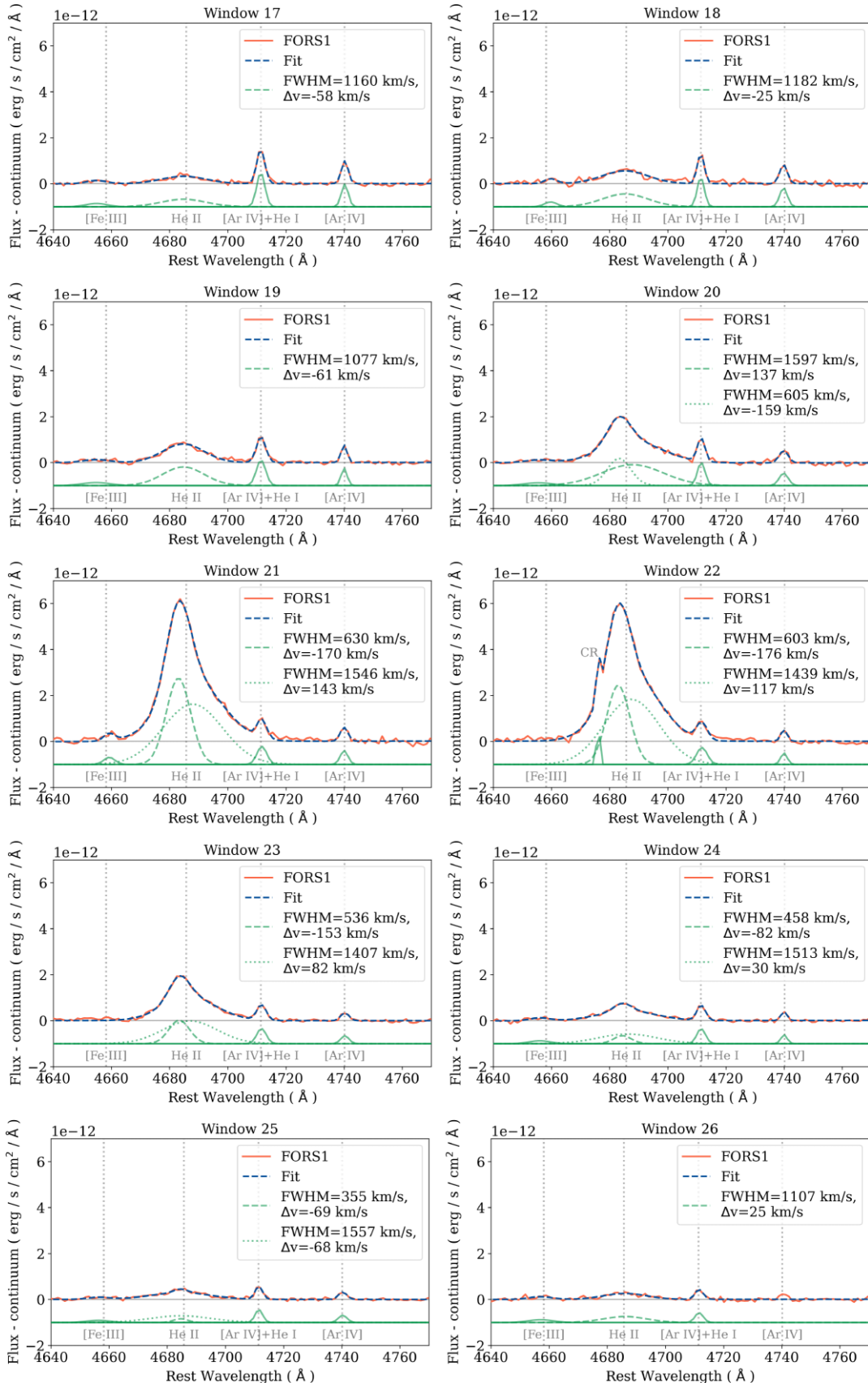


Figure 7. Continuum-subtracted spectra corresponding to 10 windows along slit C, with an SNR ≥ 5 in the He II $\lambda 4686$ line (red curves). The blue curve is a multi-Gaussian fit to the observations. The green curves below the observations show the individual Gaussian components (we use a dashed curve for He II). Nearby lines are labelled underneath the green curves. The legend gives the FWHM and velocity shift of the He II line components.

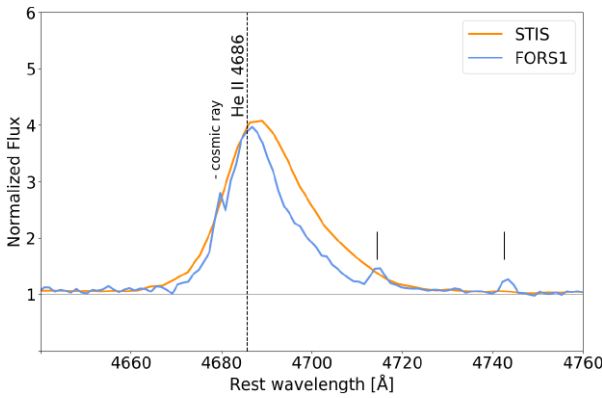


Figure 8. Orange curve: *HST* STIS observations (aperture 53 arcsec \times 0.2 arcsec, PI: Nazé, ID: 14476) of HD 5980, taken with the G430L filter on 2016 September 21 (JD = 245 7653.059 13) corresponding to the eclipse (0.36; Koenigsberger et al. 2010). Blue curve: FORS1 observations (see 2) corresponding to an orbital phase of 0.32. The black segments above the two emission lines mark the positions of the [Ar IV] + He I λ 4711 and [Ar IV] λ 4740 nebular lines in the blue spectrum, respectively.

grids, resulting in a set that can yield both atmospheres with and without significant He II-ionizing flux.

Previous authors have found that stellar population synthesis models predict more WR stars than are observed in some nearby galaxies. In their census for hot, luminous stars in the Tarantula region in the LMC, Doran et al. (2013) found only seven classical WR stars and five very massive WNh stars residing in the core of R136. The very massive WNh stars are located in a very young region (\sim 2 Myr) and will be gone by the time the cWR stars are predicted to appear by the stellar population models (\sim 3 Myr; see Fig. 12). The seven cWR stars observed in the wider Tarantula region (NGC 2070) are older and likely stem from the peak of star formation in this region, which was \sim 4 Myr ago according to Schneider et al. (2018). When comparing with BPASS population synthesis models, Bestenlehner et al. (2020) found that the number of observed cWR stars is actually lower than what was predicted. The super star cluster (SSC) A in dwarf galaxy NGC 1569 has a similar age (Hunter et al. 2000) and metallicity (Kobulnicky & Skillman 1997) than the wider Tarantula region in the LMC (Mayya et al. 2020). Using Gran Telescopio

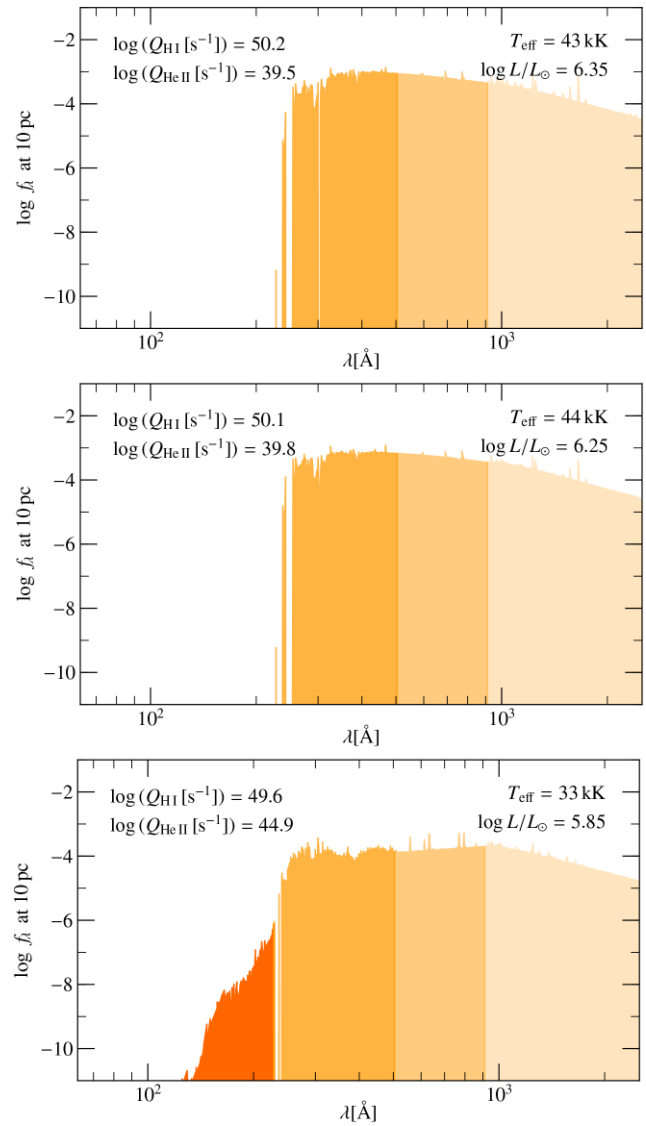


Figure 10. Synthetic flux distributions at a distance of 10 pc from the two WN stars (top two panels) and the O supergiant (bottom panel) in HD 5980.

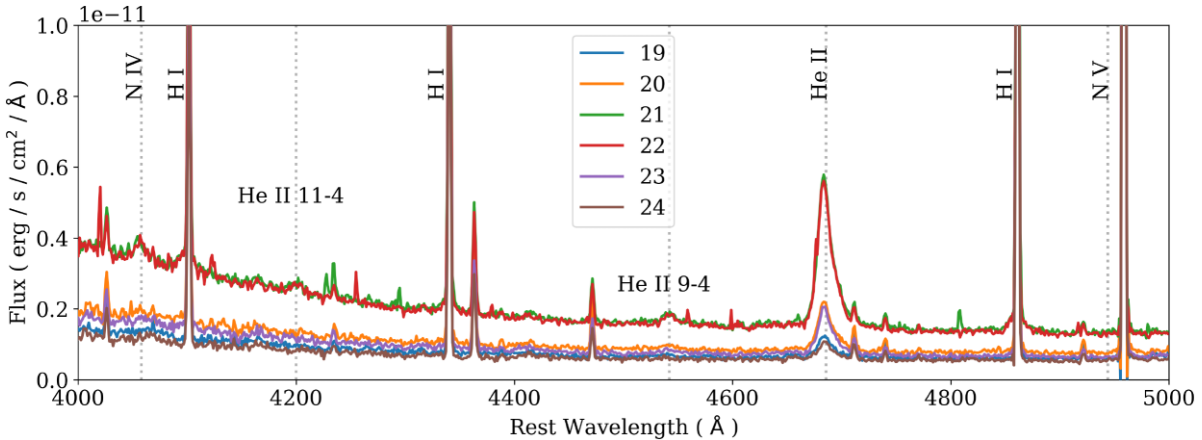


Figure 9. Spectra extracted from windows 19 to 24. The windows are 0.51 arcsec \times 5 arcsec in size and their location along slit C is shown in Fig. 1. The spectra are uncorrected for reddening due to dust but corrected for redshift. The legend gives the window number. We mark with vertical dotted lines the positions of the broad N IV λ 4058 and He II λ 4686 emission lines and the He II 11–4 (4200 Å) and He II 9–4 (4542 Å) Pickering bumps. Note the broad components underlying the nebular hydrogen lines.

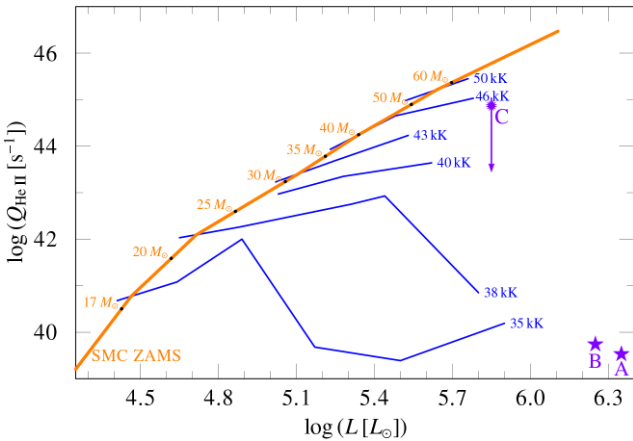


Figure 11. Estimates for the He^+ ionizing rate ($Q_{\text{He II}}$) on the ZAMS. The blue lines connect models with the same T_{eff} but different values of $\log g$ and $\log L$. The orange curve is generated by using the luminosity from the SMC ZAMS in Brott et al. (2011) and then interpolating the blue data set (see the text for more details). The positions of the stars in HD 5980 are indicated with the letters A, B, and C. We use different symbols for the two WNs and the O star.

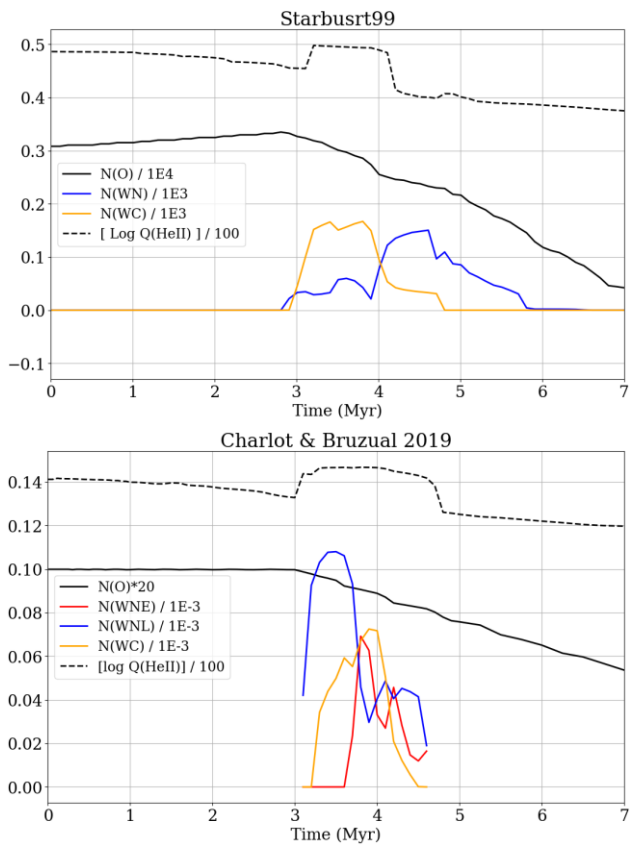


Figure 12. Predicted evolution of $Q_{\text{He II}}$ and the numbers of O, WN, and WC stars for SSPs without VMSs and composed of single, non-rotating stars. The latter numbers are scaled down by the factors given in the legends so that all curves can be shown near to each other. We show predictions from two independent codes: STARBURST99 (top panel, $10^6 M_\odot$ SSP) and Charlot & Bruzual 2019 (bottom panel, SSP with stellar initial mass function normalized to $1 M_\odot$). The metallicity of the stellar atmospheres approaches that of the SMC (see the text for more details).

Canarias MEGARA observations of SSA A, Mayya et al. (2020) estimate the number of WR stars from the ratio of the observed integrated luminosity of the broad $\text{He II} \lambda 4686$ line to the typical luminosity of a WNL star ($\sim 1.22 \times 10^{36}$ erg s $^{-1}$ for the metallicity of the galaxy). Mayya et al. (2020) find 124 ± 11 WNL stars, which is consistent with the STARBURST99 predictions shown in their fig. 9 (first column, middle panel) but too much compared to what has been observed in NGC 2070, even though being of similar mass. The estimates from line luminosities are very rough and the attribution to specifically WNL stars is somewhat arbitrary. Moreover, WNL stars are not expected to yield measurable amounts of He^+ -ionizing flux (Crowther & Hadfield 2006; Sander 2022), which is at odds with the strong flux measured by Mayya et al. (2020), as there, similar to what we find here, the population models seem to predict ionizing fluxes from the WNL stage.

Given the findings in the Tarantula region and the uncertainties of the measurement by Mayya et al. (2020), it appears that the numbers of WR stars are actually overpredicted by stellar population synthesis models. However, the WR classification is formally a purely spectroscopic one, while the assignment from the population models is usually based on surface composition and temperature. Hence, the predicted stars might not actually appear as WR stars, making them much harder to detect. The suspicious coincidence between the increase of the He^+ -ionizing flux and the number of cWR stars in fact indicates that the population synthesis models like to select weaker winded atmosphere models that have more transparent winds with few or no emission-line signatures. In the SSC A region of NGC 1569, this could potentially resolve the discrepancy, but the absence of He^+ -ionizing flux in the Tarantula region makes such an explanation invalid there. Assuming that the too low number of WR stars is an effect of overestimating the self-stripping of massive star (in single star evolution), one would expect to see more Red supergiants (RSGs) instead in the Tarantula region. As evident from the compilation by Bestenlehner et al. (2020), this does not seem to be the case. Finally, the lifetimes of WRs could be shorter than those assumed in the models, but given the relatively constant duration of the central He burning time in massive stars (~ 300 kyr) this would imply that the stars spend a considerable fraction of that in a stage where they do not become visible as cWRs. However, studying this is beyond the scope of this paper.

While a more detailed investigation would be necessary to precisely identify the origins of the mismatch between the empirical results and the population synthesis predictions, it seems likely that the currently implemented stellar evolution in both SB99 and CB99 yields significant populations of stars that do not have mass-loss rates that are high enough to be opaque to He II -ionizing photons. Instead, the predicted stars are sufficiently hot and hydrogen depleted to formally fall into the range where the WR grids are applied. Whether such stars would actually be classified as WR from their spectral appearance (Shenar et al. 2020) cannot be determined in the scope of this paper. None the less, we can conclude that the current generation of population synthesis models seems to have significant problems to get a realistic prediction of $Q_{\text{He II}}$, at least at subsolar metallicities. Updating $Q_{\text{He II}}$ predictions in widely used population synthesis codes using observations like the ones presented in this work will be crucial to enable a more realistic interpretation of SF galaxies.

5.3 What is the effect of the SNR south of HD 5980?

As mentioned in the introduction, Garnett et al. (1991) suggest that fast radiative shocks due to supernova explosions can produce

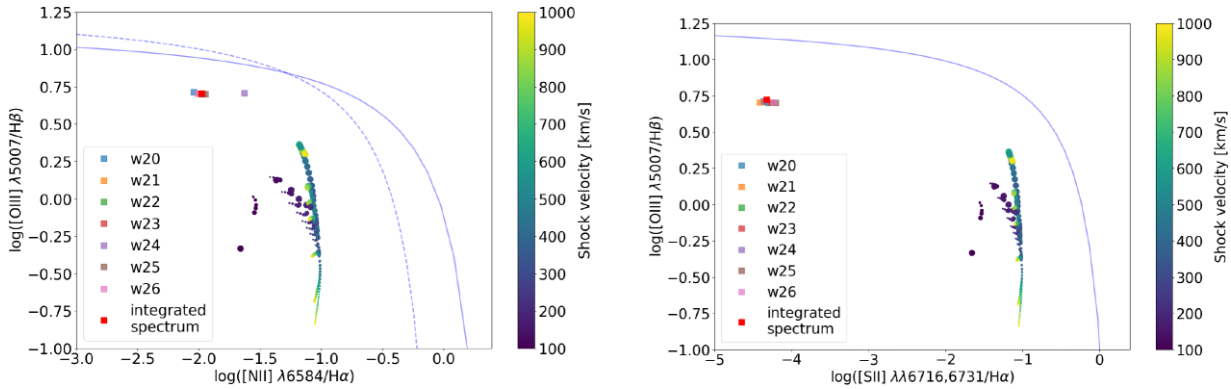


Figure 13. Left: $[\text{O III}] \lambda 5007/\text{H} \beta$ versus $[\text{N II}] \lambda 6584/\text{H} \alpha$ diagnostic diagram (Baldwin et al. 1981). The dashed and solid blue lines represent the Kauffmann et al. (2003) and Kewley et al. (2001) curves for separating SF objects from AGNs, respectively. Right: $[\text{O III}] \lambda 5007/\text{H} \beta$ versus $[\text{S II}] \lambda\lambda 6717, 6731/\text{H} \alpha$ diagnostic diagram (Veilleux & Osterbrock 1987). The solid blue line is the Kewley et al. (2001) curve for separating SF objects from AGNs. In both panels, the squares represent values measured in windows of slit C with two Gaussian components (Fig. 7) and $\text{SNR} \geq 5$ in the $\text{He II} \lambda 4686$ line (Fig. 1), and the red-filled square is the value measured after integrating the spectra of the seven windows. We also show the shock models of Alarie & Morisset (2019) with SMC metallicity, a pre-shock density of $n_0 = 1 \text{ cm}^{-3}$, shock speeds between 200 and 1000 km s^{-1} (see colour bar), and magnetic field strengths between 0.0001 and 10 μG (given by the size of the filled circle, where the size increases with the strength).

relatively strong He II emission in giant H II regions under certain conditions. The extended X-ray emission around HD 5980 coincides with non-thermal radio emission, suggesting that an SNR is present in the region (Reid et al. 2006). In Fig. 1, we indicate the position of SNR B0057–724, which is reported in Reid et al. (2006). The diffuse X-ray emission of the SNR reaches the region covered by our slit C (see fig. 10 of Reid et al. 2006). Thus, we looked at the positions of the observations corresponding to slit C and windows 20–26 (which have broad He II) in optical diagnostic diagrams relative to the radiative shock models of Alarie & Morisset (2019). These shock models agree with predictions presented in Allen et al. (2008) at SMC metallicity but include models of lower metallicities. Fig. 13 shows the diagnostic diagrams of Baldwin, Phillips & Terlevich (1981) and Veilleux & Osterbrock (1987), left- and right-hand panels, respectively. These diagrams use nebular emission-line fluxes corrected for the stellar component. The red square is the integrated value of the seven windows. For comparison, the filled circles show the SMC shock models, presented in Alarie & Morisset (2019). The colour bar corresponds to the shock speed, taking into account values between 100 and 1000 km s^{-1} . We find that the optical-line ratios of the spectra extracted from the windows are located far from the shock-model predictions. Thus, no evidence of the presence of the SNR is seen in these diagnostic diagrams. A caveat to this result is that the shock models do not account for any chemical enrichment from the products of the star that exploded.

The SNR is almost centred on HD 5980 and has dimensions ~ 4 arcmin according to Ye, Turtle & Kennicutt (1991) (see his fig. 6). The X-ray emission extends south to at least 1 arcmin. See fig. 1 of Nazé et al. (2002). Our slit is located 4 arcsec from HD 5980; hence, any light from the SNR should enter the slit. Velázquez, Koenigsberger & Raga (2003) proposed that the observed X-rays could result from the collision of HD 5980’s wind with the foreground SNR. If that were the case, then: (a) there would be significant collisional excitation and ionization; and (b) the SNR would be He enriched. Thus, one could argue that there should be nebular He II emission at the position of slit C. In order to verify that we have the ability to detect nebular emission within our broad He II emission, we simulate the presence of nebular He II emission by adding the flux of the nearby, nebular $[\text{Ar IV}] \lambda 4740 \text{ \AA}$ to the flux of the $\text{He II} \lambda 4686 \text{ \AA}$ line. Hereafter, we refer to the resulting profile as the combined

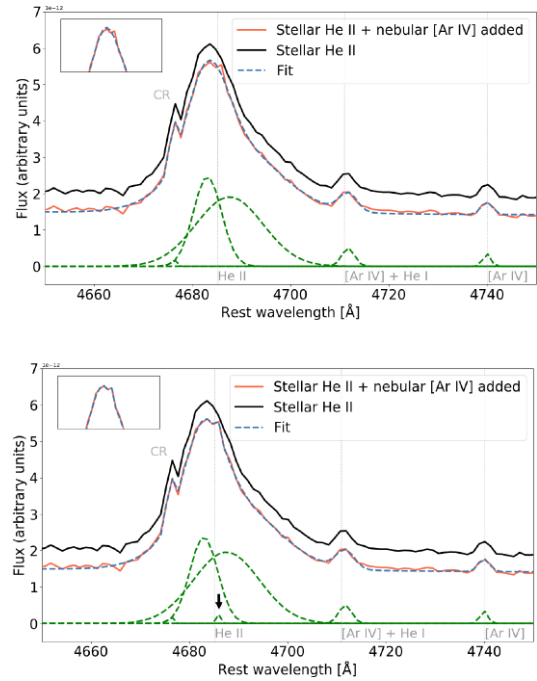


Figure 14. Simulation of stellar plus nebular He II profile (red curves in both panels). For simulating a nebular component, we add to the observed He II profile the $[\text{Ar IV}] \lambda 4740 \text{ \AA}$ line at 4686 \AA (see the text for more details). Two different fits to the result are presented (blue-dashed curves) corresponding to the Gaussian components shown with green-dashed curves. The black curve is the FORS1 observation, which is plotted offset for clarity. The insets in both panels show the peak of the combined emission ($\text{He II} + [\text{Ar IV}]$) and that the fit in the bottom panel is the best.

profile. We chose this $[\text{Ar IV}]$ line based on fig. 1 of López-Sánchez & Esteban (2010), where the nebular He II lines have fluxes that are similar to those of the $[\text{Ar IV}]$ line. We fit the combined He II profile, finding that a third emission component is now necessary in order to achieve a good fit. This is shown in the insets of Fig. 14, where the top inset corresponds to the fit without the third component and the bottom panel to the fit with it. We conclude that we have the ability to

detect nebular He II emission with the strength of the [Ar IV] λ 4740 Å line. However, we do not observe such emission.

6 SUMMARY AND CONCLUSIONS

We use archival long-slit observations obtained with FORS1 on the VLT to look for nebular He II λ 4686 emission south of the WN6-7 + WN6h close binary in HD 5980. We only find broad He II λ 4686 emission, as far as \sim 7.6 pc from the binary. A comparison with observations obtained with STIS on the *HST*, at a similar orbital phase, shows that the FORS1 broad He II emission is likely contamination from multiple-star system HD 5980. We use models to show that no significant He⁺-ionizing flux is expected from the WN stars in HD 5980 and that when similar stars are present in a coeval stellar population, the O stars are far greater emitters of He⁺-ionizing radiation.

We also compared the spectra of known massive stars within the FORS1 slits with published VLT FLAMES spectra of higher quality. This comparison gives us confidence in the revised FORS1 slit positions relative to V19, which we provide in this paper. The FORS1 red-grism observations of these stars did not add anything new to what is already known about them.

With regard to the SNR B0057–724 near HD 5980, we find that it is unlikely that it significantly contributes to nebular He II emission at the position of FORS1 slit C. We detect none at the level of the flux of the nearby [Ar IV] λ 4740 Å.

ACKNOWLEDGEMENTS

We thank the referee for comments that really helped improve the quality of this paper. AW and AS acknowledge the support of UNAM via grant agreement PAPIIT nos. IA102120 and IN106922. AACs is funded by the Deutsche Forschungsgemeinschaft (DFG; German Research Foundation) in the form of an Emmy Noether Research Group – Project-ID 445674056 (SA4064/1-1, PI: Sander) and acknowledges additional support from a DFG collaborative research centre – Project-ID 138713538 – SFB 881 ('The Milky Way System', subproject P04). We thank Gloria Koenigsberger, John Hillier, and Yael Nazé for useful discussions that led to the current interpretation of the FORS1 He II profile south of HD 5980; Philip Dufton, Danny Lennon, and Chris Evans for useful discussions about the known massive star content in the region covered with FORS1, and for providing the normalized VLT FLAMES spectra of the stars in common with this work; Claus Leitherer, Gustavo Bruzual, and Stéphane Charlot for their help with the output of their population synthesis models; Jay Gallagher, Lidia Oskinova, and Matthew Rickard for helping establish that the available *HST* STIS and VLT MUSE observations of NGC 346 do not include the region around HD 5980; and finally, Artemio Herrero, Miriam García, and Norberto Castro for very helpful information that enriched the discussion of Figs 4 and 5.

DATA AVAILABILITY

The data underlying this article will be shared on reasonable request to the corresponding author.

REFERENCES

- Adamo A. et al., 2017, *ApJ*, 841, 131
 Alarie A., Morisset C., 2019, *Rev. Mex. Astron. Astrofis.*, 55, 377
- Allen M. G., Groves B. A., Dopita M. A., Sutherland R. S., Kewley L. J., 2008, *ApJS*, 178, 20
 Asplund M., Grevesse N., Sauval A. J., Scott P., 2009, *ARA&A*, 47, 481
 Baldwin J. A., Phillips M. M., Terlevich R., 1981, *PASP*, 93, 5
 Bestenlehner J. M. et al., 2020, *MNRAS*, 499, 1918
 Björklund R., Sundqvist J. O., Puls J., Najarro F., 2021, *A&A*, 648, A36
 Bouret J. C., Lanz T., Hillier D. J., Heap S. R., Hubeny I., Lennon D. J., Smith L. J., Evans C. J., 2003, *ApJ*, 595, 1182
 Bouret J. C., Lanz T., Martins F., Marcolino W. L. F., Hillier D. J., Depagne E., Hubeny I., 2013, *A&A*, 555, A1
 Brands S. A. et al., 2022, *A&A*, 663, A36
 Bressan A., Marigo P., Girardi L., Salasnich B., Dal Cero C., Rubele S., Nanni A., 2012, *MNRAS*, 427, 127
 Brott I. et al., 2011, *A&A*, 530, A115
 Crowther P. A. et al., 2016, *MNRAS*, 458, 624
 Crowther P. A., 2007, *ARA&A*, 45, 177
 Crowther P. A., Hadfield L. J., 2006, *A&A*, 449, 711
 Doran E. I. et al., 2013, *A&A*, 558, A134
 Dufton P. L., Evans C. J., Hunter I., Lennon D. J., Schneider F. R. N., 2019, *A&A*, 626, A50
 Ekström S. et al., 2012, *A&A*, 537, A146
 Eldridge J. J., Stanway E. R., Xiao L., McClelland L. A. S., Taylor G., Ng M., Greis S. M. L., Bray J. C., 2017, *Publ. Astron. Soc. Aust.*, 34, e058
 Evans C. J., Howarth I. D., Irwin M. J., Burnley A. W., Harries T. J., 2004, *MNRAS*, 353, 601
 Fitzpatrick E. L., 1999, *PASP*, 111, 63
 Garnett D. R., Kennicutt R. C. J., Chu Y.-H., Skillman E. D., 1991, *ApJ*, 373, 458
 Gordon K. D., Clayton G. C., Misselt K. A., Landolt A. U., Wolff M. J., 2003, *ApJ*, 594, 279
 Götzberg Y., de Mink S. E., Groh J. H., Leitherer C., Norman C., 2019, *A&A*, 629, A134
 Gouliermis D. A., Hony S., 2015, Proc. IAU Symp. Vol. 316, Formation, Evolution, and Survival of Massive Star Clusters. Cambridge Univ. Press, Cambridge, p. 117
 Gräfener G., Koesterke L., Hamann W. R., 2002, *A&A*, 387, 244
 Guseva N. G., Izotov Y. I., Thuan T. X., 2000, *ApJ*, 531, 776
 Gutkin J., Charlot S., Bruzual G., 2016, *MNRAS*, 462, 1757
 Hainich R., Ramachandran V., Shenar T., Sander A. A. C., Todt H., Gruner D., Oskinova L. M., Hamann W. R., 2019, *A&A*, 621, A85
 Hamann W. R., Gräfener G., 2003, *A&A*, 410, 993
 Henize K. G., 1956, *ApJS*, 2, 315
 Hennekemper E., Gouliermis D. A., Henning T., Brandner W., Dolphin A. E., 2008, *ApJ*, 672, 914
 Hilditch R. W., Howarth I. D., Harries T. J., 2005, *MNRAS*, 357, 304
 Hillier D. J., Koenigsberger G., Nazé Y., Morrell N., Barbá R. H., Gamen R., 2019, *MNRAS*, 486, 725
 Hillier D. J., Lanz T., 2001, in Ferland G., Savin D. W., eds, ASP Conf. Ser. Vol. 247, Spectroscopic Challenges of Photoionized Plasmas. Astron. Soc. Pac., San Francisco, p. 343
 Hunter D. A., O'Connell R. W., Gallagher J. S., Smecker-Hane T. A., 2000, *AJ*, 120, 2383
 Izotov Y. I., Schaerer D., Blecha A., Royer F., Guseva N. G., North P., 2006, *A&A*, 459, 71
 James B. L. et al., 2022, *ApJS*, 262, 37
 Kauffmann G. et al., 2003, *MNRAS*, 346, 1055
 Kehrig C. et al., 2016, *MNRAS*, 459, 2992
 Kehrig C., Guerrero M. A., Vílchez J. M., Ramos-Larios G., 2021, *ApJ*, 908, L54
 Kehrig C., Vílchez J. M., Guerrero M. A., Iglesias-Páramo J., Hunt L. K., Duarte-Puertas S., Ramos-Larios G., 2018, *MNRAS*, 480, 1081
 Kehrig C., Vílchez J. M., Pérez-Montero E., Iglesias-Páramo J., Brinchmann J., Kunth D., Durret F., Bayo F. M., 2015, *ApJ*, 801, L28
 Kewley L. J., Dopita M. A., Sutherland R. S., Heisler C. A., Trevena J., 2001, *ApJ*, 556, 121
 Kobulnicky H. A., Skillman E. D., 1997, *ApJ*, 489, 636
 Koenigsberger G., Georgiev L., Hillier D. J., Morrell N., Barbá R., Gamen R., 2010, *AJ*, 139, 2600

- Koenigsberger G., Morrell N., Hillier D. J., Gamen R., Schneider F. R. N., González-Jiménez N., Langer N., Barbá R., 2014, *AJ*, 148, 62
- López-Sánchez Á. R., Esteban C., 2010, *A&A*, 516, A104
- Martins F., Palacios A., 2017, *A&A*, 598, A56
- Mayya Y. D. et al., 2020, *MNRAS*, 498, 1496
- Nazé Y., Hartwell J. M., Stevens I. R., Corcoran M. F., Chu Y. H., Koenigsberger G., Moffat A. F. J., Niemela V. S., 2002, *ApJ*, 580, 225
- Plat A., Charlot S., Bruzual G., Feltre A., Vidal-García A., Morisset C., Chevallard J., Todt H., 2019, *MNRAS*, 490, 978
- Portegies Zwart S. F., McMillan S. L. W., Gieles M., 2010, *ARA&A*, 48, 431
- Ramachandran V. et al., 2019, *A&A*, 625, A104
- Reid W. A., Payne J. L., Filipović M. D., Danforth C. W., Jones P. A., White G. L., Staveley-Smith L., 2006, *MNRAS*, 367, 1379
- Relaño M., Peimbert M., Beckman J., 2002, *ApJ*, 564, 704
- Rickard M. J. et al., 2022, *A&A*, 666, A189
- Roman-Duval J. et al., 2020, *Res. Notes Am. Astron. Soc.*, 4, 205
- Sabbi E. et al., 2007, *AJ*, 133, 44
- Sabbi E. et al., 2008, *AJ*, 135, 173
- Sander A. A. C., 2022, preprint ([arXiv:2211.05424](https://arxiv.org/abs/2211.05424))
- Sander A., Shenar T., Hainich R., Giménez-García A., Todt H., Hamann W. R., 2015, *A&A*, 577, A13
- Saxena A. et al., 2020, *A&A*, 636, A47
- Schaerer D., Contini T., Pindado M., 1999, *A&AS*, 136, 35
- Schaerer D., Vacca W. D., 1998, *ApJ*, 497, 618
- Schlafly E. F., Finkbeiner D. P., 2011, *ApJ*, 737, 103
- Schmutz W., Leitherer C., Gruenwald R., 1992, *PASP*, 104, 1164
- Schneider F. R. N. et al., 2018, *Science*, 359, 69
- Senchyna P. et al., 2017, *MNRAS*, 472, 2608
- Senchyna P., Stark D. P., Mirocha J., Reines A. E., Charlot S., Jones T., Mulchaej J. S., 2020, *MNRAS*, 494, 941
- Shenar T. et al., 2016, *A&A*, 591, A22
- Shenar T., Gilkis A., Vink J. S., Sana H., Sander A. A. C., 2020, *A&A*, 634, A79
- Shirazi M., Brinchmann J., 2012, *MNRAS*, 421, 1043
- Simón-Díaz S., Herrero A., 2014, *A&A*, 562, A135
- Smith L. J., Crowther P. A., Calzetti D., Sidoli F., 2016, *ApJ*, 823, 38
- Sobral D. et al., 2019, *MNRAS*, 482, 2422
- Sota A., Maíz Apellániz J., Walborn N. R., Alfaro E. J., Barbá R. H., Morrell N. I., Gamen R. C., Arias J. I., 2011, *ApJS*, 193, 24
- Stark D. P. et al., 2015, *MNRAS*, 454, 1393
- Szécsi D., Agrawal P., Wünsch R., Langer N., 2022, *A&A*, 658, A125
- Todt H., Sander A., Hainich R., Hamann W. R., Quade M., Shenar T., 2015, *A&A*, 579, A75
- Valerdi M., Peimbert M., Peimbert A., Sixtos A., 2019, *ApJ*, 876, 98
- van der Hucht K. A., 1996, in Vreux J. M., Detal A., Fraipont-Caro D., Gosset E., Rauw G., eds, Liege Int. Astrophys. Colloquia Vol. 33, Wolf-Rayet Stars in the Framework of Stellar Evolution. Liège Univ. Belgium., Belgium, p. 1
- Veilleux S., Osterbrock D. E., 1987, *ApJS*, 63, 295
- Velázquez P. F., Koenigsberger G., Raga A. C., 2003, in Reyes-Ruiz M., Vázquez-Semadeni E., eds, Proc. Conf. Ser. Vol. 18, The eighth Mexico-Texas Conference on Astrophysics : Energetics of Cosmic Plasmas. Astrophys., Rev. Mex. Astron., CDMX, Mexico, p. 150
- Vink J. S., de Koter A., Lamers H. J. G. L. M., 2001, *A&A*, 369, 574
- Vink J. S., Sander A. A. C., 2021, *MNRAS*, 504, 2051
- Walborn N. R., Lennon D. J., Heap S. R., Lindler D. J., Smith L. J., Evans C. J., Parker J. W., 2000, *PASP*, 112, 1243
- Wang L., Gies D. R., Peters G. J., Götzberg Y., Chojnowski S. D., Lester K. V., Howell S. B., 2021, *AJ*, 161, 248
- Wofford A., Leitherer C., Chandar R., 2011, *ApJ*, 727, 100
- Wofford A., Leitherer C., Chandar R., Bouret J.-C., 2014, *ApJ*, 781, 122
- Wofford A., Vidal-García A., Feltre A., Chevallard J., Charlot S., Stark D. P., Herenz E. C., Hayes M., 2021, *MNRAS*, 500, 2908
- Xiao L., Stanway E. R., Eldridge J. J., 2018, *MNRAS*, 477, 904
- Ye T., Turtle A. J., Kennicutt R. C. J., 1991, *MNRAS*, 249, 722

APPENDIX A: SPECTRAL EXTRACTION ROUTINE

In Fig. A1, we show spectra corresponding to slit C and window 22 of Fig. 1, which were extracted with our custom PYTHON routine (thick coloured curves) and IRAF’s apall routine (thin grey curves). Since the spectra are undistinguishable from each other, we can confidently

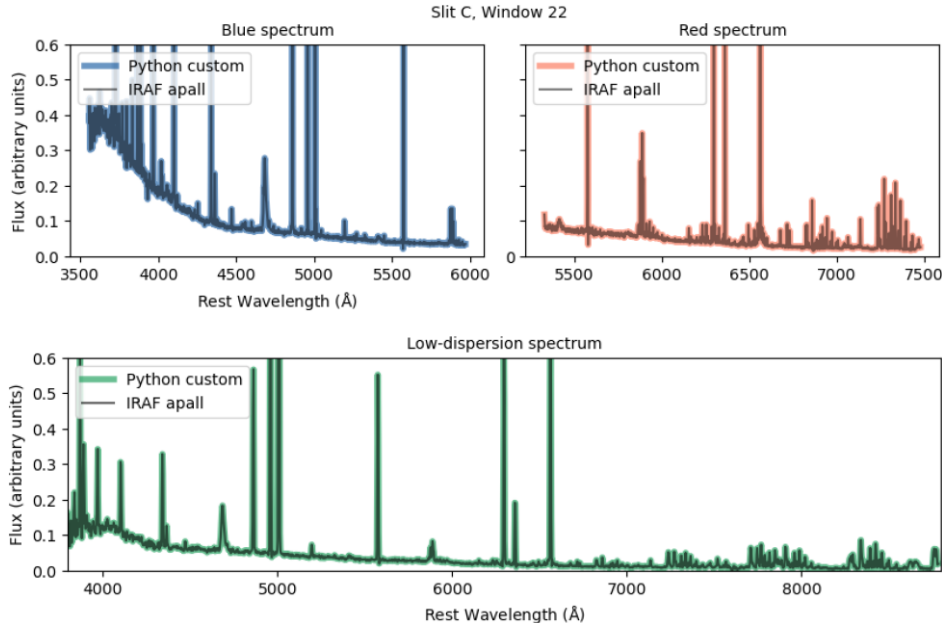


Figure A1. Comparison of spectra extracted from slit C and window 22 with our custom PYTHON routine (thick coloured curves) and IRAF’s apall routine (thin grey curves). The top two panels show the blue- and red-grism spectra, respectively, while the bottom panel shows the low-dispersion grism spectrum. The figure shows that the spectra extracted with PYTHON and IRAF are undistinguishable from each other.

use our custom PYTHON routine for the spectral extractions used in this work.

APPENDIX B: MATCHING THE FLUX LEVELS OF THE BLUE AND RED GRISMS

As shown in the top panel of Fig. B1, which corresponds to the spectra extracted from slit C at window 22 of Fig. 1, the continuum level of the red spectrum (red curve) does not match the continuum level of the blue spectrum (blue curve). The top panel of Fig. B1 is just an example but this is true in general. Thus, a correction needs to be applied. For this purpose, we use the low-dispersion spectrum, which is shown in grey in Fig. B1. We proceed as follows. First, we use Gaussian fitting and a custom PYTHON routine to obtain the fluxes, F , of the hydrogen H α and H β emission lines in the high (h)- and low (l)-dispersion spectra, i.e. $F_h(\text{H}\alpha)$ and $F_h(\text{H}\beta)$, and $F_l(\text{H}\alpha)$ and $F_l(\text{H}\beta)$, respectively. If for the blue spectrum, $F_h(\text{H}\beta) > F_l(\text{H}\beta)$, then we divide the flux array of the blue spectrum by $F_h(\text{H}\beta)/F_l(\text{H}\beta)$. Otherwise, we multiply it by $F_l(\text{H}\beta)/F_h(\text{H}\beta)$. We proceed similarly for the red spectrum, but this time we use the ratio of the H α fluxes instead. The bottom panel of Fig. B1 shows that this procedure fixes the problem.

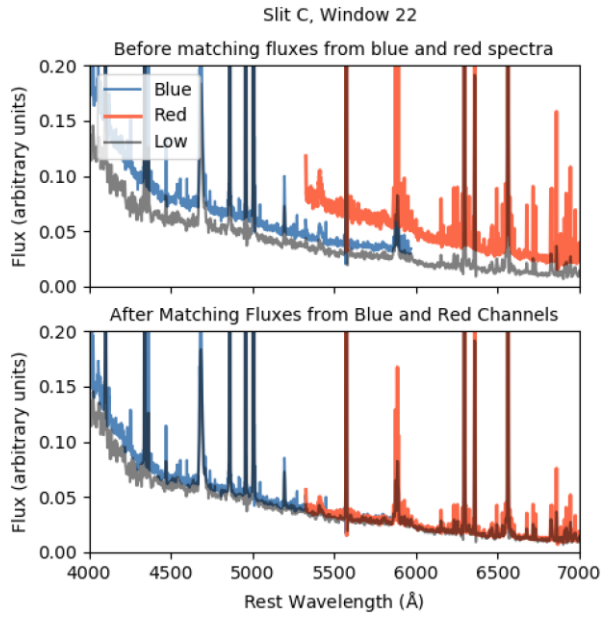


Figure B1. Spectra from the blue channel (thin blue curve) and red channel (thick red curve) before and after matching the flux levels (top and bottom panels, respectively). The grey curve shows the low-dispersion spectrum that was used for matching both channels.

This paper has been typeset from a $\text{\TeX}/\text{\LaTeX}$ file prepared by the author.

2. Extreme broad He II emission at high and low redshifts: the dominant role of VMS in NGC 3125-A1 and CDFS131717.

2.1. Resumen

El supercúmulo estelar (SSC, por sus siglas en inglés) A1 ($3.1 \times 10^5 M_{\odot}$) de la galaxia NGC 3125 muestra una línea de emisión de He II $\lambda 1640$ excepcionalmente ancha ($EW \sim 4.6 \pm 0.5 \text{ \AA}$, $FWHM = 1131 \pm 40 \text{ km s}^{-1}$), lo que la convierte en un valioso punto de referencia para interpretar observaciones de emisores extremos de He II a desplazamientos al rojo de hasta $z \sim 2-3$. Para este trabajo realizamos un análisis con observaciones de A1 tomadas con el Espectrógrafo de Orígenes Cósmicos (COS) del Telescopio Espacial Hubble (HST), las cuales revelan que no hay contaminación significativa de la línea de He II por emisión nebulosa y que la línea de He II está corrida al rojo $121 \pm 17 \text{ km s}^{-1}$ en relación con las líneas del medio interestelar.

Comparamos las observaciones COS G130M + G160M de A1 (1150 - 1750 \AA) con los últimos modelos BPASS y Charlot & Bruzual (C&B) de síntesis de población estelar simple (SSP), que incluyen estrellas muy masivas (VMS) de hasta $300 M_{\odot}$. Discutimos por qué los modelos BPASS con binarias cercanas no consiguen reproducir las propiedades de la línea He II de A1. Por otro lado, el modelo C&B (sin contemplar rotación) con $Z = 0.008$ y edad = 2.2 Myr presenta un buen ajuste a la línea de He II, esto debido a la proximidad al límite de Eddington que tienen las VMS en el modelo. Este modelo también reproduce las emisiones de C III $\lambda 1175$, N V $\lambda 1240$ y C IV $\lambda 1550$ del viento estelar.

Adicionalmente, presentamos predicciones del perfil de línea de O V $\lambda 1371$ para SSP pobres en metales, mostrando que la línea es fuerte para edades inferiores a 3 Myr y sirve como un importante marcador de juventud y VMS. Por último, analizamos la presencia de VMS en CDFS131717, una galaxia de baja metalicidad con gran actividad de formación estelar situada a $z = 3.071$, para la cual tenemos una tentativa detección de absorción de O V y una clara emisión fuerte y amplia de He II. Estos perfiles son raros y apuntan a la existencia de VMS de vida corta en la galaxia. Nuestros resultados muestran los efectos de la teoría de vientos estelares impulsados por radiación más recientes y la importancia de incorporar VMS en los modelos de síntesis de población estelar.

2.2. Contribución

Tomando los espectros reducidos de NGC 3125-A1 (A1), comparé los modelos de síntesis de población estelar (SSP) de C&B para metalicidades entre $Z=0.001$ y $Z=0.01$, tomando finalmente las de metalicidades de $Z = 0.006$ y $Z = 0.008$ siendo estas más cercanas a la metalicidad de la galaxia, tanto para aquellos que contienen estrellas individuales por encima de $100 M_{\odot}$ y $300 M_{\odot}$. Lo anterior para todas las edades disponibles en los modelos. Haciendo uso de una

prueba estadística de χ^2 , determiné que el modelo que mejor ajusta la emisión de He II corresponde a $Z = 0.008$ y una edad de 2.2 Myr. Dicho modelo también provee un buen ajuste a las líneas del viento estelar: C III $\lambda 1175$, N V $\lambda\lambda 1238, 1241$ y C IV $\lambda\lambda 1548, 1551$ (ver sección 4 del artículo asociado para más detalles).

Una vez identificado el modelo que mejor ajusta nuestras observaciones, grafiqué el número de estrellas WN, WC y WO, así como el número de estrellas O y la tasa de fotones ionizantes de He II de los modelos SSP, observando que la tasa de fotones ionizantes de He II aumenta con la aparición de las estrellas WR, específicamente las WNL y WNE, contrario a lo que esperábamos debido a los densos vientos de estas estrellas Sixtos et al. (2023, , primer artículo de ésta tesis).

Siguiendo el procedimiento de (Wofford et al., 2014), calculé el valor de la masa en estrellas del cúmulo A1. Para ello obtuve un flujo promedio alrededor de la longitud de onda de 1500 ± 3 Å en las observaciones y en el modelo adoptado ($Z = 0.008$, edad de 2.2 Myr, con estrellas individuales de más de $300 M_\odot$), en las observaciones realicé una corrección por enrojecimiento intrínseco (A1) y debido a polvo en la Vía Láctea. Utilizando una distancia de 11.5 Mpc, obtuve la luminosidad a esta longitud de onda y así la masa del cúmulo, la cual corresponde a $1.9 \times 10^5 M_\odot$ (para más detalles ver sección 5.2 del artículo asociado).

Finalmente, calculé el número de estrellas O ($N(O)_{obs}$) en A1, relacionando el número de estrellas O en nuestro modelo SSP ($N(O)_{theo}$) de masa $10^6 M_\odot$ y el cociente de las luminosidades en 1500 Å previamente calculadas, es decir, $N(O)_{obs} = N(O)_{theo} \times (L_{1500, theo}/L_{1500, obs})$. El número de estrellas O obtenido es de 172, el cual es tres veces menos que el encontrado en (Wofford et al., 2014) (para más detalles ver el último párrafo de la sección 5.2 en el artículo dos).

Para cada uno de los resultados descritos anteriormente, escribí los detalles en el artículo. Así mismo, participé en la respuesta a los comentarios realizados por el árbitro.

Extreme broad He II emission at high and low redshifts: the dominant role of VMS in NGC 3125-A1 and CDFS131717

Aida Wofford ¹★ Andrés Sixtos ¹, Stephane Charlot, ² Gustavo Bruzual, ³ Fergus Cullen ¹, Thomas M. Stanton ¹, Svea Hernández, ⁵ Linda J. Smith ⁶ and Matthew Hayes ¹

¹Instituto de Astronomía, Universidad Nacional Autónoma de México, Unidad Académica en Ensenada, Km 103 Carr. Tijuana–Ensenada, Ensenada, B.C., C.P. 22860, México

²Sorbonne Université, CNRS, UMR 7095, Institut d’Astrophysique de Paris, 98 bis bd Arago, 75014 Paris, France

³Instituto de Radioastronomía y Astrofísica, UNAM Campus Morelia, Apartado postal 3-72, 58090 Morelia, Michoacán, México

⁴Institute for Astronomy, University of Edinburgh, Royal Observatory, Edinburgh, EH9 3HJ, UK

⁵AURA for ESA, Space Telescope Science Institute, 3700 San Martin Drive, Baltimore, MD 21218, USA

⁶Space Telescope Science Institute, 3700 San Martin Drive, Baltimore, MD 21218, USA

⁷Department of Astronomy and Oskar Klein Centre for Cosmoparticle Physics, AlbaNova University Centre, Stockholm University, SE-10691, Stockholm, Sweden

Accepted 2023 May 23. Received 2023 May 22; in original form 2023 March 6

ABSTRACT

Super star cluster (SSC) A1 ($3.1 \times 10^5 M_{\odot}$) in NGC 3125 has one of the strongest ($EW = 4.6 \pm 0.5 \text{ \AA}$) broad ($FWHM = 1131 \pm 40 \text{ km s}^{-1}$) He II $\lambda 1640$ emission lines in the nearby universe and constitutes an important template for interpreting observations of extreme He II emitters out to redshifts of $z \sim 2 - 3$. We use Cosmic Origins Spectrograph (COS) observations of A1 to show that there is no significant contamination of the He II line with nebular emission and that the line is redshifted by $121 \pm 17 \text{ km s}^{-1}$ relative to ISM lines. We compare the COS G130M + G160M observations of A1 to recent binary BPASS and single-star Charlot & Bruzual (C&B) simple stellar population (SSP) models with very massive stars (VMS) of up to $300 M_{\odot}$. On the other hand, we suggest why BPASS models fail to reproduce A1’s He II emission. On the other hand, a C&B model with $Z = 0.008$, age = 2.2 Myr, and VMS approaching the Eddington limit provides an excellent fit to the He II emission and fits reasonably well C III $\lambda 1175$, N V $\lambda\lambda 1238, 1241$, and C IV $\lambda\lambda 1548, 1551$. We present O V $\lambda 1371$ line-profile predictions showing that this line constitutes an important tracer of youth and VMS in galaxies. Finally, we discuss the presence of VMS in CDFS131717, a highly star-forming low-metallicity galaxy located at $z = 3.071$, which has a tentative detection of O V absorption and strong broad He II emission. These features are rare and hint to the presence of short-lived VMS in the galaxy. Our results show the effect of the latest developments of stellar wind theory and the importance of accounting for VMS in models.

Key words: techniques: spectroscopic – galaxies: starburst – ultraviolet: galaxies – ultraviolet: stars.

1 INTRODUCTION

1.1 Starburst galaxies, massive stars, and cosmic noon

Starburst galaxies are characterized by massive violent bursts of star formation. They are powered by populations of hot stars with progenitor masses of $5 M_{\odot}$ and above, which have main diagnostic lines in the satellite ($< 3200 \text{ \AA}$) ultraviolet (UV Leitherer et al. 2001). Locally, starburst galaxies are responsible for 20 per cent of star formation in galaxies (Brinchmann et al. 2004). Nearby starburst galaxies are the most obvious local counterparts of the normal star-forming galaxies discovered at high redshift, in particular galaxies located at redshifts of $z \sim 2 - 3$, that is, at the epoch of ‘cosmic noon’. The epoch of cosmic noon is ideal to examine the mechanisms of star formation because it is when galaxies formed about half of their current stellar mass (Förster Schreiber & Wuyts 2020). Stacked

spectra of star-forming cosmic-noon galaxies (e.g. Shapley et al. 2003; Cullen et al. 2019; Saxena et al. 2020), as well as single-object observations (Pettini et al. 2000; Erb et al. 2010; Rivera-Thorsen et al. 2019; Vanzella et al. 2020) provide a glimpse of the dominant stellar populations present at the peak of star formation in the universe, and in particular, the massive-star ($\geq 10 M_{\odot}$) content.

1.2 The broad He II problem at high and low redshift

Broad He II $\lambda 1640$ emission (hereafter, He II 1640) is the strongest stellar line in the stacked UV spectrum of 811 Lyman Break Galaxies (LBGs) located at $z \sim 3$ produced by Shapley et al. (2003). LBGs are star-forming galaxies that are selected using their differing appearance in several imaging filters due to the position of the Lyman limit. When Shapley et al. (2003) published their composite spectrum, the He II line was the only strongly discrepant stellar line when comparing the rest-frame UV spectra of LBGs to the UV templates of local starbursts, in particular those available at the

* E-mail: awofford@astro.unam.mx

time (Leitherer et al. 1999) from the widely used stellar population synthesis package Starburst99 (Leitherer et al. 2010).

In stacked spectra, the uncertainties in the redshifts of the galaxies that make up the spectrum contribute to some extent to the width of the composite He II line profile. However, a recent deep (20 h) Very Large Telescope (VLT) observation of a UV bright ($M_{UV} = -21.7$) non-lensed star-forming galaxy (ID = CDFS131717) that is located at $z_{\text{spec}} = 3.071$ and is part of the deep public ESO spectroscopic survey with VIMOS on the VLT, VANDELS (McLure et al. 2018; Garilli et al. 2021), clearly shows the existence of broad He II 1640 emission in single objects (Stanton et al., in preparation).

Alternatively, some nearby starburst galaxies show extreme broad He II emission lines that until very recently were also challenging to model with population synthesis models. This is the case of SSC A1 in galaxy NGC 3125. The extreme He II $\lambda 4686$ emission of this SSC was first noted by Kunth & Sargent (1981). In their study of nearby starburst galaxies with WR-star features observed with *HST*'s Space Telescope Imaging Spectrograph (STIS), Chandar, Leitherer & Tremonti (2004) confirmed the extreme nature of A1 using the He II 1640 line, which is the UV equivalent of the optical line at 4686 Å. The latter authors also studied NGC 3125 in the context of LBGs located at $z \sim 3$. Finally, Senchyna et al. (2021) studied a different sample of nearby broad He II 1640 emitters observed with *HST*'s Cosmic Origins Spectrograph (COS, an instrument with higher sensitivity and spectral resolution with respect to the STIS/G140L setup used by Chandar et al. 2004). The later authors only found one star-forming galaxy, SB 179, with a strength of the He II 1640 emission line similar to that of NGC 3125-A1.

In integrated spectra of massive-star populations, broad ($FWHM \approx 1000 \text{ km s}^{-1}$) He II emission suggests stellar winds as the formation mechanism. Strong, broad He II 1640 emission requires a high mass-loss rate (to produce a dense wind) and high temperature (to doubly ionize He), with He not necessarily overabundant (though He II emission is boosted if the star is He rich).

Since classical Wolf–Rayet (cWR) stars (He-burning, H-deficient) meet the first two conditions and are He rich, the presence of broad He II is generally thought to indicate the presence of WR stars. Alternatively, Very Massive Stars (VMS), which have initial masses of $M \geq 100 M_{\odot}$ (Vink 2015), that is, above the commonly used upper mass limit of the stellar IMF, can produce WR features even during core H-burning, independent of He enrichment. These are WNh stars, where the ‘W’ stands for ‘Wolf–Rayet’ and the ‘N’ and ‘h’ indicate the dominance of nitrogen emission lines and presence of hydrogen lines in the star’s spectrum, respectively (Smith & Conti 2008). In VMS, the reason for the increased *EW* of the He II $\lambda 4686$ stellar-wind line is almost certainly the proximity to the Eddington limit. This is shown in fig. 10 of Vink et al. (2011), where one sees that increasing the electron-scattering Eddington factor theoretically increases the mass-loss rate, and also empirically, the He II *EW*. A similar increase of the *EW* is expected for the UV line as well.

VMS have been found in star cluster R136, which is at the centre of LMC’s large H II region NGC 2070 (Crowther et al. 2010, 2016). R136 is $1 - 2.5$ Myr old (Brands et al. 2022) and has a binary-corrected virial mass of $M = 4.6 - 14.2 \times 10^4 M_{\odot}$ (Hénault-Brunet et al. 2012) that is consistent with the photometric mass of $\sim 5 \times 10^4 M_{\odot}$ that is reported in Andersen et al. (2009). There are several determinations of the initial mass of the most massive star in R136, R136a1: $320_{-40}^{+100} M_{\odot}$ (Crowther et al. 2010, based on *HST*UV spectroscopy from the Goddard High Resolution Spectrograph (GHRS) and the Faint Object Spectrograph + optical *VLT*/SINFONI spectroscopy + *VLT*/MAD IR, according to their table 1), 251_{-31}^{+48} (Bestenlehner et al. 2020, based on STIS UV

spectroscopy), $273_{-36}^{+25} M_{\odot}$ (Brands et al. 2022, based on STIS optical and UV spectroscopy) and $196_{-27}^{+34} M_{\odot}$ (Kalari et al. 2022, based on BVRI-like photometry from the Gemini speckle imager Zorro, which separates sources a1 and #9). On the other hand, in W14, we ruled out that the extraordinary He II emission and O V $\lambda 1371$ (O V 1371) absorption of NGC 3125-A1 are due to an extremely flat exponent of the upper IMF, and suggested that they originate in the winds of VMS. Furthermore, Smith et al. (2016) found evidence of the presence of VMS in cluster #5 of blue compact dwarf (BCD) galaxy NGC 5253 based on *HST*/UV and *VLT*/optical spectra, and Leitherer et al. (2018) suggested that VMS could explain the COS far-UV observations of SSC-N in BCD galaxy II Zw 40.

Several research groups have developed population synthesis models, that is, models that predict the photometric and spectroscopic properties of stellar systems, which account for the contribution of VMS (e.g. Gutkin, Charlot & Bruzual 2016; Byrne et al. 2022; Martins & Palacios 2022). In particular, Martins & Palacios (2022) discuss the expected effects of VMS in integrated spectra of massive-star populations and galaxies that host them. Martins & Palacios (2022) were the first to successfully reproduce NGC 3125-A1’s extraordinary He II 1640 line by accounting for enhanced mass-loss from VMS close to the Eddington limit. However, they did not generate a tailored model for this SSC.

1.3 This work

In this paper, we use high-quality UV data that have not been previously analysed in combination with state-of-the-art population synthesis models to further investigate if VMS can account for the extreme broad He II emission in NGC 3125-A1. In addition, we explore whether VMS can also account for the previously mentioned observation of CDFS131717.

In Section 2, we present NGC 3125-A1, summarize previous findings about this object, present the UV observations of NGC 3125-A1 used in this work, and data reduction. In Section 3, we describe the models used in our analysis of A1. In Section 4, we show the comparison of the models with the observations of A1. In Section 5, we discuss our results for A1 and their consequences for the interpretation of the rest-frame UV spectrum of high-z galaxy, CDFS131717. Finally, in Section 6, we provide our summary and conclusions.

2 TARGET, OBSERVATIONS, AND DATA REDUCTION

2.1 NGC 3125-A1

Nearby starburst galaxy NGC 3125 (Tol 3, distance estimates provided in Table 1) is of particular importance for studies of the upper stellar initial mass function (IMF; e.g. W14) and galaxies at cosmic noon (e.g. Chandar et al. 2004). The galaxy has an ionized-gas oxygen abundance of $12 + \log(\text{O/H}) = 8.3$ (Hadfield & Crowther 2006), which is consistent with abundances measured in the Large Magellanic Cloud (LMC) via collisionally excited lines (Russell & Dopita 1990; Toribio San Cipriano et al. 2017) and characteristic of some star-forming galaxies at cosmic noon (Steidel et al. 2016; Amorín et al. 2017; Cullen et al. 2021; Sanders et al. 2021). It is dominated by two emission regions, A and B. Region A can be subdivided into ultraviolet (UV)-bright and highly extinguished components A1 and A2, respectively (Hadfield & Crowther 2006). Given its young age and high mass (2.2 Myr and $1.9 \times 10^5 M_{\odot}$, respectively; values from this work; see also W14), A1 is considered

Table 1. Main properties of NGC 3125, region A, and SSC A1.

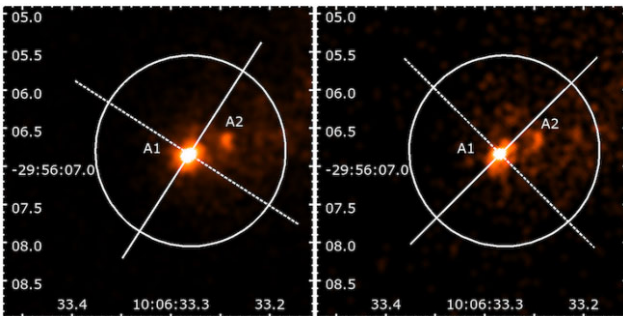
Property	Units	Value	Reference
RA _{NGC3125}	h:m:s	10:06:33.372	1
Dec _{NGC3125}	d:m:s	-29:-56:-5.500	1
RA _{A1}	h:m:s	10:06:33.280	2
Dec _{A1}	d:m:s	-29:-56:-6.800	2
Redshift	-	0.003712	3
Distance 1	Mpc	11.5	4a
Distance 2	Mpc	14.84 ± 1.04	4b
$E(B - V)_{MW}$	mag	0.073	5
$E(B - V)_{A1}$	mag	0.130	6
$12 + \log(O/H)_A$	dex	8.32 ± 0.03	7

Notes. Reference:

- (1) J2000 right ascension (h:m:s) or declination (d:m:s) of galaxy from Strasbourg astronomical Data Centre (<http://cdsweb.u-strasbg.fr/>).
- (2) J2000 right ascension (h:m:s) or declination (d:m:s) of A1 used for COS observations from <https://archive.stsci.edu/missions-and-data/hst>.
- (3) Redshift from NASA/IPAC Extragalactic Data base (NED, <https://ned.ipac.caltech.edu/>).
- (4a) Value derived from the Galactic Standard of Rest velocity using a Hubble constant of $H_0 = 75 \text{ km s}^{-1} \text{ Mpc}^{-1}$, obtained by Schaefer, Contini & Kunth (1999), and adopted in W14 for comparison of the SSC masses and numbers of O and WR stars with previous works.
- (4b) Virgo + GA + Shapley distance (Mould et al. 2000) from NED for cosmological parameters: $\Omega_{\text{matter}} = 0.308$, $\Omega_{\text{vacuum}} = 0.692$, and $H_0 = 67.8 \text{ km s}^{-1} \text{ Mpc}^{-1}$
- (5) Colour excess due to dust in the Milky Way from: <https://noirlab.edu>.
- (6) Colour excess due to intrinsic dust from W14.
- (7) Oxygen abundance in the ionized gas from Hadfield & Crowther (2006).

Table 2. Summary of COS spectroscopic observations.

Data set	Grating	Cen Wave/Å	Exp Time/s	PID
LBJS01010	G130M	1300	2549.184	12 172
LBJS01020	G130M	1318	2971.200	12 172
LE4GP2010	G160M	1600	4880.640	15 828
LE4GP2020	G160M	1623	5188.640	15 828

**Figure 1.** COS NUV MIRRORA TA images of programs 12 172 (left; data set: LBJS01IOQ) and 15 828 (right; data set: LE4GP2ZCQ), with COS footprint overlaid (circle). North is up and east is to the left. The dashed lines indicate the PA angles of the programs, (149° and 135°, respectively). The exposure times are 30 and 6 s, respectively.

to be a super star cluster (SSC, Johnson 2001; Adamo et al. 2020). Table 1 lists main properties of the galaxy, region A, and SSC A1.

In W14, we present *Hubble Space Telescope* (*HST*) UV spectra of A1 obtained by PI Leitherer with two spectrographs: (i) the STIS, using the $2'' \times 50''$ long slit (effectively a $2'' \times 25''$ slit due to the size of the STIS FUV MAMA detector) and the G140L grating

($R \sim 1000$, i.e. $\sim 300 \text{ km s}^{-1}$ at 1640 Å); and (ii) the COS, using the $2.5''$ -wide circular Primary Science Aperture (PSA) and the G130M grating ($R \sim 20\,000$, i.e. $\sim 15 \text{ km s}^{-1}$ at 1640 Å). We also show that the spectroscopically derived mass of A1 is of the same order of magnitude as the binary-corrected virial mass of star-forming region NGC 2070 in the LMC ($4.5 \times 10^5 \text{ M}_\odot$) and consistent with a mass estimate from photometry (Bosch, Terlevich & Terlevich 2009). The STIS observation analysed in W14 shows that A1 is characterized by the presence of a broad He II 1640 emission line with a large equivalent width ($FWHM = 1131 \pm 40 \text{ km s}^{-1}$ and $EW = 4.6 \pm 0.5 \text{ \AA}$, respectively, values from this work) and stellar O V $\lambda 1371$ absorption. W14 show that the He II emission in the STIS spectrum of A1 cannot be reproduced with standard Starburst99 models (Leitherer et al. 2010).

2.2 Observations

Observations of NGC 3125-A1 were obtained with COS G130M and G160M gratings as part of *HST* programs 12 172 (PI Leitherer, on November 2011; lifetime position, LP1) and 15 828 (PI Wofford, on October 2020; LP4), respectively. In particular, we use the data sets that are listed in column 1 of Table 2. The table gives the grating, central wavelength, and exposure time of the observations. The spectra were obtained with the PSA. To provide continuous coverage from $\sim 1150 - 1800 \text{ \AA}$, we used two central wavelengths (cenwave) with each grating. To improve the quality of the spectra, we used four focal-plane positions with each cenwave. The observations have a wavelength-dependent resolving power in the range, $R \sim 15\,000 - 20\,000$.

As described in James (2022), offsets in flux between different gratings and cenwaves can be observed in COS observations of extended objects obtained with different position angles (PAs). We inspected the individual exposures of both gratings in the overlapping regions and found no flux offsets between the different sets. This is in agreement with the fact that both sets were observed at comparable PAs (135° and 149° for G130M and G160M, respectively). The target was acquired using MIRROR A. The near-UV (NUV) acquisition images from programs 12 172 (G130M) and 15 828 (G160M) are shown in the left and right panels of Fig. 1, respectively. In spite of the lower exposure time used in the TA corresponding to program 15 828, the fainter A2 cluster is clearly seen in the right panel of the figure. According to Hadfield & Crowther (2006) the total colour excesses of A1 and A2 are: $E(B - V) \sim 0.24$ and ~ 0.58 mag, respectively; and A1 has an NUV flux in the *HSTFOC* F220W band that is approximately 3.2 times larger than that of A2.

2.3 Data reduction

The observations were retrieved from the Mikulski Archive for Space Telescopes (MAST) and calibrated on-the-fly using *HST*'s CALCOS code version V3.4.0 (Soderblom 2021). The latest version of the CALCOS pipeline does not provide co-added products combining different gratings and central wavelengths. We further process the individual COS x1d files using the IDL code developed by the COS Guaranteed Time Observer Team (Danforth et al. 2010). The individual x1d spectra were weight-combined (using the exposure times as weighting factors) by interpolating onto a common wavelength vector. Lastly, we bin the combined spectrum by a single COS resolution element (1 resel = 6 pixels), corresponding to the nominal point-spread function. We checked the wavelength calibration accuracy by comparing the position of the MW absorption

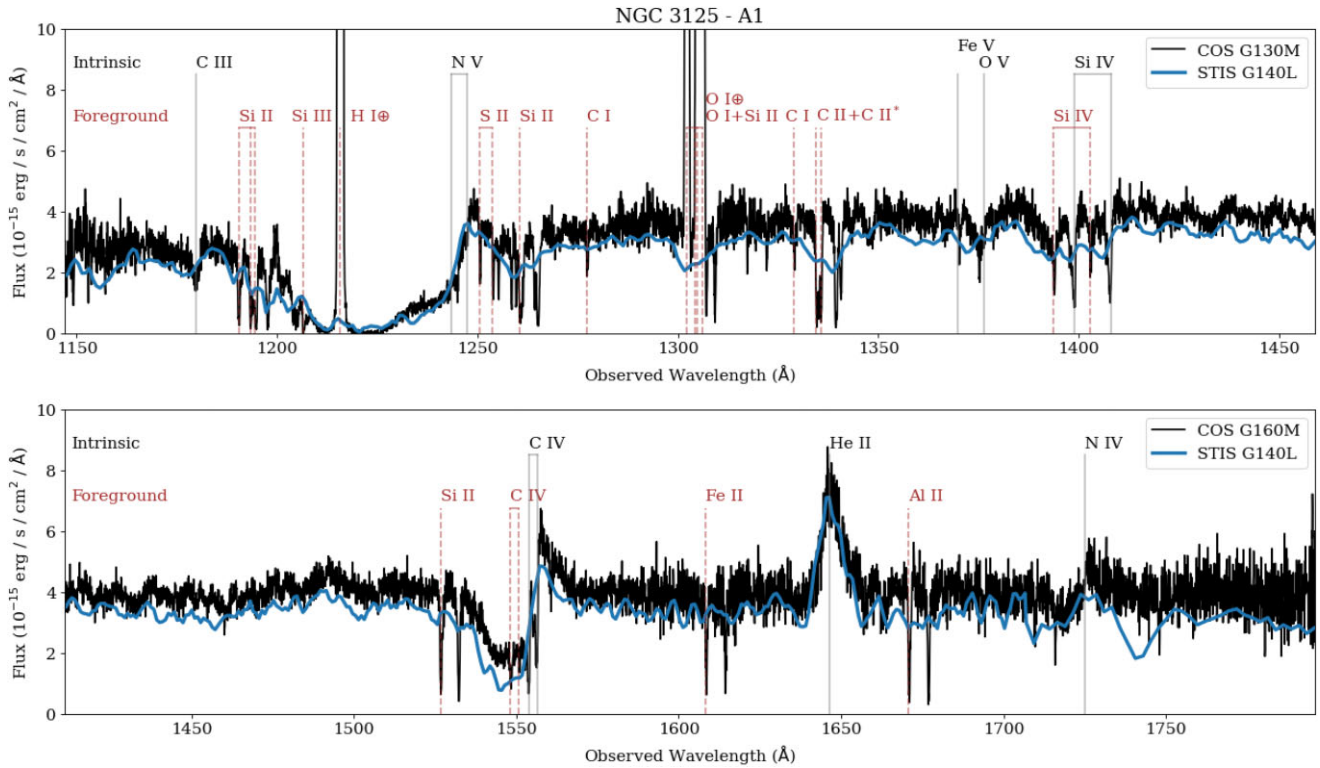


Figure 2. NGC 3125-A1 spectra, uncorrected for any reddening due to dust and redshift, obtained with COS G130M + G160M (black curve) and STIS G140L (blue curve), using the 2.5'' circular and 2'' \times 25'' long-slit apertures, respectively. We mark the positions of intrinsic stellar-wind and photospheric features with solid vertical grey lines. The cores of some of these features are contaminated with ISM absorptions. The ions that the features originate from are indicated with black characters. We also mark the positions of strong foreground contaminating features with dashed vertical brown lines, including the geocoronal H I and O I emission lines, which are identified by the Earth's symbol. Note the broad absorption at ~ 1216 Å due to the H I Ly α absorptions of the MW and the galaxy. The limits of the top and bottom panels are [1147, 1459] and [1411, 1796] Å, respectively, and correspond to the limits covered by the G130M and G160M observations.

line Si II $\lambda 1190.42$ Å and Al II $\lambda 1670.79$. We find offsets of about ~ 0.05 Å that are within the wavelength accuracy of COS (0.06 Å).

Fig. 10 of W14 shows a comparison between COS G130M and STIS G140L spectra of NGC 3125-A1. Fig. 2 shows a similar figure where the wavelength range has been extended in order to include the unpublished COS G160M observations. In Fig. 2, we identify the strongest foreground and intrinsic spectral features. For this purpose, we use the line list in table 1 of Leitherer et al. (2011). The difference in flux between the STIS and COS observation is due to the difference in apertures.

Fig. 2 shows that the NGC 3125-A1 profiles of N V $\lambda\lambda 1238, 1241$ (N V 1240), C IV $\lambda\lambda 1548, 1551$ (C IV 1550), and He II 1640; and Milky Way (hereafter MW) + NGC 3125-A1 H I Ly α absorptions are remarkably similar in the COS and STIS observations. However, the STIS observation has a lower spectral resolution. This makes it hard to see weak narrow ISM absorption lines and to distinguish between intrinsic and foreground ISM lines, except when these are sufficiently strong, as is the case for the C II, C II* $\lambda\lambda 1334, 1336$, and Si IV $\lambda\lambda 1393, 1403$ (Si IV 1400) doublets. Note that the weaker N IV $\lambda 1718$ P-Cygni like profile is much clearer in the COS data.

There is a striking similarity between the spectrum of NGC 3125-A1 that we show in Fig. 2 and the spectrum of VMS, R136a3, which is shown in fig. 5 of Crowther et al. (2010) (top panel). The VMS spectrum was obtained with the GHRS, an instrument that is no longer on board of *HST*. For reference, R136a3 is located in the LMC, is classified as a hydrogen-rich WN5h star, and has an initial mass of 155^{+25}_{-18} (Kalari et al. 2022).

2.4 Normalization and Ly α correction

Removing the Ly α absorption profiles of the MW and NGC 3125 from the COS observations is a critical step for finding an accurate model fit to the observations. This is because these absorptions severely contaminate the N V 1240 stellar doublet. We correct for Ly α absorption by adopting a similar approach and software as those described in Hernandez et al. (2020, 2021) and Sirressi et al. (2022).

As a first step, we normalize the COS spectrum by interpolating between nodes manually positioned to avoid stellar and ISM features. To guide the normalization and location of the nodes, we use a Staburst99 (Leitherer et al. 1999, 2014) instantaneous burst model of LMC metallicity. We adjust the tension of the cubic spline between the nodes as needed to closely match the rectified luminosities of the model.

Using the normalized spectrum we fit Voigt profiles to the Lyman α absorption using the Python software VoigtFit v.3.13.9 (Krogager 2018). We note that given the radial velocity of NGC 3125, the Ly α absorption originating from the MW is blended with the galaxy absorption. We fit both Ly α absorption components (MW and NGC 3125) simultaneously. We set the b value for both MW and NGC 3125 to 0, since the line is in the damped part of the curve of growth; and the velocity for the MW is set to 0 km s $^{-1}$. The VoigtFit software allows users to incorporate the line-spread function (LSF) information to account for the wavelength-dependent resolution intrinsic to the instrument. Given that NGC 3125-A1 is observed to be an extended source, we convolve the COS LSF profiles with the FWHM of the target in the dispersion direction, as measured from

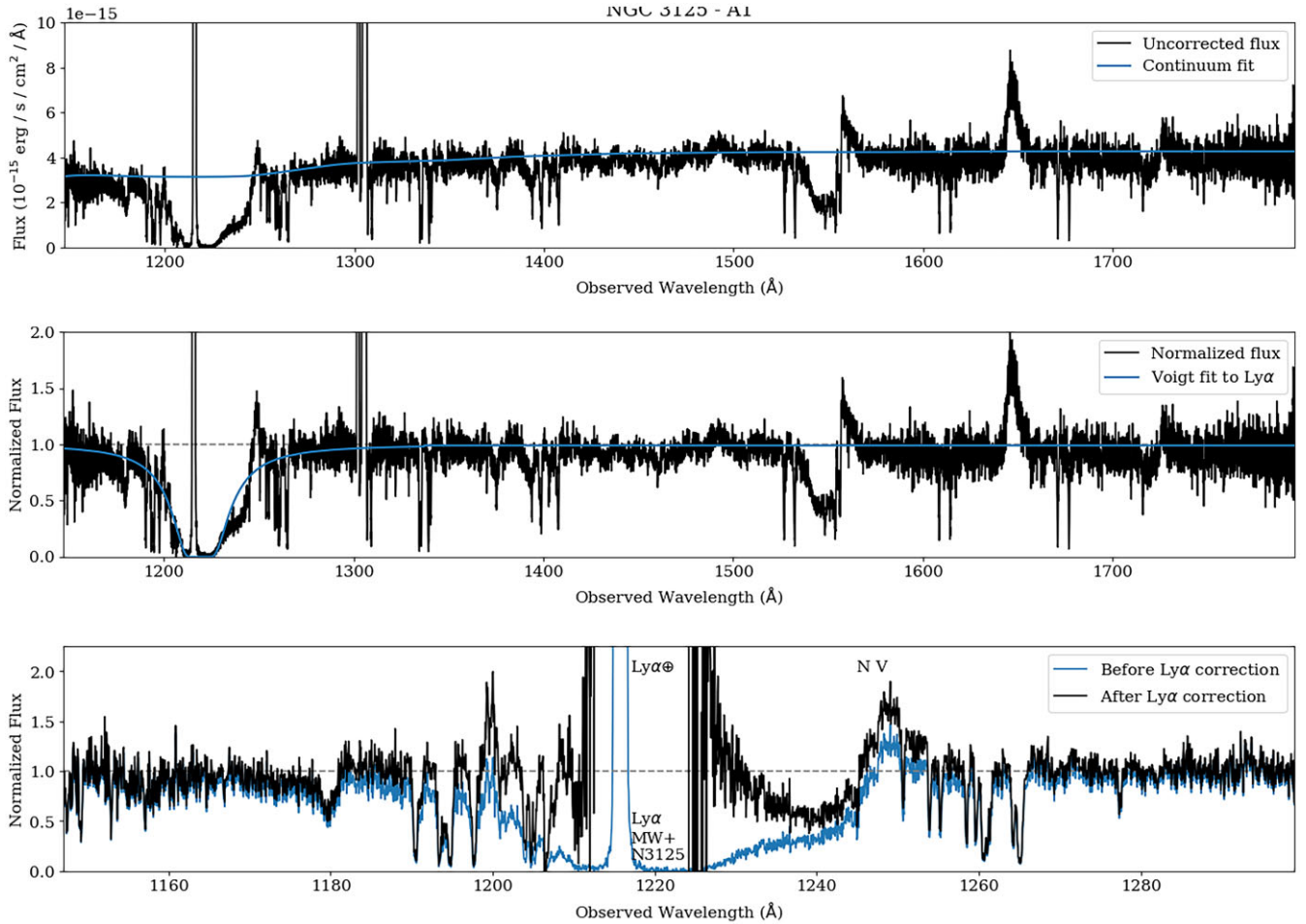


Figure 3. Plots corresponding to steps we follow to normalize and correct for Ly α the COS G130M + G160M spectrum. Top panel – COS spectrum (black curve) and fit to the continuum (blue curve). Middle panel – normalized COS spectrum resulting from dividing the flux by the fit to the continuum. Bottom panel – Comparison of normalized spectra before and after correcting for the Ly α absorptions (blue and black curves, respectively).

the COS acquisition images, and use the broadened LSFs to specify the resolution of the observations within `VoigtFit`. The final spectral resolution of the observations is derived using equation (1) in Hernandez et al. (2020). We obtain the best Ly α fit when masking contaminating stellar and ISM absorption features, particularly the broad N V 1240 absorption on the red wing of Ly α . We fit for the hydrogen column densities NH I(MW), NH I(NGC 3125), and the velocity of NGC 3125. We measured a column density of H I of log NH I = 21.752 ± 0.126 cm $^{-2}$ for NGC 3125. The inferred NH I(MW) agrees with the measured 21 cm value from the all-sky map from HI4PI (<http://cdsarc.u-strasbg.fr/viz-bin/qcat?J/A+A/594/A116>). We divide the normalized COS spectrum by the best Ly α fit to remove the contaminating profile.

In Fig. 3, we show the steps followed to normalize and correct the COS G130M + G160M spectrum for the Ly α absorptions. The top panel shows the fit to the observed continuum. The middle panel shows the normalized spectrum that results from dividing the observed spectrum by the fit to the continuum. It also shows the fit to the Ly α absorption components. Finally, the bottom panel shows the comparison between the normalized spectra before and after correcting for the Ly α absorptions. The bottom panel clearly shows that the strength of the emission component of the P-Cygni like profile of N V $\lambda\lambda 1238, 1242$ becomes stronger after the Ly α correction.

3 POPULATION SYNTHESIS MODELS

In W14, we speculated that VMS are present in NGC 3125-A1. However, it was not until recently that population synthesis models accounting for VMS became available (e.g. Senchyna et al. 2021; Martins & Palacios 2022). Martins & Palacios (2022) were the first to reproduce A1's He II line with VMS approaching the electron-scattering Eddington limit. In their modelling, they use a BPASS SSP with single stars corresponding to $Z = 0.006$, age = 2 Myr, and upper mass limit of the IMF of $100 M_{\odot}$. They supplement this SSP with VMS models generated with stellar evolution tracks from STAREVOL (Siess, Dufour & Forestini 2000; Lagarde et al. 2012; Amard et al. 2019), stellar atmospheres from CMFGEN (Hillier & Miller 1998), and the mass-loss rates of Gräfener (2021). Although their solution overproduces emission in N V 1240 (see their fig. 11), this could be because they do not correct the STIS observation for the nearby LyA absorptions of the MW and NGC 3125. The C IV 1550 emission component is also overproduced in their model. Nevertheless, the fact that they are able to reproduce A1's extreme He II emission constitutes a great accomplishment.

The COS observations that we use in this work have higher spectral resolution and SNR in the continuum compared to the STIS observation used by Martins & Palacios (2022). They also cover a longer wavelength range, and in particular, the He II 1640 line at

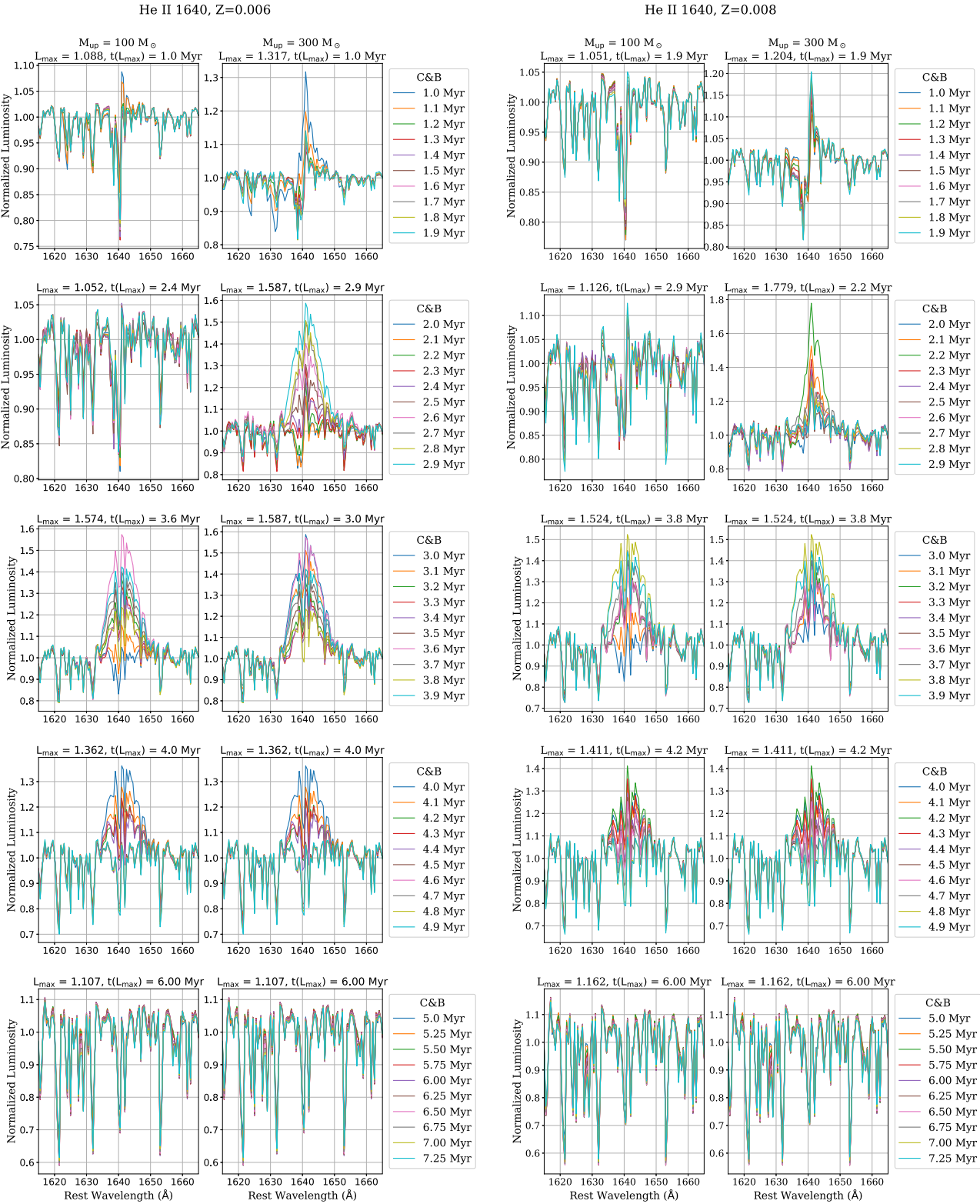


Figure 4. First two columns – C&B He II 1640 line-profile predictions for SSPs with $Z = 0.006$ and $M_{\text{up}}/\text{M}_{\odot} = 100$ (1st column) or $M_{\text{up}}/\text{M}_{\odot} = 300$ (2nd column). We use a linear fit between continuum windows [1615, 1620] and [1660, 1665] to normalize the He II lines. In each panel, the curves of different colours correspond to models of 10 different ages, as given by the right-hand side legends. We give in each panel, the maximum luminosity in the wavelength range [1620, 1660] Å that is reached in the panel, that is, the amplitude of He II line when it is in emission; and the corresponding age. Models are available for ages in logarithmic space. Last two columns – Similar but for $Z = 0.008$. The maximum amplitude of He II is obtained for $Z = 0.008$, $M_{\text{up}}/\text{M}_{\odot} = 300$, and 2.2 Myr.

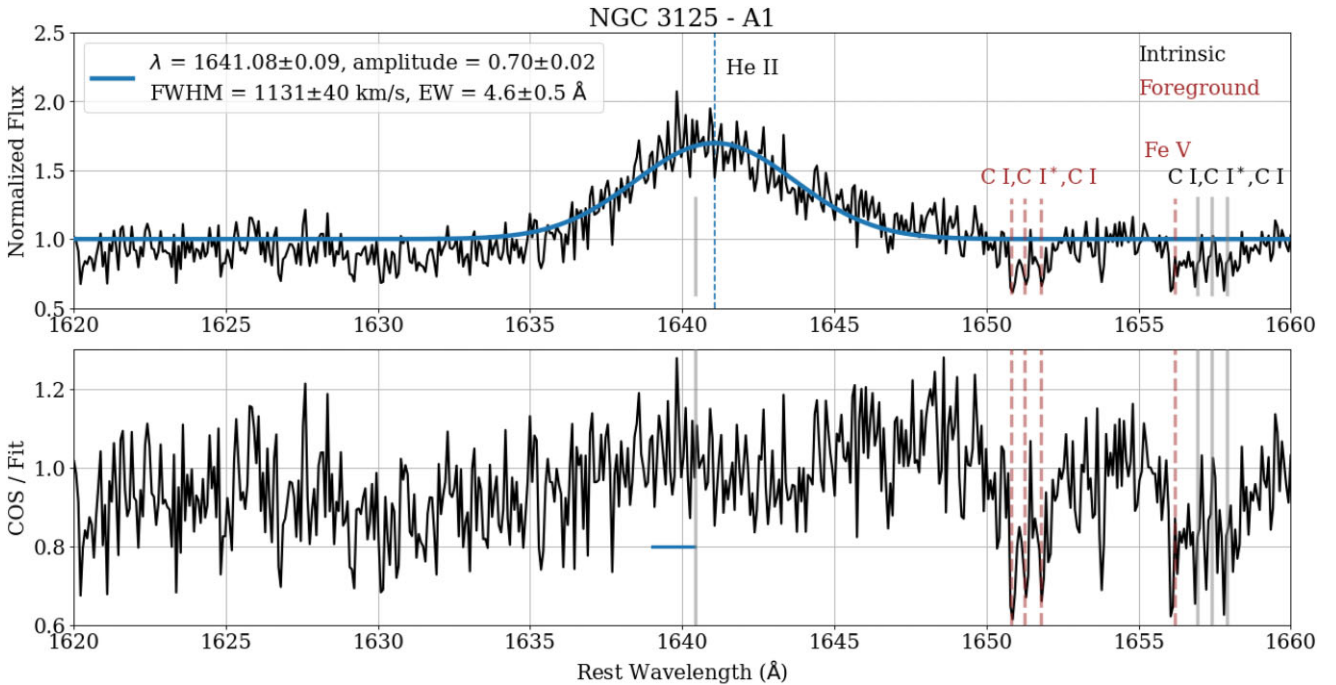


Figure 5. Top panel – normalized portion of the spectrum around the intrinsic He II 1640 line (black curve), and Gaussian fit to the line (blue curve). The spectrum is corrected for the redshift of the galaxy. After this correction, the observed He II line, whose position at 1641.08 \AA is marked by a vertical blue-dashed line, shows an additional redshift of $121 \pm 17 \text{ km s}^{-1}$ relative to the expected rest-frame position at 1640.42 \AA , which is marked by the short vertical grey line. The fit parameters are given in the legend. Bottom panel – observation divided by fit (black curve). In both panels, we use thick brown-dashed and grey-solid vertical lines to mark the positions of foreground and intrinsic lines. The corresponding ions are indicated in the top panel.

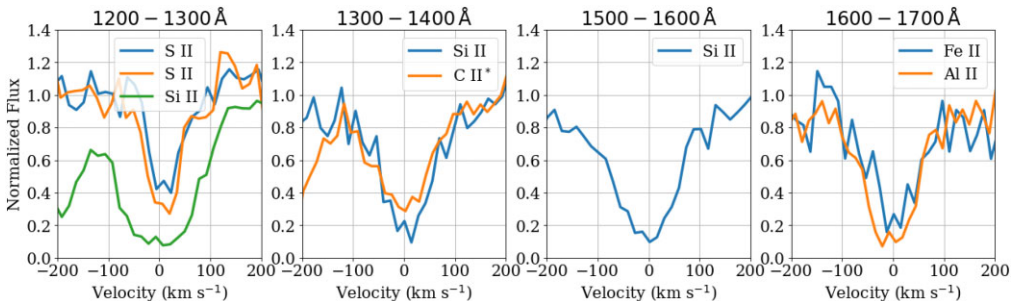


Figure 6. Selection of ISM lines along A1's line of sight that are: free of strong contamination by nearby lines, from the ions given by the legends, and present in the wavelength intervals given by the titles of the panels. According to Leitherer et al. (2011), the rest-wavelengths of the lines from each ion are: S II at 1250.58 and 1253.81 Å; Si II at 1260.42, 1304.37, and 1526.71 Å; C II* at 1335.71 Å, Fe II at 1608.45 Å; and Al II at 1670.79 Å. We show the redshift-corrected spectra ($z = 0.003712$). The centroids of all lines are at rest.

higher spectral resolution. We use these higher quality observations to test the Charlot & Bruzual (hereafter C&B) population synthesis models (Plat et al. 2019). The stellar ingredients used in the C&B models are explained in detail in Sánchez et al. (2022, Appendix A, Tables 8 – 12). These models cover in detail the evolution of O and B stars, including the Wolf-Rayet (WR) phase, and account for the contribution of VMS of up to $300 M_{\odot}$. The models use the PARSEC stellar evolution tracks of Chen et al. (2015), which are for single, non-rotating stars. The tracks take into consideration the formulation of mass-loss rates by Vink et al. (2011). In summary, for atmospheres and synthetic spectra of massive stars on the Main Sequence (MS) that are not flagged as WR stars according to the criteria provided in Section 3.2 of Chen et al. (2015), WM-Basic (Pauldrach, Hoffmann & Lennon 2001; Leitherer et al. 2010) models are used. To complete the wavelength-range coverage, the latter

models are supplemented with TLUSTY (Lanz & Hubeny 2003, 2007) models. If the star is flagged as WR according to the previous criteria, then C&B use the model atmospheres and synthetic spectra of WR stars from the Potsdam group (PoWR, Gräfener, Hamann, Sander, Shenar, Hainich, Todt et al.), regardless of whether the star is on the MS or elsewhere. A description of how PARSEC and PoWR models are coupled is specified in the appendix of Plat et al. (2019). Note that the mass-loss rates of WR stars from the PARSEC tracks are higher than the values predicted by Vink et al. (2011) for stars of the same mass. However, for MS O stars they are consistent. Inhomogeneities in the wind, that is, clumping in the wind is not accounted for. Since the observation is dominated by cluster A1, we assume a Simple Stellar Population (SSP), that is, a single burst of star formation. In addition, we exclude the contribution of the ionized gas, as no nebular emission lines are present in the spectra. We leave

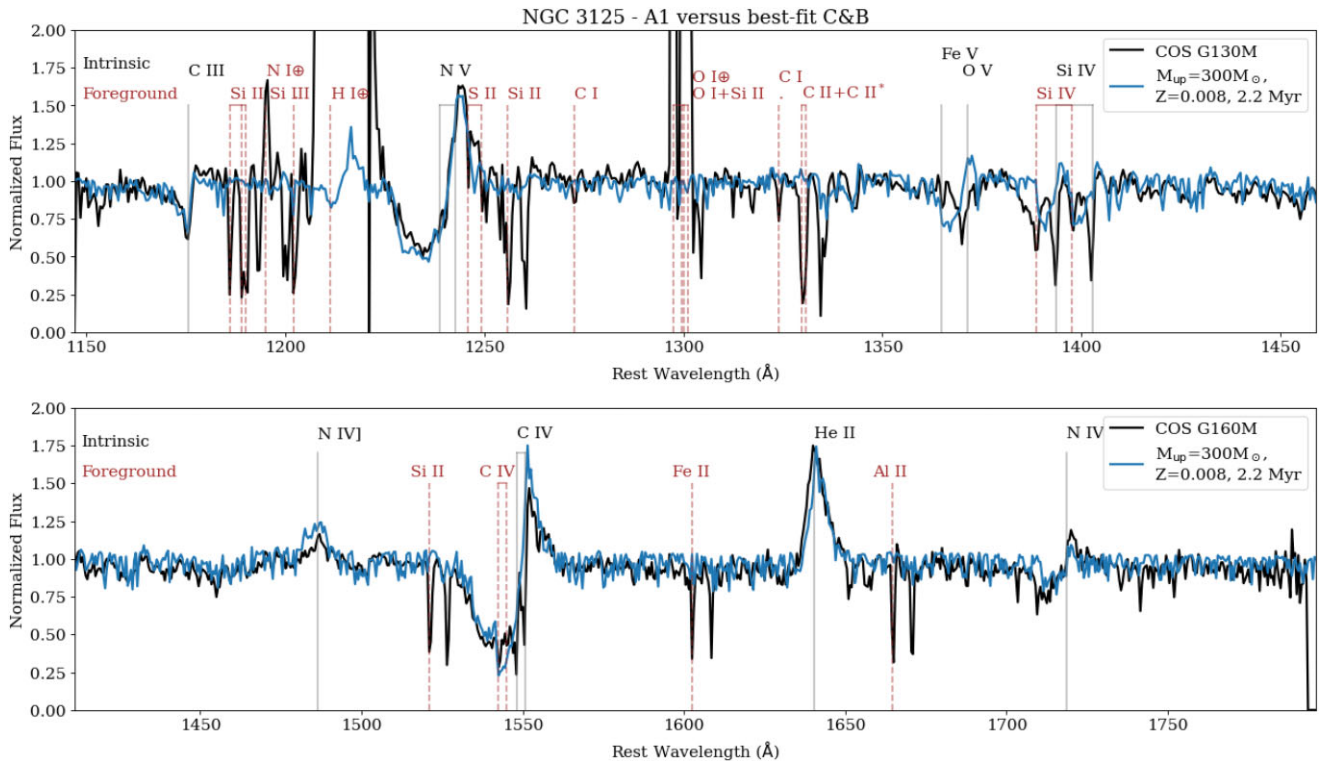


Figure 7. Comparison of CB19 model (blue curve) with COS G130M (top panel) + G160M (bottom panel) observation (black curve). We mark the positions of intrinsic and foreground lines with solid- and dashed-vertical lines, respectively, which we label with black and brown ion designations, respectively. To avoid overcrowding the plot, we do not identify the intrinsic ISM lines which are located to the right of their MW counterparts. We use the Earth's symbol to identify airglow emission lines.

the metallicity and age of the stellar population as free parameters. We do not include the reddening due to dust in the model because the comparison with the observation is done in normalized units. We try models of two metallicities that approach that of the ionized gas of NGC 3125, $Z = 0.006$ and $Z = 0.008$. For this particular application, we sample the stellar spectra in the C&B models in the UV range ($5 - 3541.4 \text{ \AA}$) every 0.1 \AA using the *SpectRes* tool provided by Carnall (2017). The total number of wavelength points in each resampled C&B spectrum is then 46 226, instead of the 16 902 points in the standard distribution (Sánchez et al. 2022, table 12).

In Fig. 4, we show corresponding predictions for the profile shape of the He II 1640 line. We show results for the above two metallicities and cases where the upper IMF mass limit, M_{up} , is equal to 100 and 300 M_\odot (hereafter, M100 and M300 models, respectively). We only show ages ranging from 1–7 Myr, as for SSPs with single stars, the He II line is expected to have an emission component at ages of < 5 Myr, when VMS and WR stars are present. The curves show the normalized luminosity. In each panel, we plot models of different ages given in Myr by the legend on the left. Each row of the figure shows predictions for different age ranges. The legends on the right give the maximum luminosity reached within each panel and its corresponding age.

Fig. 4 shows that at the two metallicities, the M300 models yield larger amplitudes of the He II line profiles, relative to the M100 models. This occurs between 2 and 3.0 Myr. In particular, the largest amplitude is reached for the combination of M300, $Z = 0.008$, and 2.2 Myr. Note that the WM-basic models dominate the P-Cygni like He II profiles when non-WR MS stars are present in the population but that the PoWR models dominate the He II emission when WR stars are present. This is illustrated in Appendix A.

4 COS OBSERVATIONS VERSUS C&B MODELS

4.1 Nebular contribution check

The *HSTACS/HRC F658N* image that is displayed in fig. 1 of W14 shows that some nebular H α emission is expected within the COS aperture. Since the models we use do not include the contribution of the ionized gas, we use the COS G160M observation to check for the presence of any nebular contribution to the He II 1640 emission line.

The top panel of Fig. 5 shows a single-component Gaussian fit (blue curve) to the normalized COS observation around the He II line (black curve). The best-fit parameters are given in the top-left legend of the panel. The emission line is broad ($FWHM = 1131 \pm 40 \text{ km s}^{-1}$), strong ($EW = 4.6 \pm 0.5 \text{ \AA}$), and redshifted by $121 \pm 17 \text{ km s}^{-1}$ in the rest-frame of the galaxy (we provide the galaxy's redshift in Table 1).

As shown in Fig. 6, after correcting the galaxy for redshift, the intrinsic ISM lines are at rest. The fact that the He II line is redshifted relative to these lines is likely because VMS dominate the He II emission, as in R136 (e.g. fig. 12 of Crowther et al. 2016), and these stars have P-Cygni like He II profiles. In the models with $Z = 0.008$ shown in Fig. 4, the predicted He II line profiles of the SSPs are P-Cygni like at ages of < 3 Myr. Thus, in the COS observation, we are likely seeing the redshifted emission component of the P-Cygni profile. The corresponding blueshifted absorption is expected to be weak and is buried in the noise.

The bottom panel of Fig. 5 shows the observation divided by the Gaussian fit to the He II line. There appears to be a decrease in the flux blueward of the He II emission peak that could be due to the P-Cygni absorption component. There is also a small flux excess on the blue side of the broad component (region marked by horizontal blue line

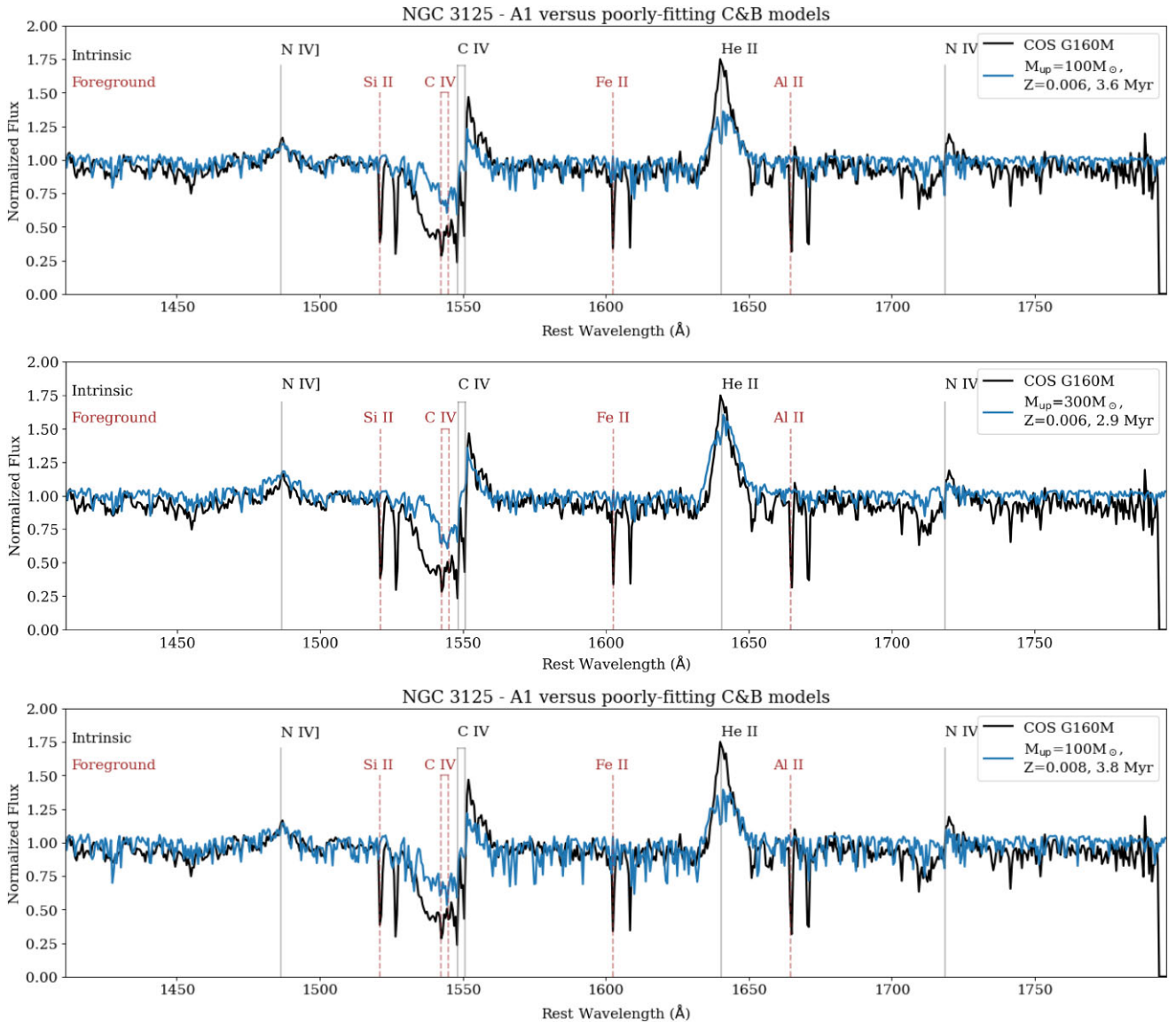


Figure 8. Similar to Fig. 7 but for the other combinations of metallicity and M_{up} that are shown in Fig. 4, at the age of maximum amplitude of the He II 1640 line. We only show the wavelength range covered by G160M. The blue and black curves are the models and observations, respectively. None of the models shown fit simultaneously the C IV and He II features. If we divide the observation by the models and consider the minimum of the stellar C IV absorption and He II emission of the models, it is between $\sim 40 - 50$ per cent and $\sim 5 - 30$ per cent too weak, respectively, relative to the observation.

in the bottom panel) at the level of ~ 10 per cent. However, the He II profile is clearly dominated by stellar-wind emission. We attribute the lack of significant nebular emission in the COS observation to the fact that there is no significant escape of He⁺-ionizing photons from the VMS stars in A1, as expected from the fact that due to their high mass-loss their winds are dense (e.g. Gräfener 2021) and absorb these photons.

The lower value of the He II EW ($\sim 5 \text{ \AA}$) relative to that previously obtained from the STIS observation ($\sim 7 \text{ \AA}$, W14) is due to the better fit to the continuum near the He II line. In particular, with the higher sensitivity and spectral resolution of COS, the weak foreground and intrinsic C I and C I* lines are detected and resolved. In the STIS observation, the fit to the continuum goes right through these lines, enhancing the line flux and hence the EW of He II.

4.2 Best-fit model

In W14, none of the models available at the time could reproduce the strength of the He II 1640 line, except for a model with an unrealistically flat IMF. Now that we have corrected the N V profile for Ly α absorption, confirmed that there is no significant nebular contamination, and normalized the spectrum, we proceed with the comparison of the observations with the model that predicts the strongest He II line, which as shown in Fig. 4, is the M300 models with $Z = 0.008$ and 2.2 Myr. The comparison of the COS observation and the C&B models is done after resampling the observation onto the model wavelength grid. We use Python’s function ‘spectres’ (Carnall 2017) for this purpose.

Fig. 7 shows the comparison between the COS G130M + G160M spectrum and the earlier model. Note that interstellar absorption

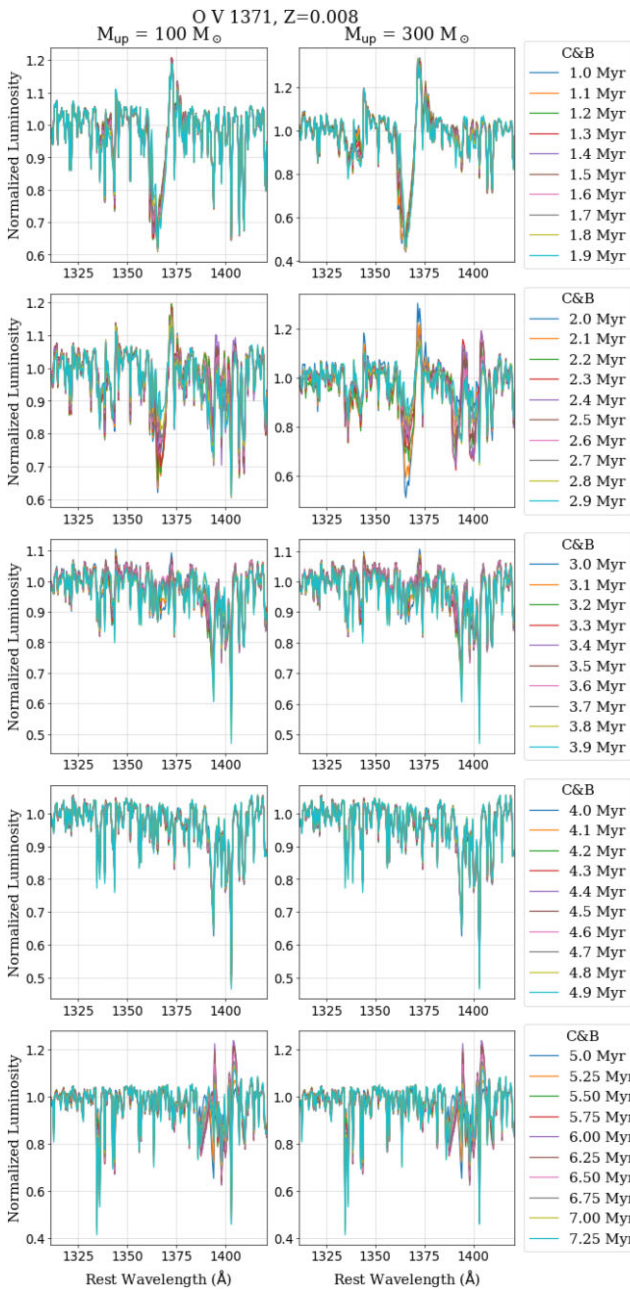


Figure 9. Similar to Fig. 4 but for O V $\lambda 1371$ and a metallicity of $Z = 0.008$. The absorption component of the line is strong at ages < 3 Myr.

lines originating in the MW and NGC 3125-A1, which are not included in the model, have not been removed from the observations. Alternatively, the model predicts a P-Cygni like Ly α profile in the region of the observation that is contaminated with geocoronal Ly α emission that fills the COS aperture.

The model is not only able to reproduce the He II 1640 line, but also provides very reasonable fits to the C III $\lambda 1175$, N V 1240, and C IV 1550 stellar-wind features. Alternatively, the optimum fit fails to reproduce both the O V 1371 line, which is indicative of youth (early O stars; e.g. Walborn, Nichols-Bohlin & Panek 1995; Crowther et al. 2016) or presence of WC stars (e.g. Grafener et al. 1998; Crowther et al. 2002); or Si IV $\lambda\lambda 1394, 1403$, which is a key indicator of evolved OB supergiants. The mismatch between the observed O V and Si IV and the best fit is likely due to failures of the theoretical

models (e.g. Garcia & Bianchi (2004) found discrepancies between WMBasic predictions and UV spectra obtained with the *International Ultraviolet Explorer*). Note that metal lines, for example, O V 1371 and N IV $\lambda 1718$ are sensitive to clumping in the stellar wind (Bouret, Lanz & Hillier 2005). Since the C&B models are based on stellar atmosphere models without wind inhomogeneities, sensitivity to clumping may explain why some of the earlier features are not as well fitted. Note that for individual stars, the clumping factor is generally used to get a consensus between UV and optical diagnostics of mass-loss. If the mass-loss rates are wrong, the line strengths of wind-affected lines will be wrong and so will be inferences from SSP models that use these lines.

For comparison, Fig. 8 shows models with other combinations of metallicity and M_{up} , at the age of maximum amplitude of the He II 1640 line, which are also shown in Fig. 4. Such models are unable to simultaneously reproduce the stellar C IV 1550 absorption and He II 1640 emission of NGC 3125-A1. In summary, the M300 model with $Z = 0.008$ and 2.2 Myr, is the best-fit model.

5 DISCUSSION

5.1 Does A1 contain VMS?

Several of the stellar-wind features that are observed in the COS spectrum of A1 are also observed in the spectra of classical WR stars. However, the presence of the O V $\lambda 1371$ absorption line in A1's spectrum suggests that this system might be too young to already have cWR stars. O V is common in early O and VMS (Crowther et al. 2016). Although note that a blend of lines including O V is used to fit the spectra of in WC stars in Aadland et al. (2022).

Fig. 9 is similar to Fig. 4 but shows C&B predictions for the O V $\lambda 1371$ line profiles corresponding to $Z = 0.008$, the metallicity of our best-fit model. The panels in the figure also include the Si IV 1400 doublet (which is strong when OB supergiants are present) and O IV $\lambda 1340$. Fig. 9 shows that indeed O V is strong in absorption at ages younger than 3 Myr. Note that the models predict that O V has a P-Cygni profile at the age of our best-fit model but that in the observation, the line is only in absorption. This could be due to problems with the atmosphere models.

For all combinations of metallicity and upper mass limit of the IMF used in this work, Fig. 10 shows the evolution of the number of massive stars of various types for a C&B SSP with an initial mass in stars of $10^5 M_{\odot}$. The WR subtypes are defined in Section 3.2 of Chen et al. (2015). Additional details are provided in appendix A1 of Plat et al. (2019). For most star types given by the legend, the number of stars should be obtained from the left axis of the figure, whereas for O-type dwarfs + supergiants, which are more numerous, they should be obtained from the right axis. In the M100 models, which are shown in the top row of the figure, the WR stars are present at ages larger than 3 and less than 5 Myr, and stars of WNL subtype are present until slightly older ages at $Z = 0.008$ relative to $Z = 0.006$. In the M300 models, the WR stars that have progenitor masses of $\geq 100 M_{\odot}$ are marked with purple squares. WR stars appear earlier in the M300 models relative to the M100 models, and in the M300 models, earlier at the highest metallicity. In particular MS WNL stars are present at 2.2 Myr in the M300 model with $Z = 0.008$, which is our preferred model.

For completeness, Fig. 10 also shows the He⁺ ionization rate, Q_{HeII} (dashed-grey curve, use right axis). Note how Q_{HeII} goes up when the WNL stars (solid-blue curve) appear, and down when cWR stars have evolved. As discussed in Sixtos et al. (2023), the increase in Q_{HeII} during the WNL, WNE, and WC phases is

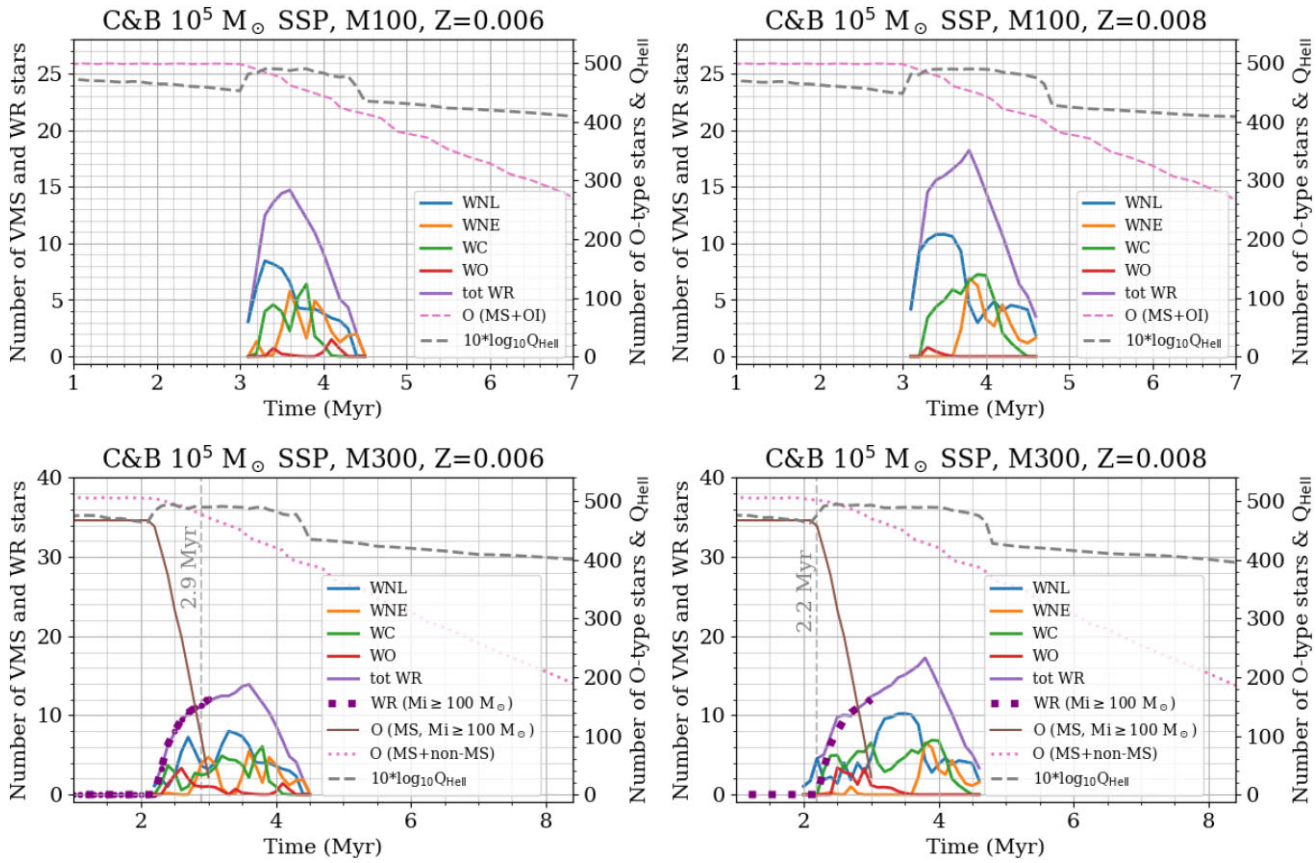


Figure 10. For C&B SSP models of total initial mass equal to 10^5 M_\odot and all combinations of metallicity and upper mass limit of the IMF, evolution of the numbers of stars of different types, as given by the legends. The different solid curves are: blue (WNL), orange (WNE), red (WO), and purple (total number of WR stars). The purple squares on top of the purple curve correspond to WR stars whose progenitors have $\geq 100 \text{ M}_\odot$. The rest of curves correspond to: MS O stars with initial masses, $M_i \geq 100 \text{ M}_\odot$ (solid-brown); and O-type stars (MS + O I; dashed-pink). We include the value of 10 times the log of the He II-ionizing photon rate, Q_{HeII} in s^{-1} (dashed-grey curve). Use the y-axis labels to know which y-axis to use. In the bottom panels, the vertical dotted lines give the ages of maximum He II 1640 emission. Note that Q_{HeII} is boosted when the WR stars are present. As explained in Sixtos et al. 2023, this is unexpected for WN and WC stars.

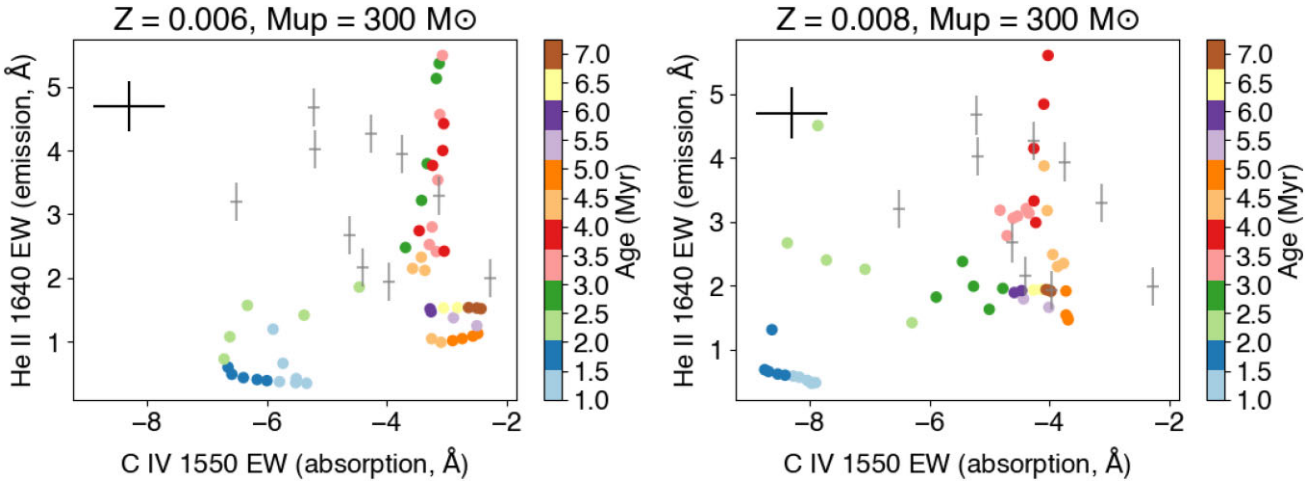


Figure 11. Similar to fig. 4 of S21 but for C&B M300 SSPs instead of constant star formation, and only for the two metallicities used in this work. The left and right panels show the results for $Z = 0.006$ and $Z = 0.008$, respectively. The black cross represents the measurement errors in A1's observed EWs and the grey crosses are the approximate errors of the observations presented in Table 5 of S21 and corresponding to a sample of nearby star-forming galaxies with metallicities down to $12 + \log(\text{O/H}) = 8.0$. The filled circles are the model predictions at the ages given by the colour bar. Only the $Z = 0.008$ model of 2.2 Myr approaches the EWs of A1. Also note the sensitivity of the C IV strength to the metallicity.

Table 3. Luminosity, mass in stars, and number of O stars for: model predictions corresponding to an SSP of $10^6 M_\odot$ (properties with ‘the’ in the sub-index); observations of NGC3125-A1; and W14.

Property	Units	This work	W14
Distance = 11.5 Mpc			
L_{1500} , the, M100	erg s^{-1}	1.9E + 39	1.54E + 39
L_{1500} , the, M300	erg s^{-1}	2.9E + 39	–
L_{1500} , obs	erg s^{-1}	5.4E + 38	2.6E + 38
M_* , obs, M100	M_\odot	2.9E + 05	1.7E + 05
M_* , obs, M300	M_\odot	1.9E + 05	–
$N(O)$, the, M100	stars	1428	2793
$N(O)$, the, M300	stars	928	–
$N(O)$, obs, M100	stars	408	467
$N(O)$, obs, M300	stars	172	–
Distance = 14.8 Mpc			
L_{1500} , obs	erg s^{-1}	9E + 38	–
M_* , obs, M300	M_\odot	3.1E + 05	–
$N(O)$, obs, M300	stars	286	–

unexpected due to the dense winds of these stars which trap the He^+ ionizing photons (Crowther & Hadfield 2006; Sander 2022). The explanation provided in Sixtos et al. (2023) is that C&B use the PoWR atmosphere grids (Todt et al. 2015), which result in a set that can yield atmospheres with and without significant He II -ionizing flux; and that the C&B population synthesis models tend to select weaker winded atmospheres that are more transparent to He II -ionizing photons. Note that this is also the case for the population synthesis code Starburst99 Russell & Dopita (1990); Leitherer et al. (2010). The extent of the emission at $<228 \text{ \AA}$ is sensitive to the theoretical definitions of WNE (no H) and WNL (some H) versus empirical (WNE: high ionization, WNL: low ionization) as well as the WNL threshold. The C&B models use the WNL PoWR atmospheres described in the appendix of Plat et al. (2019).

For a discussion on the discrepancy between predictions for the number of WR stars from population synthesis codes Starburst99 (Leitherer et al. 2010) and C&B (models used in this work) relative to observations of these stars in the LMC, see the discussion in Section 5 of Sixtos et al. (2023).

Fig. 4 of Senchyna et al. (2021, hereafter, S21) shows a plot of the strength of stellar He II emission (equivalent width, EW) versus stellar C IV absorption for a sample of extreme Wolf-Rayet (WR) galaxies and a selection of constant star formation population

synthesis models. WR galaxies are a subset of emission-line (or H II) galaxies whose integrated spectra shows broad ($FWHM \sim 10 - 20 \text{ \AA}$ or $640 - 1280 \text{ km s}^{-1}$) He II 4686 emission (Vacca & Conti 1992). In practice, the detection of a broad emission feature at $4650 - 4690 \text{ \AA}$, which is attributed to WR stars and possibly includes additional emission lines (the so-called ‘blue bump’) is often simply used (Schaerer et al. 1999). WR galaxies are distinguished spectroscopically from AGNs by their narrower Balmer lines and their forbidden line intensity ratios, which are indicative of stellar rather than non-stellar (i.e. power law) excitation.

The most extreme galaxy in the figure of S21 is not fully reproduced by the models they select. NGC 3125-A1 has a He II 1640 equivalent width and metallicity that are comparable to that of their most extreme galaxy, SB 179 (their tables 4 and 5), but a larger C IV 1550 EW. In Fig. 11, we show a plot similar to fig. 4 of S21 but for C&B SSP models at the two metallicities used in the present work. The black cross is the A1. The grey crosses are the galaxies in table 5 of S21, which span a wider range in metallicity than our model metallicites and are only plotted to demonstrate that only one galaxy in S21 approaches the EW of A1’s He II line. We use the same continuum and on-line windows for normalizing the models and observation of A1, as in S21. Also following S21, we compute the EW values of the models and observation by dividing the He II emission and C IV absorption components into rectangles (of width = 0.1 \AA , in our case) and summing the areas of the rectangles. In our case, we exclude the ISM components that contaminate the C IV lines. The figure shows how the strength of the C IV absorption depends on metallicity. Also note that only our best-fit model of 2.2 Myr approaches A1’s EWs. In summary, VMS of $Z = 0.008$ are the preferred explanation for the observed spectrum of A1.

A note could be added acknowledging that Fig. 11 is for LMC Z and some of the S21 galaxies have metallicities down to $\log \text{O/H} = 8.0$.

5.2 A1’s properties

W14 estimate the present-day mass in stars of A1 from the ratio of the STIS luminosity at 1500 \AA (corrected for reddening and redshift), to that of an SSP model with an initial mass of $10^6 M_\odot$, a Kroupa (2001) IMF, and an age of 3 Myr. For the model, they use the empirical LMC/SMC stellar library. The luminosity at 1500 \AA is from the continuum of the ensemble of stars. For the above purpose, W14 use a distance of 11.5 Mpc to A1, colour excesses due to dust in the MW

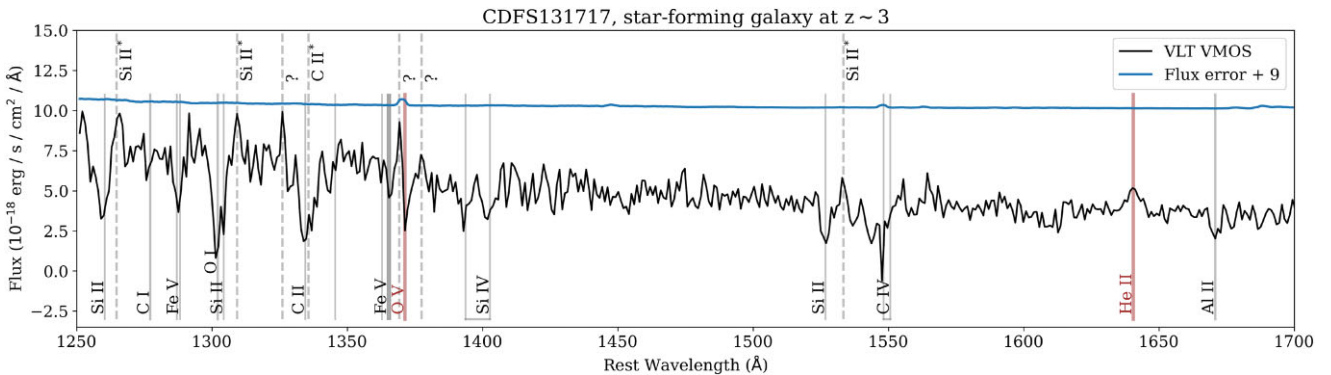


Figure 12. Reddening- and redshift-corrected VLT VMOS spectrum of $z_{\text{spec}} = 3.071$ galaxy, CDF131717 (solid-black curve), and corresponding flux errors (blue curve, offset for clarity). Based on van Hoof (2018), we mark with labelled vertical lines the positions of: the He II 1640 emission and tentative O V 1371 absorption (solid brown); fine structure lines of Si II^* (1264.73, 1309.27, and 1533.43 \AA) and C II^* (1335.71 \AA ; dashed grey), and other ISM and stellar features (solid grey).

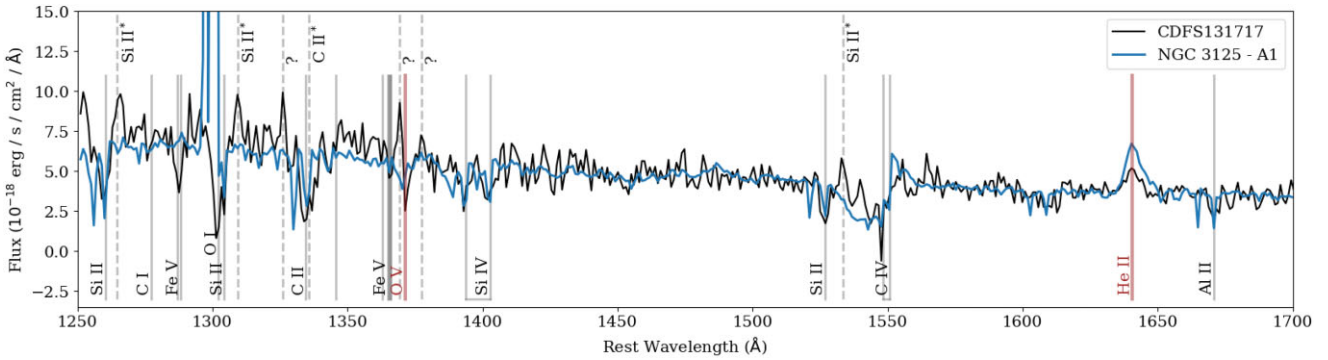


Figure 13. Comparison of the spectra of CDFS131717 (black curve) and NGC 3125-A1(blue curve). Both spectra are corrected for reddening and redshift. A1’s spectrum is degraded to the resolution of the VANDELS object and scaled to match its continuum flux at 1500 Å.

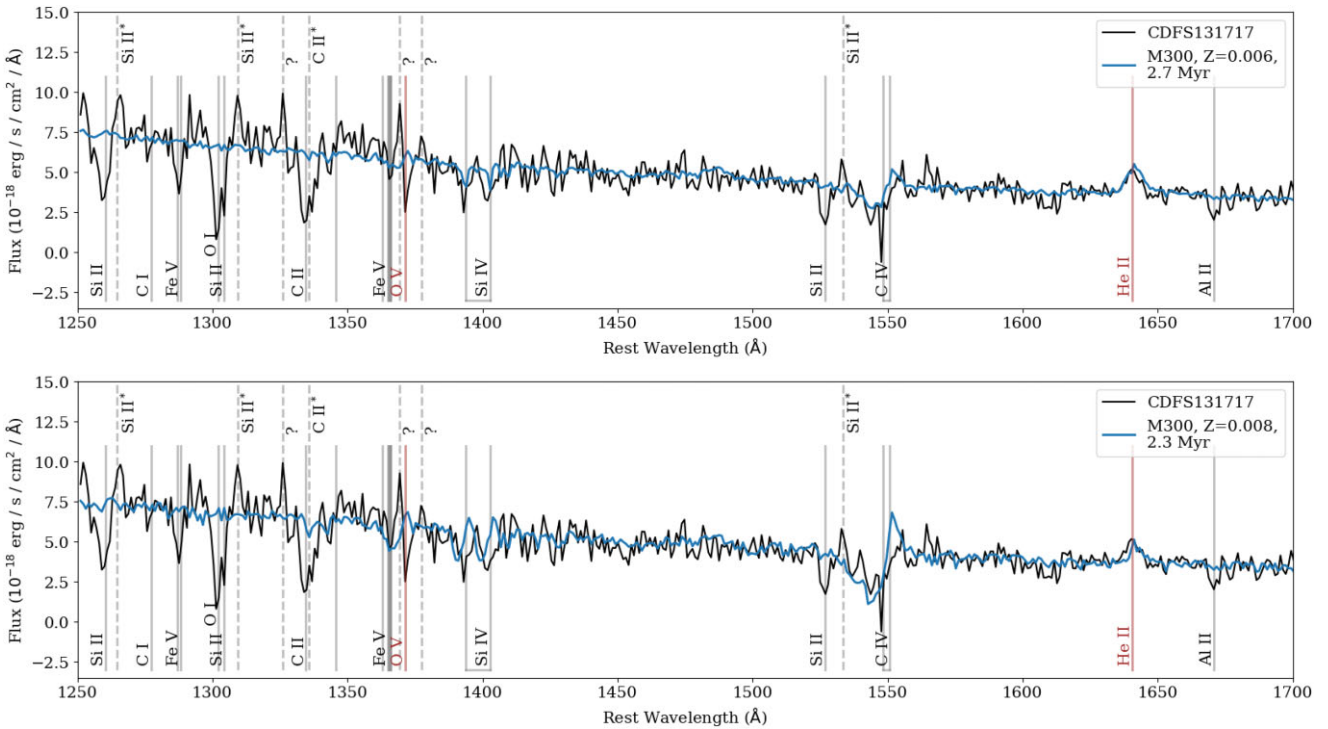


Figure 14. Similar to Fig. 13 but we compare the spectrum of CDFS131717 (black curve) to M300 models with $Z = 0.006$ and 2.7 Myr (top panel, blue curve); and $Z = 0.008$ and 2.3 Myr (bottom panel). Although the fit to the C IV and He II lines looks better in the top panel, at 2.7 Myr, the VMS are gone (see left panel of Fig. 10), whereas at 2.3 Myr (bottom panel), they are still present (see right panel of Fig. 10). However, in the bottom panel, the emission component of the predicted C IV doublet is too strong.

and A1 of 0.08 and 0.013 mag, respectively, and the extinction laws of (Fitzpatrick 1999) and (Gordon et al. 2003) for the foreground (MW) and intrinsic (A1) reddening corrections, respectively. We adopt the latter parameters to obtain in a similar way luminosities from the COS observation ($L_{1500, \text{obs}}$) and the M100 and M300 models ($L_{1500, \text{M100}}$ and $L_{1500, \text{M300}}$, respectively). For obtaining the luminosities, we use the average flux over a ± 3 Å wavelength interval around 1500 Å. In our case, the models correspond to $Z = 0.008$ and the age of highest amplitude of $\text{He II} \lambda 1640$, that is, ages of 3.8 and 2.2 Myr, respectively. To a first approximation, the present-day mass in stars of A1 is given by the luminosity ratio. The luminosities and masses from W14 and this work are given in Table 3. The masses from W14 and our M100 and M300 models are consistent with a SSC of $10^5 M_\odot$. For a distance of 11.5 Mpc, the mass corresponding to

our best-fit model is $1.9 \times 10^5 M_\odot$, whereas it is $3.1 \times 10^5 M_\odot$ when using the Virgo + GA + Shapley distance of 14.8 Mpc.

In addition, as in W14, we compute the present-day number of O stars in A1 ($N(O)$) by scaling the $N(O)$ values of our $10^6 M_\odot$ SSP M100 and M300 models by the above luminosity ratio, that is, $N(O)_{\text{obs}} = N(O)_{\text{theo}} \times (L_{1500, \text{theo}} / L_{1500, \text{obs}})$. For M100, the $N(O)$ value is smaller by 19 per cent than in W14 because the age for M100 is 3.8 Myr instead of 3 Myr for W14. For our best-fit model and a distance of 11.5 Mpc, $N(O)_{\text{obs}} = 172$, which is about a factor of three times smaller than what we found in W14. It is 286 for a distance of 14.8 Mpc.

In this work, we do not estimate the number of classical WR stars, since the presence of VMS indicates that classical WR stars have not appeared in the population yet.

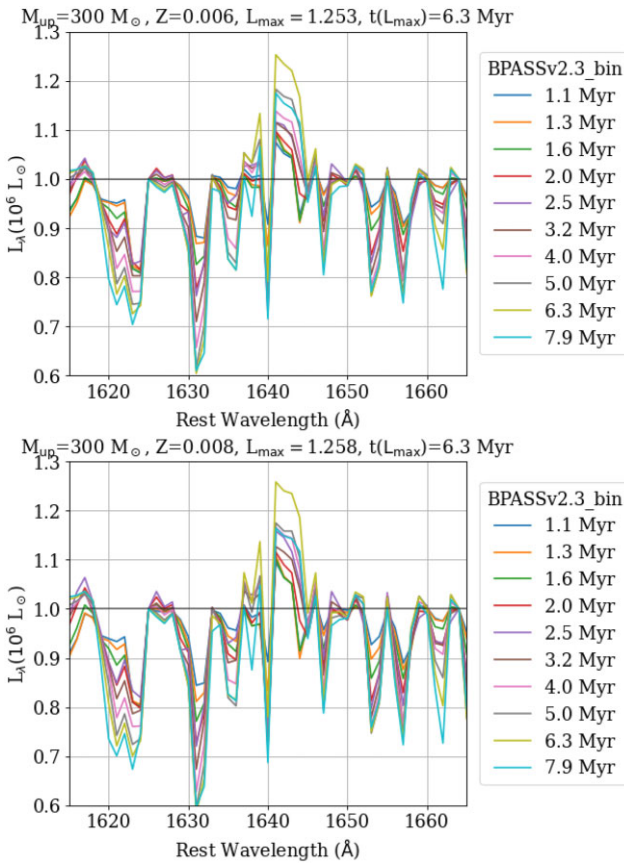


Figure 15. Evolution of He II 1640 line profiles predicted by BPASS (version 2.3) M300 SSP models with close binaries, $\Delta(\log(\alpha/\text{Fe})) = 0$, and $Z = 0.006$ (top panel) and $Z = 0.008$ (bottom panel), at the ages given by the legend. The models have a total initial mass in stars of 10^6 M_\odot . At the two metallicities, the maximum He II emission occurs at ~ 6 Myr. At ages ≥ 8 Myr, this emission is weaker.

5.3 NGC 3125-A1 versus a star-forming galaxy at $z \sim 3$

In Section 1.2, we mentioned high-redshift ($z = 3.071$) and high star-forming galaxy, CDFS131717. This galaxy has a strong ($EW = 2.5 \pm 0.1 \text{ \AA}$) broad ($FWHM \approx 920 \text{ km s}^{-1}$) He II 1640 emission line (Stanton et al. in preparation). These properties were derived from a VLT VMOS spectrum, which has a resolving power of $R = 580$, that is, a resolution of $\sim 508 \text{ km s}^{-1}$ at 6500 \AA near the observed-frame wavelength of the He II 1640 line. The reddening- and redshift-corrected spectrum of the galaxy is shown in Fig. 12. Given that the He II line is the only broad UV line of CDFS131717, this object is unlikely to be an AGN. According to a full UV-optical SED fit, the galaxy has a stellar mass of $10^{9.7} \text{ M}_\odot$ with a star-formation of $> 100 \text{ M}_\odot/\text{yr}$, making it highly star-forming for this redshift (e.g. Speagle et al. 2014). The presence of broad He II emission with $EW > 2 \text{ \AA}$ also marks it out as rare within the general star-forming population (<2 per cent of sources; Saxena et al. 2020).

Fig. 12 shows a tentative detection of O V 1371 absorption. In VMS, this absorption is expected to be blueshifted (see Fig. 9), but in CDFS131717, it appears to be at rest and next to an unidentified narrow emission line to the left of the absorption. Note that similar narrow emission lines are present at other wavelengths and correspond to Si II fluorescent emission, which is due to transitions to fine structure levels of the Si II ion. Similar lines are sometimes seen in galaxies (e.g. Wang et al. 2020). Also note that the flux error has a

slight increase near the unidentified line. In the figure, the units of the flux and flux errors are the same but the flux errors are plotted offset for clarity. If the absorption line is O V 1371, this could indicate the presence of VMS in the galaxy, particularly since it is accompanied by broad He II and strong C IV lines.

In Fig. 13, we compare the shapes of the spectra of CDFS131717 (black curve) and NGC 3125-A1(blue curve). A1's spectrum was degraded to match the resolution of the VANDELS object and scaled to match its flux in the continuum at 1500 \AA . Both spectra are corrected for reddening and redshift. An intrinsic slope of $\beta = -2.4$ (where $F_\lambda \propto \lambda^\beta$) was assumed for the continuum of CDFS131717. The O V absorptions almost coincide. On the other hand, the He II line of CDFS131717 is weaker. Note, however, that we are comparing a SSC (A1) to an entire galaxy, which has an underlying stellar continuum that is not present in A1.

In Fig. 14, we compare the spectrum of CDFS131717 to M300 models (given the tentative detection of O V absorption). The lowest metallicity model (top panel, blue curve) seems to provide a reasonable fit to the stellar C IV 1550 and He II 1640 features (the narrow C IV ISM components of the observation are not accounted for in the model); but this model has weak O V in absorption. The highest metallicity model (bottom panel) approximately fits the He II line but produces too much C IV 1550 in emission. However, the latter model has stronger O V 1371 in absorption. A fit to the galaxy with a more realistic (non-SSP) model is beyond the scope of our paper but will be presented in a more comprehensive study of CDFS131717 that also includes optical constraints (Stanton et al. in preparation). However, we note here that the tentative detection of O V absorption, clear detection of strong and broad He II emission, and rarity of high-redshift objects with similar He II line properties are all hints that short-lived VMS might be present in CDFS131717.

5.4 Binaries

There is now evidence that most massive stars are in close binary systems where the stars exchange mass and rotate, which affects their evolution relative to models where massive stars evolve as single non-rotating objects (Sana et al. 2012). Fig. 4 shows that the 1640 emission fades after 5 Myr owing to the lack of WR stars from single stars beyond this age, but binaries will prolong the WR phase, as predicted by the work of Götberg et al. 2018 and observed by Beasor et al. 2021, who favour an age of approximately 10 Myr for Galactic cluster Westerlund 1, which is host to dozens of WR stars.

The importance of including binaries in massive-star population studies is discussed in the review by Eldridge & Stanway (2022). Several efforts have been carried out to determine the initial binary fraction, period distribution, and mass ratios of these stars (e.g. Sana et al. 2012). The effects of binaries are currently implemented in some spectral synthesis codes, for example, BPASS (Eldridge et al. 2017) and the models of Götberg et al. (2019).

The latest version of publicly available BPASS models (version 2.3) are presented in (Byrne et al. 2022). In Fig. 15, we show BPASS v. 2.3 He II 1640 line-profile predictions for M300 SSP populations with close binaries at the metallicities used in this work. We plot BPASS models with a standard mass ratio of α -elements to iron, at all ages available between ~ 1 and ~ 8 Myr. At older ages, the strength of He II does not increase. In addition, BPASS models with the same total metallicity, Z , but in which mass ratio of α -elements to iron has been modified by $\Delta(\log(\alpha/\text{Fe}))$ do not significantly

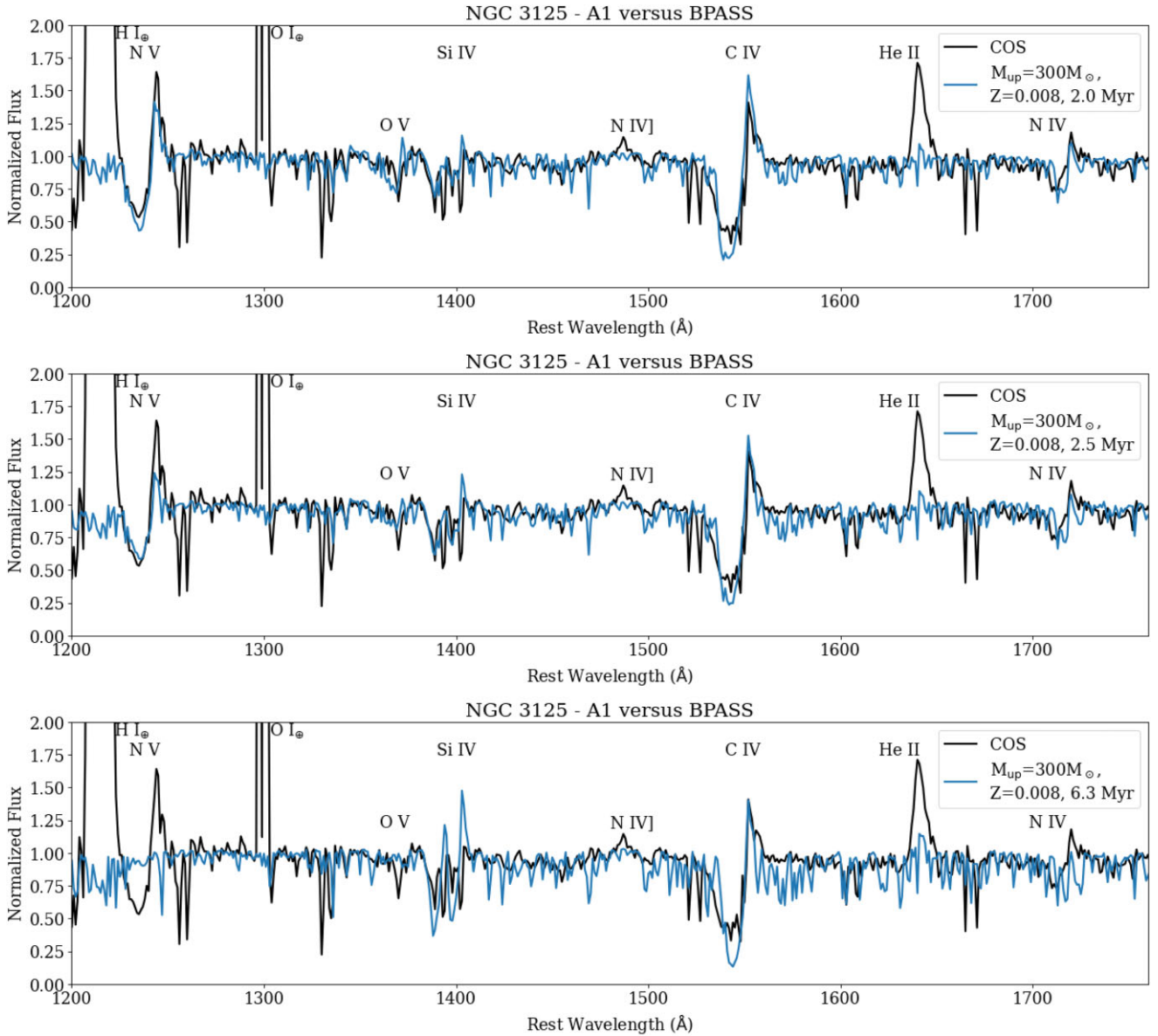


Figure 16. Comparison of BPASS M300 SSP models having close binaries and $Z = 0.008$ (blue curves), with A1’s observation degraded to the model’s resolution and normalized (black curve). We show model at the ages given by the legend. The bottom panel is the case of maximum He II emission.

change the strength of the He II profile. At the two metallicities shown in Fig. 15, the maximum strength of He II is reached at 6.3 Myr. Thus, binary models boost 1640 emission at higher ages with respect to single stars. In addition, at 6.3 Myr, the emission is slightly stronger for $Z = 0.008$. On the other hand, the maximum He II line strength is significantly less than that of A1. This can be seen in Fig. 16, where we compare BPASS models with $Z = 0.008$ and different ages given by the legend. Ages 2.0 and 2.5 Myr are the closest available ages in BPASS to our best-fit C&B model, which corresponds to 2.2 Myr. According to BPASS author J.J. Eldridge (private communication) some of the reasons that could explain the BPASS prediction for He II 1640 are the following. At $Z = 0.008$ the absorption lines in cooler stars start to get significant and decrease the strength of the He II, as seen in Fig. 15. In addition, there are fewer VMS in the BPASS models at this metallicity because the models start having mass-loss rates that are high enough to reduce the mass of VMS to more normal masses. Thus, the models

have fewer stars near the Eddington limit so weaker He II. Finally, the BPASS models do not include accretion-disc emission around stellar black holes and neutron stars, which might boost the He II emission. Going back to Fig. 16, also note that for none of the ages shown do the N v 1240 and C IV 1550 features fit simultaneously. In summary, although BPASS models currently fail to reproduce strong stellar He II emission, population synthesis models should allow for modern mass-loss prescriptions, rotational mixing, and close binary evolution.

6 SUMMARY AND CONCLUSIONS

In this paper, we present unpublished COS G160M observations of SSC NGC 3125-A1 that we analyse in combination with archival G130M spectra of the object. We focus on the modelling of the extreme He II emission of the SSC, which had represented a challenge

for population synthesis models until recently Martins & Palacios (2022).

(i) We determine that the He II line has a negligible contribution from nebular gas, is broad ($FWHM = 1131 \pm 40 \text{ km s}^{-1}$), strong ($EW = 4.6 \pm 0.5 \text{ \AA}$), and redshifted by $121 \pm 17 \text{ km s}^{-1}$ relative to ISM lines (Fig. 5). The broad line is the strongest ever detected in the nearby universe, only comparable to one of the objects in the sample of nearby galaxies with broad He II emission that is analysed in S21.

(ii) Although BPASS version 2.3 (Byrne et al. 2022) models with close binaries currently fail to reproduce strong stellar He II emission (Figs 15 and 16), it is clear that population synthesis models should allow for close binary evolution (Section 5.4).

(iii) Alternatively, a C&B (Plat et al. 2019) SSP with single non-rotating stars, a metallicity of $Z = 0.008$, and an age of 2.2 Myr, where MS WR stars close to the Eddington limit are present, provides a very good fit to the He II line and other massive-star features in the wavelength range $\sim 1150 - 1750 \text{ \AA}$ (Figs 7 and 11).

(iv) We show that the presence of blueshifted O V $\lambda 1371$ absorption in the spectrum of a massive-star population provides an important clue of the youth of the population and possible presence of VMS (Fig. 9).

We also present the spectrum of the broad-HeII emitter, CDFS131717, which is an unlensed strongly star-forming, low-metallicity galaxy located at $z \sim 3.071$ (Fig. 14). The tentative detection of O V absorption in the spectrum, clear detection of strong and broad He II emission, and rarity of the objects with similar properties at high- z are all hints that short-lived VMS might be present in CDFS131717. A more detailed analysis of this galaxy accounting for the underlying stellar population and including constraints from the optical will be presented in Stanton et al. (in preparation). Overall, our results show the effect of the improved formulation of stellar mass-loss rates. In conclusion, population synthesis models should include binaries, VMS, modern mass-loss prescriptions, and rotational mixing.

ACKNOWLEDGEMENTS

Based on observations made with the NASA/ESA *Hubble Space Telescope*, at the Space Telescope Science Institute, which is operated by the Association of Universities for Research in Astronomy, Inc., under NASA contract number NAS5-26555. These observations are associated with programs #12172 and #15828.

AW and AS acknowledge financial support from grant number DGAPA/UNAM PAPIIT IN106922 (PI Wofford). GB acknowledges financial support from UNAM grants DGAPA/PAPIIT IG100319 and BG100622. FC and TMS acknowledge support from a UKRI Frontier Research Guarantee Grant (PI Cullen; grant reference EP/X021025/1).

We thank the referee for very helpful comments that improved the quality of this work. We also thank J. Vink for pointing out that H-rich VMS have WR features, independent of He enrichment; P. Crowther and T. Shenar, who helped clarify why VMS and not classical WR stars are the main contributors to the UV spectrum of A1; J. C. Bouret and A. Sander, for helpful discussions about the use of the clumping factor in massive-star wind models; and E. Stanway and J.J. Eldridge for providing explanations for the weaker He II emission predicted by the BPASS models at $Z = 0.008$.

7 DATA AVAILABILITY

The *HST* COS observations from PIDs 12 172 and 15 828 used in this work are available through the Barbara A. MAST at <https://mast.stsci.edu/search/ui/#/>. The VANDELS spectrum used in this work is publicly available and can be accessed via the ESO science portal (<http://archive.eso.org/scienceportal/home>).

REFERENCES

- Aadland E., Massey P., Hillier D. J., Morrell N., 2022, *ApJ*, 924, L44
 Adamo A., et al., 2020, *Space Sci. Rev.*, 216, 69
 Amard L., Palacios A., Charbonnel C., Gallet F., Georgy C., Lagarde N., Siess L., 2019, *A&A*, 631, 77
 Amorín R., et al., 2017, *Nat. Astron.*, 1, 0052
 Andersen M., Zinnecker H., Moneti A., McCaughrean M. J., Brandl B., Brandner W., Meylan G., Hunter D., 2009, *ApJ*, 707, L1347
 Beasor E. R., Davies B., Smith N., Gehrz R. D., Figer D. F., 2021, *ApJ*, 912, L16
 Bestenlehner J. M., et al., 2020, *MNRAS*, 499, 1918
 Bosch G., Terlevich E., Terlevich R., 2009, *AJ*, 137, 3437
 Bouret J. C., Lanz T., Hillier D. J., 2005, *A&A*, 438, 301
 Brands S. A., et al., 2022, *A&A*, 663, 36
 Brinchmann J., Charlot S., White S. D. M., Tremonti C., Kauffmann G., Heckman T., Brinkmann J., 2004, *MNRAS*, 351, 1151
 Byrne C. M., Stanway E. R., Eldridge J. J., McSwiney L., Townsend O. T., 2022, *MNRAS*, 512, 5329
 Carnall A. C., 2017, preprint ([arXiv:1705.05165](https://arxiv.org/abs/1705.05165))
 Chandar R., Leitherer C., Tremonti C. A., 2004, *ApJ*, 604, L153
 Chen Y., Bressan A., Girardi L., Marigo P., Kong X., Lanza A., 2015, *MNRAS*, 452, 1068
 Crowther P. A., Hadfield L. J., 2006, *A&A*, 449, 711
 Crowther P. A., Dessart L., Hillier D. J., Abbott J. B., Fullerton A. W., 2002, *A&A*, 392, 653
 Crowther P. A., Schnurr O., Hirschi R., Yusof N., Parker R. J., Goodwin S. P., Kassim H. A., 2010, *MNRAS*, 408, 731
 Crowther P. A., et al., 2016, *MNRAS*, 458, 624
 Cullen F., et al., 2019, *MNRAS*, 487, 2038
 Cullen F., et al., 2021, *MNRAS*, 505, 903
 Danforth C. W., Keeney B. A., Stocke J. T., Shull J. M., Yao Y., 2010, *ApJ*, 720, L976
 Eldridge J. J., Stanway E. R., 2022, *ARA&A*, 60, 455
 Eldridge J. J., Stanway E. R., Xiao L., McClelland L. A. S., Taylor G., Ng M., Greis S. M. L., Bray J. C., 2017, *PASA*, 34, e058
 Erb D. K., Pettini M., Shapley A. E., Steidel C. C., Law D. R., Reddy N. A., 2010, *ApJ*, 719, L1168
 Fitzpatrick E. L., 1999, *PASP*, 111, 63
 Förster Schreiber N. M., Wuyts S., 2020, *ARA&A*, 58, 661
 Garcia M., Bianchi L., 2004, *ApJ*, 606, L497
 Garilli B., et al., 2021, *A&A*, 647, 150
 Gordon K. D., Clayton G. C., Misselt K. A., Landolt A. U., Wolff M. J., 2003, *ApJ*, 594, L279
 Götzberg Y., de Mink S. E., Groh J. H., Kupfer T., Crowther P. A., Zapartas E., Renzo M., 2018, *A&A*, 615, 78
 Götzberg Y., de Mink S. E., Groh J. H., Leitherer C., Norman C., 2019, *A&A*, 629, 134
 Gräfener G., 2021, *A&A*, 647, 13
 Graefener G., Hamann W. R., Hillier D. J., Koesterke L., 1998, *A&A*, 329, 190
 Gutkin J., Charlot S., Bruzual G., 2016, *MNRAS*, 462, 1757
 Hadfield L. J., Crowther P. A., 2006, *MNRAS*, 368, 1822
 Hénault-Brunet V., et al., 2012, *A&A*, 546, 73
 Hernandez S., Aloisi A., James B. L., Ferland G. J., Fox A. J., Tosi M., Tumlinson J., 2020, *ApJ*, 892, L19
 Hernandez S., et al., 2021, *ApJ*, 908, L226
 Hillier D. J., Miller D. L., 1998, *ApJ*, 496, L407
 James B. L., 2022, in COS Instrument Handbook, ver. 14. STScI, Baltimore, p. 14

- Johnson K. E., 2001, PhD thesis, University of Colorado, Boulder
- Kalari V. M., Horch E. P., Salinas R., Vink J. S., Andersen M., Bestenlehner J. M., Rubio M., 2022, *ApJ*, 935, L162
- Krogager J.-K., 2018, preprint ([arXiv:1803.01187](https://arxiv.org/abs/1803.01187))
- Kroupa P., 2001, *MNRAS*, 322, 231
- Kunth D., Sargent W. L. W., 1981, *A&A*, 101, 5
- Lagarde N., Decressin T., Charbonnel C., Eggenberger P., Ekström S., Palacios A., 2012, *A&A*, 543, 108
- Lanz T., Hubeny I., 2003, *ApJS*, 146, 417
- Lanz T., Hubeny I., 2007, *ApJS*, 169, 83
- Leitherer C., et al., 1999, *ApJS*, 123, 3
- Leitherer C., Leão J. R. S., Heckman T. M., Lennon D. J., Pettini M., Robert C., 2001, *ApJ*, 550, L724
- Leitherer C., Ortiz Otálvaro P. A., Bresolin F., Kudritzki R.-P., Lo Faro B., Pauldrach A. W. A., Pettini M., Rix S. A., 2010, *ApJS*, 189, 309
- Leitherer C., Tremonti C. A., Heckman T. M., Calzetti D., 2011, *AJ*, 141, 37
- Leitherer C., Ekström S., Meynet G., Schaerer D., Agienko K. B., Levesque E. M., 2014, *ApJS*, 212, 14
- Leitherer C., Byler N., Lee J. C., Levesque E. M., 2018, *ApJ*, 865, L55
- Martins F., Palacios A., 2022, *A&A*, 659, 163
- McLure R. J., et al., 2018, *MNRAS*, 479, 25
- Mould J. R., et al., 2000, *ApJ*, 529, L786
- Pauldrach A. W. A., Hoffmann T. L., Lennon M., 2001, *A&A*, 375, 161
- Pettini M., Steidel C. C., Adelberger K. L., Dickinson M., Giavalisco M., 2000, *ApJ*, 528, L96
- Plat A., Charlot S., Bruzual G., Feltre A., Vidal-García A., Morisset C., Chevallard J., Todt H., 2019, *MNRAS*, 490, 978
- Rivera-Thorsen T. E., et al., 2019, *Science*, 366, 738
- Russell S. C., Dopita M. A., 1990, *ApJS*, 74, 93
- Sana H., et al., 2012, *Science*, 337, 444
- Sánchez S. F., et al., 2022, *ApJS*, 262, 36
- Sander A. A. C., 2022, preprint ([arXiv:2211.05424](https://arxiv.org/abs/2211.05424))
- Sanders R. L., et al., 2021, *ApJ*, 914, L19
- Saxena A., et al., 2020, *A&A*, 636, 47
- Schaerer D., Contini T., Kunth D., 1999, *A&A*, 341, 399
- Senchyna P., Stark D. P., Charlot S., Chevallard J., Bruzual G., Vidal-García A., 2021, *MNRAS*, 503, 6112
- Shapley A. E., Steidel C. C., Pettini M., Adelberger K. L., 2003, *ApJ*, 588, L65
- Siess L., Dufour E., Forestini M., 2000, *A&A*, 358, 593
- Sirressi M., et al., 2022, *AJ*, 164, 208
- Sixtos A., Wofford A., Sander A. A. C., Peimbert A., 2023, *MNRAS*, 519, 5656
- Smith N., Conti P. S., 2008, *ApJ*, 679, L1467
- Smith L. J., Crowther P. A., Calzetti D., Sidoli F., 2016, *ApJ*, 823, L38
- Soderblom D. R., 2021, in COS Data Handbook, Vol. 5. p. 5
- Speagle J. S., Steinhardt C. L., Capak P. L., Silverman J. D., 2014, *ApJS*, 214, 15
- Steidel C. C., Strom A. L., Pettini M., Rudie G. C., Reddy N. A., Trainor R. F., 2016, *ApJ*, 826, L159
- Todt H., Sander A., Hainich R., Hamann W. R., Quade M., Shenar T., 2015, *A&A*, 579, 75
- Toribio San Cipriano L., Domínguez-Guzmán G., Esteban C., García-Rojas J., Mesa-Delgado A., Bresolin F., Rodríguez M., Simón-Díaz S., 2017, *MNRAS*, 467, 3759
- Vacca W. D., Conti P. S., 1992, *ApJ*, 401, L543
- Vanzella E., et al., 2020, *MNRAS*, 499, L67
- Vink J. S., Muijres L. E., Anthonisse B., de Koter A., Gräfener G., Langer N., 2011, *A&A*, 531, 132
- Vink J. S., et al., 2015, Proc. IAU 10, Very Massive Stars in the Local Universe. Cambridge Univ. Press, p. 51
- van Hoof P. A. M., 2018, *Galaxies*, 6, 63
- Walborn N. R., Nichols-Bohlin J., Panek R. J., 1995, VizieR Online Data Catalog, p. III/115
- Wang B., Heckman T. M., Zhu G., Norman C. A., 2020, *ApJ*, 894, L149

APPENDIX A: WM-BASIC AND POWR CONTRIBUTIONS

In Fig. A1, we show the effect on the final SED of not using the WM-Basic models, i.e. of using plane parallel TLUSTY models with no stellar wind + PoWR models (red curves). The blue curves include Tlusty + WM-Basic + PoWR models. The top and bottom rows show different wavelength ranges. The figure illustrates that WM-Basic models dominate the P-Cygni like He II 1640 profile of the population when no WR stars of any kind are present. This can be seen in the bottom-left panel, which corresponds to a C&B M300 SSP of $Z = 0.006$ and 2.2 Myr. On the other hand, the bottom-right panel of the figure, which corresponds to a similar model but with $Z = 0.008$, shows that the He II 1640 emission is dominated by the PoWR models. This is because at this metallicity, MS WR stars have already appeared at the same age, and in C&B models, WR stars are modelled with PoWR. All this is in agreement with what is shown in the bottom panels of Fig. 10, where the number of WNL stars as a function of time is plotted at the above two metallicities. At both metallicities, Fig. A1 shows that WM-Basic models dominate the N V 1240 and C V 1550 P-Cygni profiles, which are due to the presence of O MS stars. Note that the model in blue shown in the bottom-right panel of Fig. A1 is the one that best fits the COS observations of NGC 3125-A1.

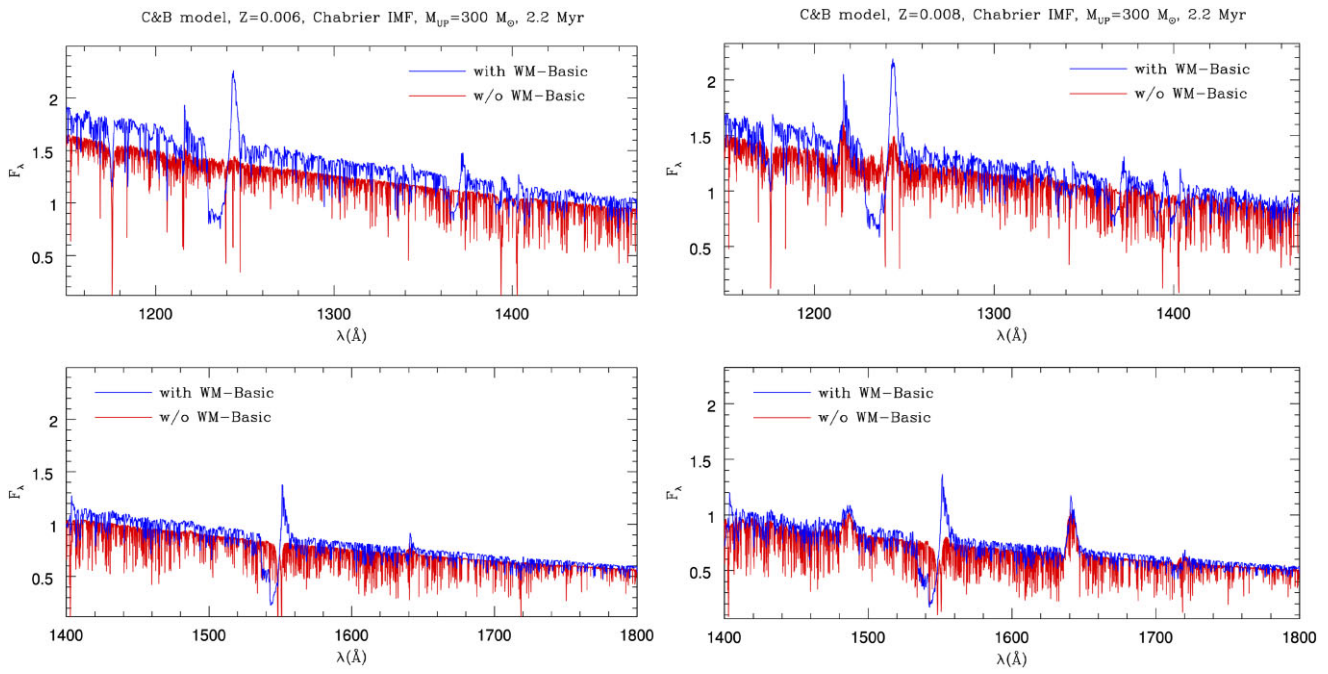


Figure A1. Left – difference in C&B M300 SSP spectrum of $Z = 0.006$ and 2.2 Myr, with (blue curve) and without (red-curve) the contribution of the WM-Basic models. The top and bottom rows show different wavelength ranges. At 2.2 Myr and $Z = 0.006$, there are no WR stars of any kind and a He II 1640 P-Cygni like profile is only present when the WM-Basic models are included. Right – Similar but for $Z = 0.008$. At this metallicity, there are MS WR stars present. This is why in the bottom-right panel the He II 1640 emission is dominated by the PoWR models.

This paper has been typeset from a $\text{\TeX}/\text{\LaTeX}$ file prepared by the author.

I. Conclusiones generales

Realizamos dos estudios de la emisión de He II en el óptico (λ 4686) y UV (λ 1640) en dos diferentes objetos, HD 5980 en el óptico y NGC 3125-A1 en el UV. Para el primer trabajo, utilizamos observaciones obtenidas con FORS1 en el *VLT* para buscar emisión nebulosa de He II λ 4686 al sur del sistema múltiple HD 5980. Encontramos solo una componente ancha de He II λ 4686, extendida hasta \sim 7.6 pc del sistema. Realizamos una comparación con observaciones obtenidas con STIS en el *HST*, con una fase orbital similar a nuestras observaciones, mostrando así que la emisión ancha de He II es una probable contaminación del sistema múltiple HD 5980. Adicionalmente, utilizamos modelos de atmósferas estelares para mostrar que no se espera un flujo de He⁺ ionizante significativo de las estrellas WN de HD 5980 y que cuando estrellas similares están presentes en una población estelar coetánea, las estrellas O podrían ser las mayores emisoras de radiación ionizante de He⁺ solo comparado con estrellas WN, pero no al nivel de una galaxia.

Para el segundo trabajo utilizamos observaciones COS G160M obtenidas con el *HST* del SSC NGC 3125-A1 no publicadas, junto a observaciones anteriores tomadas con COS G130M, enfocándonos en modelar la emisión de He II extrema de A1. Observamos una emisión ancha de la línea de He II λ 1640 ($FWHM = 1131 \pm 40 \text{ km s}^{-1}$), intensa ($EW = 4.6 \pm 0.5 \text{ \AA}$) y corrida al rojo $121 \pm 17 \text{ km s}^{-1}$ con respecto a las líneas del medio interestelar. Esta línea ancha es la más intensa jamás detectada en el Universo cercano, solo comparable con uno de los objetos de la muestra de galaxias cercanas con emisión de He II ancha que analizaron en Senchyna et al. (2021). Se observó que los modelos BPASS (versión 2.3, Eldridge et al., 2017; Byrne et al., 2022), no logran reproducir la emisión estelar de He II aún incluyendo evolución de binarias con intercambio de materia. Por otro lado, usando modelos de C&B (Plat et al., 2019) con estrellas individuales no rotantes, se encontró que para una metalicidad de $Z = 0.008$, y una edad de 2.2 Myr, donde se cuenta con estrellas VMS cerca del límite de Eddington, se obtiene un buen ajuste de la linea de He II y otras líneas espectrales características de estrellas masivas en el rango de longitud de onda entre 1150-1750\AA. En este trabajo también se muestra que la presencia de la línea de absorción O v λ 1371, corrida al azul en el espectro de una población de estrellas masivas, proporciona una importante pista de la juventud de la población y la posible presencia de VMS. Por último, analizamos la presencia de VMS en CDFS131717, una galaxia de baja metalicidad con gran actividad de formación estelar situada a $z = 3.071$. En su conjunto, nuestros artículos muestran dos desafíos a los que aún se enfrentan los modelos de síntesis de poblaciones estelares más usados: la correcta predicción de la tasa de fotones ionizantes de He II y la correcta predicción del perfil de la emisión de He II formada en el viento estelar que hasta ahora se ha logrado con éxito pero sin binarias. Por otra parte, nuestro trabajo discute la importancia de incluir la binariedad, las VMS, los últimos avances en la teoría de los vientos de las estrellas masivas y la rotación en los modelos de síntesis de poblaciones modernos.

Bibliografía

Abbott B. P., et al., 2019, , 875, 122

Abbott R., et al., 2020, , 896, L44

Abbott R., et al., 2021, , 915, L5

Agrawal P., 2021, in Hypatia Colloquium 2021: Early Career Astronomer series at ESO. p. 17, doi:10.5281/zenodo.5607416

Alarie A., Morisset C., 2019, , 55, 377

Bestenlehner J. M., et al., 2020, , 499, 1918

Bressan A., Marigo P., Girardi L., Salasnich B., Dal Cero C., Rubele S., Nanni A., 2012, , 427, 127

Broekgaarden F. S., et al., 2022, , 516, 5737

Brown T. M., Heap S. R., Hubeny I., Lanz T., Lindler D., 2002, , 579, L75

Brown T. M., et al., 2014, , 796, 91

Bruzual G., Charlot S., 2003, , 344, 1000

Bruzual-A. G., 1983, , 8, 63

Byrne C. M., Stanway E. R., Eldridge J. J., McSwiney L., Townsend O. T., 2022, , 512, 5329

Chabrier G., 2003, , 115, 763

Chen Y., Bressan A., Girardi L., Marigo P., Kong X., Lanza A., 2015, , 452, 1068

Chiappini C., Matteucci F., Meynet G., 2006, in , Chemical Abundances and Mixing in Stars in the Milky Way and its Satellites. p. 371, doi:10.1007/978-3-540-34136-9_115

Cordier D., Pietrinferni A., Cassisi S., Salaris M., 2007, , 133, 468

Crowther P. A., 2007, , 45, 177

Crowther P. A., Hadfield L. J., 2006, , 449, 711

Crowther P. A., Schnurr O., Hirschi R., Yusof N., Parker R. J., Goodwin S. P., Kassim H. A., 2010, , 408, 731

Crowther P. A., et al., 2016, , 458, 624

Dessart L., Hillier D. J., Li C., Woosley S., 2012, , 424, 2139

Doran E. I., et al., 2013, , 558, A134

- Dotter A., 2016, , 222, 8
- Driessen L., Moffat A. F. J., Walborn N. R., Shara M. M., 1995, , 110, 2235
- Dufton P. L., Evans C. J., Hunter I., Lennon D. J., Schneider F. R. N., 2019, , 626, A50
- Eggenberger P., et al., 2021, , 652, A137
- Ekström S., et al., 2012, , 537, A146
- Eldridge J. J., Stanway E. R., 2012, , 419, 479
- Eldridge J. J., Stanway E. R., Xiao L., McClelland L. A. S., Taylor G., Ng M., Greis S. M. L., Bray J. C., 2017, , 34, e058
- Faber S. M., 1972, , 20, 361
- Feltre A., Charlot S., Gutkin J., 2016, , 456, 3354
- Gal-Yam A., Leonard D. C., 2009, , 458, 865
- Garcia M., et al., 2019, arXiv e-prints, p. arXiv:1908.04687
- Georgy C., Ekström S., Meynet G., Massey P., Levesque E. M., Hirschi R., Eggenberger P., Maeder A., 2012, , 542, A29
- Georgy C., et al., 2013, , 558, A103
- Gómez-González V. M. A., Mayya Y. D., Toalá J. A., Arthur S. J., Zaragoza-Cardiel J., Guerrero M. A., 2021, , 500, 2076
- Götberg Y., de Mink S. E., Groh J. H., 2017, , 608, A11
- Götberg Y., de Mink S. E., Groh J. H., Kupfer T., Crowther P. A., Zapartas E., Renzo M., 2018, , 615, A78
- Hadfield L. J., Crowther P. A., 2006, , 368, 1822
- Hainich R., Pasemann D., Todt H., Shenar T., Sand er A., Hamann W. R., 2015, , 581, A21
- Hillier D. J., Koenigsberger G., Nazé Y., Morrell N., Barbá R. H., Gamen R., 2019, , 486, 725
- Hirschi R., Meynet G., Maeder A., Ekström S., Georgy C., 2010, in Leitherer C., Bennett P. D., Morris P. W., Van Loon J. T., eds, Astronomical Society of the Pacific Conference Series Vol. 425, Hot and Cool: Bridging Gaps in Massive Star Evolution. p. 13
- Izotov Y. I., Schaerer D., Blecha A., Royer F., Guseva N. G., North P., 2006, , 459, 71
- Kehrig C., Guerrero M. A., Vilchez J. M., Ramos-Larios G., 2021, , 908, L54
- Kotak R., Vink J. S., 2006, , 460, L5
- Kroupa P., 2001, , 322, 231
- Lamers H. J. G. L. M., Maeder A., Schmutz W., Cassinelli J. P., 1991, , 368, 538
- Legrand F., Kunth D., Roy J. R., Mas-Hesse J. M., Walsh J. R., 1997, , 326, L17
- Leitherer C., et al., 1999, , 123, 3

- Leitherer C., Ortiz Otálvaro P. A., Bresolin F., Kudritzki R.-P., Lo Faro B., Pauldrach A. W. A., Pettini M., Rix S. A., 2010, , 189, 309
- Leitherer C., Byler N., Lee J. C., Levesque E. M., 2018, , 865, 55
- Leitherer C., Lee J. C., Faisst A., 2019, , 158, 192
- Levesque E. M., Leitherer C., Ekstrom S., Meynet G., Schaerer D., 2012, , 751, 67
- López-Sánchez Á. R., Esteban C., 2010, , 516, A104
- Madau P., Dickinson M., 2014, , 52, 415
- Maeder A., Meynet G., 1994, , 287, 803
- Maiolino R., et al., 2023, arXiv e-prints, p. arXiv:2306.00953
- Maraston C., 2005, , 362, 799
- Martins F., Schaerer D., Marques-Chaves R., Upadhyaya A., 2023, arXiv e-prints, p. arXiv:2308.14489
- Massey P., 2003, , 41, 15
- Massey P., Duffy A. S., 2001, , 550, 713
- Matthee J., et al., 2020, , 498, 3043
- Mayya Y. D., et al., 2020, , 498, 1496
- Meynet G., Maeder A., Schaller G., Schaerer D., Charbonnel C., 1994, , 103, 97
- Meynet G., Ekström S., Georgy C., Chiappini C., Maeder A., 2009, Reviews in Modern Astronomy, 21, 97
- Mingozzi M., et al., 2022, , 939, 110
- Murphy L. J., et al., 2021, , 501, 2745
- Neugent K. F., Levesque E., Massey P., 2021, in American Astronomical Society Meeting Abstracts. p. 119.05D
- Papaderos P., Izotov Y. I., Guseva N. G., Thuan T. X., Fricke K. J., 2006, , 454, 119
- Paxton B., et al., 2013, , 208, 4
- Pettini M., Zych B. J., Steidel C. C., Chaffee F. H., 2008, , 385, 2011
- Pietrinferni A., Cassisi S., Salaris M., Castelli F., 2004, , 612, 168
- Plat A., Charlot S., Bruzual G., Feltre A., Vidal-García A., Morisset C., Chevallard J., Todt H., 2019, , 490, 978
- Reid W. A., Payne J. L., Filipović M. D., Danforth C. W., Jones P. A., White G. L., Staveley-Smith L., 2006, , 367, 1379
- Robertson B. E., Ellis R. S., Dunlop J. S., McLure R. J., Stark D. P., 2010, , 468, 49
- Roman-Duval J., et al., 2020, Research Notes of the American Astronomical Society, 4, 205

- Salpeter E. E., 1955, , 121, 161
- Saxena A., et al., 2020, , 636, A47
- Scalo J. M., 1986, , 11, 1
- Schaerer D., 2003, , 397, 527
- Schaller G., Schaerer D., Meynet G., Maeder A., 1992, , 96, 269
- Schulz J., Fritze-v. Alvensleben U., Möller C. S., Fricke K. J., 2002, , 392, 1
- Senchyna P., Stark D. P., Mirocha J., Reines A. E., Charlot S., Jones T., Mulchaey J. S., 2020, , 494, 941
- Senchyna P., Stark D. P., Charlot S., Chevallard J., Bruzual G., Vidal-García A., 2021, , 503, 6112
- Shapley A. E., Steidel C. C., Pettini M., Adelberger K. L., 2003, , 588, 65
- Sixtos A., Wofford A., Sander A. A. C., Peimbert A., 2023, , 519, 5656
- Smith N., Conti P. S., 2008, , 679, 1467
- Smith L. F., Shara M. M., Moffat A. F. J., 1996, , 281, 163
- Smith L. J., Crowther P. A., Calzetti D., Sidoli F., 2016, , 823, 38
- Sobral D., et al., 2019, , 482, 2422
- Spinrad H., Taylor B. J., 1971, , 22, 445
- Stanway E. R., Chrimes A. A., Eldridge J. J., Stevance H. F., 2020, , 495, 4605
- Szécsi D., Agrawal P., Wünsch R., Langer N., 2022, , 658, A125
- The LIGO Scientific Collaboration et al., 2021, arXiv e-prints, p. arXiv:2111.03606
- Trundle C., Kotak R., Vink J. S., Meikle W. P. S., 2008, , 483, L47
- Valerdi M., Peimbert A., Peimbert M., Sixtos A., 2019, , 876, 98
- Vazdekis A., Sánchez-Blázquez P., Falcón-Barroso J., Cenarro A. J., Beasley M. A., Cardiel N., Gorgas J., Peletier R. F., 2010, , 404, 1639
- Vink J. S., Muijres L. E., Anthonisse B., de Koter A., Gräfener G., Langer N., 2011, , 531, A132
- Völschow M., Banerjee R., Körtgen B., 2017, , 605, A97
- Willson L. A., 2000, , 38, 573
- Wofford A., et al., 2012, arXiv e-prints, p. arXiv:1209.3199
- Wofford A., Leitherer C., Chandar R., Bouret J.-C., 2014, , 781, 122
- Wofford A., Vidal-García A., Feltre A., Chevallard J., Charlot S., Stark D. P., Herenz E. C., Hayes M., 2021, , 500, 2908
- Woosley S. E., Weaver T. A., 1995, , 101, 181
- Yusof N., et al., 2022, , 511, 2814